# ANC of UAS Rotor Noise using Virtual Error Sensing

Melissa A. Polen

Thesis submitted to the Faculty of the
Virginia Polytechnic Institute and State University
in partial fulfillment of the requirements for the degree of

Masters of Science
in
Mechanical Engineering

Christopher R. Fuller, Chair
Steve Southward
Pablo Tarazaga

February 5, 2021
Hampton Roads, Virginia

Keywords: Active Noise Control, Virtual Error Sensors, Unmanned Aerial Systems

# ANC of UAS Rotor Noise using Virtual Error Sensing

Melissa A. Polen

(ABSTRACT)

Traditional active noise control (ANC) systems rely on a physical sensor to measure the error signal at the desired location of attenuation. The error signal is then used to update an adaptive controller, which ultimately attenuates the measured response. However, it is not always practical to use traditional ANC in real-world applications. For example, as small unmanned aerial systems (UAS) become more commonly used, community noise exposure also increases, along with the desire to reduce UAS noise. Traditional ANC systems that rely on physical sensors at observer locations are impractical, since a UAS does not typically have real-time access to the response at an observer's ears, which is realistically in the far-field. Virtual error sensing (VES) can augment an ANC system using near-field measurements to estimate the response at a desired far-field location. In this way, the VES technique effectively shifts the zone of quiet from the location of the physical sensor(s) to a different "virtual" location. This thesis begins by outlining past work that used traditional ANC methods and virtual error sensing techniques. Numerical modeling results showing the predicted spatial change in SPL achieved using a virtual sensor will be presented. Experimental tests used ANC to attenuate the noise from a single UAS rotor at far-field locations using a near-field microphone and the remote microphone technique (RMT) to develop the VES. The results of the VES alone and with an ANC approach at several far-field virtual locations will be presented and discussed.

**Keywords:** active noise control, virtual error sensing, remote microphone technique, unmanned aerial system, feedforward control

# ANC of UAS Rotor Noise using Virtual Error Sensing

Melissa A. Polen

(GENERAL AUDIENCE ABSTRACT)

Small unmanned aerial systems (sUAS) are becoming increasingly common for private, military, and commercial use, and as such, community noise exposure is increasing. Reducing the noise produced by UAS could help improve community acceptance. Active noise control (ANC) might be used to attenuate noise produced by sUAS, however, traditional ANC systems would require a physical sensor in the far-field, which is not feasible. A virtual error sensor (VES) could eliminate the need for a far-field sensor. This thesis describes the proposed VES strategy, and presents numerical simulations and experimental results that highlight both the benefits and limitations of the approach. Results of the VES system with and without an ANC approach are discussed. Experimental testing focused on attenuating the tonal noise produced by one 2-bladed rotor with a tip radius of 4.7 inches. Pressure variations caused by the blade rotation were measured in the near and far-field using electret microphones and externally polarized condenser microphones, respectively. The ANC system used the filtered-x least mean squares algorithm in conjunction with the VES system to estimate the far-field response. A 2-inch diameter speaker served as the secondary source to provide the appropriate control input to the system. Experimental results show reductions between 6-13 dB at varying far-field locations and rotation rates.

**Keywords:** active noise control, virtual error sensing, tonal noise, unmanned aerial system, feedforward control

# Acknowledgments

First and foremost, I would like to thank my advisor, Dr. Fuller, for allowing me the opportunity to work on this study at my own pace and for giving me the freedom and flexibility to explore new ideas on my own. I would also like to thank my mentor at NASA Langley, Dr. Schiller, for his guidance and patience throughout this project.

Thank you to Dr. Cabell and the Structural Acoustics Branch at NASA Langley for their hospitality and willingness to provide any assistance I needed when using the building facilities and available resources. To Dr. Stanley, Dr. Britcher, Rita Aguillard, and Mary-Catherine Bunde at the National Institute of Aerospace, thank you for your helpfulness when I needed assistance registering for classes, for working through any technical difficulties I experienced while participating in my classes remotely, and for allowing me to use NIA's classrooms.

Lastly, I would like to thank my family for their unconditional love and support.

# Contents

# List of Figures

# List of Tables

# Chapter 1

# Introduction

The desire to incorporate unmanned aerial systems (UAS) in commercial, recreational, and military use is becoming increasingly common and as such, noise pollution caused by UAS rotating propellers is more prevalent. This unique and relatively new type of noise pollution can be annoying to members of communities that will be frequently exposed to UAS flights. The Federal Aviation Administration (FAA) studies the effect that aircraft noise has on communites using the concept of noise annoyance, which was developed in the 1960's [1]. In recent years, annoyance due to UAS has been the focus of studies. For example, a study conducted in the Exterior Effects Room at NASA Langley suggests that there is a difference in the annoyance response caused by noise from drones than there is from ground vehicles, indicating that increased use of UAS could face push-back from communities [2]. Attenuating the noise produced by UAS can help achieve community acceptance. Additionally, UAS operating for military use, which fly quietly, have a higher probability of remaining undetected and successfully completing missions. In order to alleviate community annoyance caused by growing UAS use, it could be helpful to identify how they produce noise, and subsequently, how to reduce it.

UAS noise is largely attributed to the propellers. Noise produced by the propeller is typically

dominated by tones, at frequencies that are directly related to both the blade count and the rotation rate. Tonal noise is comprised of thickness and loading noise. Thickness noise is a product of repeated air displacement that is caused by the periodically rotating propeller blades and is dominant in the plane of the rotor. Loading noise is caused by lift and drag forces that affect the pressure distribution on the blades. Researchers [3, 4, 5] have studied UAS vehicles, their subsystems, and their components, and found that rotor noise is well defined at the rotor blade passage frequency (BPF) and its harmonics. Stephenson, Weitsman, and Zawodny [6] demonstrated that in a closed chamber, a rotating system experiences recirculation effects once fluid that has been displaced by the propeller blades is ingested back into the propeller. This unsteady loading force can amplify the rotor harmonics as much as 15 dB. In practical applications, these recirculation effects might not be seen, but they could be relevant during testing. Propeller blade noise has been the focus of many studies which aim to reduce blade noise using either passive or active methods of noise control.

Noise control attenuates a disturbance noise through methods that are described as passive or active. Passive noise control uses absorptive or reflective materials to redirect sound from some desired location and does not require external energy. Examples of passive techniques include mufflers and sound barriers on highways. Passive techniques are easily implemented and effective for noises with frequencies higher than 1 kHz. At low frequencies, however, passive techniques are not as effective [7]. As frequency decreases, the associated wavelength increases, and the required thickness of absorptive material increases as well. Peak absorption occurs when the material thickness is at least one-quarter of the acoustic wavelength; for example, the required material thickness of a rotor operating with a BPF of 200 Hz would be almost one-half meter, leading to a design that cannot practically be applied. Design constraints often limit the size of absorptive material that may be used to attenuate sound. Although size and weight are limiting constraints in attenuating noise produced by UAS propeller blades, the use of passive noise control has been explored. Dot-

terel Technologies [8] developed a duct made from lightweight acoustic materials that shrouds the propellers of a UAV and is meant to redirect the noise upwards away from potential observers, though measured performance is not readily available.

Although passive noise control can be easy to implement, it is not always practical when aiming to attenuate low frequencies since the required thickness typically increases as frequency decreases. UAS do not have the space for these materials and can be limited by weight requirements. Additionally, rotor tones are typically dominant at frequencies lower than 1 kHz [6, 9]. It may be possible to attenuate noise produced by UAS by implementing active noise control (ANC), as considered for example by Schiller and Zawodny [10]. Active noise control (ANC) can be a cost effective way to attenuate noise produced by frequencies ranging between 50 and 1 kHz, frequencies that are difficult to control using passive techniques. In traditional ANC applications, a primary source radiates a disturbance sound to some location and an error sensor, usually a microphone, is placed at the desired location of attenuation. A secondary source, typically a loudspeaker, produces acoustic sound waves of the same amplitude as the disturbance noise that are 180 degrees out of phase; the sound produced by the secondary source destructively interferes with the disturbance sound. The degree of destructive interference is dependent on the pressure field information that is provided by the error microphone [11].

## 1.1 Background

### 1.1.1 Active Noise Control

Lueg [12] suggested ANC in a one-dimensional duct, in which an upstream sensor measured a disturbance noise that was provided to controller. The duct limited the sound to propogate in one direction and kept the noise from spreading to three-dimensions. A control signal was then created

and passed through a loudspeaker that was located in the duct, downstream of the reference sensor. The primary disturbance signal and the control signal canceled each other, effectively reducing the noise at the desired location. This active noise control structure is called feedforward, because the disturbance noise is measured and used to update the controller before it affects the system. Figure 1.1 illustrates feedforward ANC in a one dimensional duct similar to Lueg's patent.

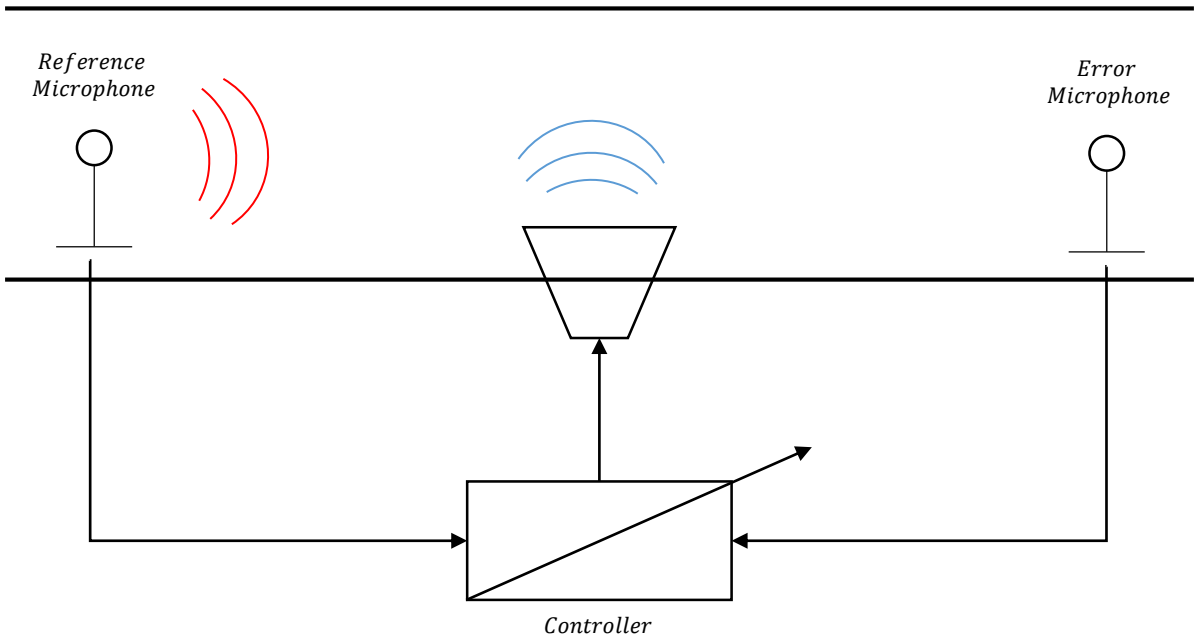


Figure 1.1: Feedforward ANC in a one dimensional duct.

Lueg's feedforward design achieved global attenuation at the locations located downstream from the loudspeaker. Where Lueg's patent described a 1-dimensional sound field, others explored more complex sound fields. For example, Elliott, Bullmore, and Curtis examined global ANC in a modally dense 3-dimensional enclosed sound field in a series of studies [13, 14, 15]. The studies focused on reducing the sound produced by propeller blades in aircraft cabins in order to achieve acceptable levels for passengers. The feasability in achieving global attenuation in a modally 3D sound field was investigated throughout the studies. It was found that secondary sources should be placed less than one-half wavelength of the frequency of interest from the primary noise source

in order to achieve significant reduction. Elliott et. al. [16] also studied the consequences that ANC in a pure tone diffuse sound field has on the surrounding sound field and confirmed that the zone of quiet surrounding the cancellation point had a diameter of one-tenth of the wavelength of the excitation frequency. Further studies [17] expanded on previous work and studied the near-field cancellation in a pure tone diffracted diffuse sound field. It was demonstrated that reflecting surfaces that are close to the cancellation point can broaden the zone of quiet.

The idea of applying ANC to reduce turbofan noise has been the subject of many studies. ANC systems have been applied to fan applications to study their effectiveness in reducing the radiated sound. Thomas et. al. [18] conduced experimental testing on a JT15D turbofan engine using a reference sensor located at the fan stage in the outer casing wall and provided a reference signal to the control system by measuring blade pulses. An error sensor, located in the far-field and on the centerline of the turbofan engine inlet, provided the error signal to the control system, which used filtered-x least mean square (FxLMS) algorithm to develop the control signal which was passed through control actuators that were located on the fan inlet. Results showed SPL reduction at the BPF within the zone of reduction, which ranged from 10°to -20°from the centerline, with maximum SPL reduction of 19.2 dB achieved at the error sensor. Additionally, results showed that spillover effects increased the SPL outside of the zone of reduction.

Work conducted by Thomas et. al. [19] studied the feasability in applying ANC from sound radiated from a turbofan engine using control actuators and reference sensors that were placed on the turbofan inlet to pass the fundamental frequency and harmonics through the control system. The FxLMS algorithm was used in a feedforward ANC system to reduce the tonal noise radiated from the turbofan at far-field locations. Error microphones that were placed in the far-field measured up to 16 dB SPL reduction at the fundamental frequency. In related work, Smith and Burdisso [20] aimed to reduce the sound radiated from a JT15D turbofan engine using 12 control actuators located on the circumference of the engine. A hybrid passive-active control technique was found to

effectively reduce the radiation in particular far-field directions. Smith, Burdisso, and Fuller [21] also aimed to reduce the tonal inlet noise from a turbofan engine using control actuators that were placed at various axial locations on the engine. The engine generated four radial modes and the control arrays controlled the radial duct modes. This test demonstrated that a single optimized control array achieved better results than using multiple arrays. Additionally, this test demonstrated that controlling only a portion of the sound field takes less effort than trying to achieve global attenuation. The patent filed by Fuller and Burdisso [22] proposed using a compact sound source to actively control the fan noise from a turbofan engine. The control source consisted of thin panels that were flush mounted on the inlet duct and were driven by a piezoelectric force transducer. This system was designed to operate over the frequency range 2000-4000 Hz.

Studies conducted at NASA Glenn Research Center [23] focused on reducing fan noise with well-defined modal qualities due to the complex noise field inside a fan duct. Several noise control techniques were considered, including various outlet vane guide configurations, which reduced the tonal level at the BPF between 5 and 10 dB. Additionally, the feasibility of applying active noise control to fan noise was also studied, each consisting of an error sensor, a controller, and a control actuator array. The control arrays were located in either the inlet duct or the exhaust duct, depending on the desired location of attenuation. In one case, an average of 18 dB in tonal reduction was achieved over a range of fan speeds. It was concluded that it is feasible to use a variety of ANC techniques to achieve tonal reductions from fan noise. Additionally, the feasibility of using wall mounted secondary sources within the duct of turbofan engines to apply ANC and reduce fan noise was validated by General Electric in the active noise control fan facility at NASA Lewis (now Glenn) Research Center [24]. The test aimed to achieve global ANC of a turbofan while it was operating and a known acoustic mode propagated through the duct. The far-field SPL was reduced by 15 dB global attenuation was achieved at the target frequency. The study also noted that control spillover did adversely affect the reduction. The test concluded that using an

array of secondary sources and a modal controller could eliminate a known propagating fan mode, demonstrating that ANC was a feasible method of reducing fan noise.

ANC has also been studied in CPU fan applications. Gee and Sommerfeldt [25, 26] studied a method of ANC which allowed for error sensors to be placed in the near-field of primary and secondary sources. The primary and secondary sources were modeled as ideal monopoles and the secondary sources were modeled to radiate minimum power. The error sensors were placed in locations that achieved greatest levels of reduction in SPL. This placement strategy achieved greater far-field SPL attenuation than when the error sensors were placed in arbitrary locations. Gee and Sommerfeldt [27] extended previous work and experimentally investigated the effect that the placement that error sensors have on the system. Taking into consideration that far-field reductions can also lead to increased noise in the near-field [7], Gee and Sommerfeldt studied the concept of a near-field ANC system based on the practicality of a compact system in CPU cooling fan applications. Experimental testing demonstrated that identifying and placing error sensors in ideal locations created acoustic coupling of the control loudspeakers, ultimately leading to greater sound power reduction. However, it should be noted that error sensors that were placed in nonideal locations still achieved sound power level reductions, although they were less than that achieved using error sensors placed in ideal locations. Fuller [28] also studied the effect of a hybrid active-passive noise control system on ducted computer fans. This configuration achieved a total sound power level reduction of 7.5 dBA over the frequency range 124 Hz to 10 kHz for both tonal and broadband noise.

### 1.1.2 Virtual Error Sensing

Although traditional methods of ANC have proven to be effective means of quieting a variety of applications including CPU fan noise, engine noise, and duct noise, it is not practical to use them to

attenuate the noise from an in-flight UAS at ground locations. Traditional ANC relies on a physical sensor that is located at the desired location of attenuation to provide the control system with an error input. Virtual error sensing is a technique that can be applied to ANC and eliminates the requirement of having a physical error microphone placed at the desired location of attenuation. During virtual error sensing, an error estimate is created using prior knowledge of the sound field. This error estimate is then passed through the controller, which generates the appropriate control signal to attenuate the SPL at the desired location, effectively removing the physical error sensor constraint in traditional ANC systems [29]. The flexibility afforded by virtual error sensing is appealing for applications like UAS noise, where it is not possible to use a physical error sensor in the control system. This section discusses the background of virtual error sensing and details previous applications of virtual error sensing in ANC systems.

The effectiveness of virtual error sensing has been demonstrated in duct arrangements that are similar to Lueg's in many studies. For example, Peterson et. al. [30] considered applying ANC using virtual error sensing on a duct arrangement. The Kalman filtering theory and physical sensors in the near-field were used to develop a virtual sensing algorithm which estimates the error signals at remote, or virtual, locations. Results showed that using virtual error sensors in the control system reduced the SPL in the duct by 19 dB. Munn, Cazzolato, Kestell, and Hansen [31] also demonstrated active noise control at low frequencies using virtual error sensors. Tonal noise was played throughout a narrow duct. The virtual sensors were established through a fitted curve. The curve was estimated using multiple transducers throughout the duct; then, the virtual error sensors were passed through the ANC system where a control signal was established. The SPL attenuation at different separation distances between the transducer and the observer location were compared. The results showed that the greatest SPL attenuation was achieved when the virtual sensors were located closest to the observer location.

ANC using virtual error sensing has been applied in environments that are more complex than

one-dimensional ducts, as well. Virtual error sensing is commonly applied to active headrests. In practice, it is not practical to position error sensors directly at the listener's ears, where they would impede the observer's movements. Active headrest configurations typically use speakers that are located behind the headrest and act as secondary sources to the system. Sensors located near the listener's head but not at the virtual location are used to measure the primary disturbance and shift the zone of quiet to the virtual location. For example, the virtual microphone arrangement has been used to estimate the response at the virtual location, and subsequently apply ANC in an active headrest configuration in a diffuse sound field [32]. Bean et. al. [33, 34] designed a hybrid control active headrest that used virtual error sensors to shift the zone of attenuation to the listener's ears. Feedforward, feedback, and hybrid control structures were compared using the remote microphone technique [35] to estimate the pressure at the listener's ears. This study found that the SPLs at the listener's ears were reducd by 15-20 dB over broadband disturbances with a hybrid controller. The SPLs were reduced 10-15 dB when the remote microphone technique was used in conjunction with the hybrid controller to estimate the pressure at the listener's ears.

Fuller, Papenfuss, and Saux [36] applied passive noise control in conjunction with ANC using virtual error sensors to reduce the radiated noise from a portable generator in a field. Passive treatment was applied to a generator and effectively attenuated the SPL in the bandwidth above 500 Hz, but was ineffective at reducing frequencies below 500 Hz. As it is not practical to implement ANC on a portable generator using a physical sensor at fixed far-field locations, the performance of an ANC system using virtual error sensors was examined. Through simultaneously using passive treatment and ANC through virtual sensors, the SPL at the desired location was between 10.5 to 13 dBA.

Moreau et. al. [37] studied the effectiveness of using virtual error sensors with a local ANC system in a pure tone diffuse sound field. This study extended previous work that studied the feasability of using traditional ANC methods in a pure tone diffuse sound field [13, 16]. Nine

virtual error sensing strategies were used to apply local ANC to a pure tone diffuse sound field. Numerical models showed that virtual error sensing strategies achieved higher SPL reduction than traditional control methods. Experimental results confirmed that it is possible to use virtual error sensing with an ANC system to achieve noise reduction at virtual locations. In ANC systems, it is common to use a secondary source to minimize the squared pressure at a microphone location. However, establishing virtual sensors using energy density, which is more spatially uniform than squared pressure, has been investigated as well. Kestell, Cazzolato, and Hansen [38] established virtual energy density sensors in a free-field environment with a single primary source. A model predicted that virtual energy density sensors were capable of establishing a zone of local ANC around a virtual observer location, although experimental testing showed that the virtual sensors were sensitive to the primary and secondary sources spatial variations at shorter wavelengths.

## 1.2 Objectives

This thesis proposes, develops, and analyzes a feedforward virtual sensor which will be used in conjunction with an ANC system to reduce the noise produced by a UAS propeller in an anechoic chamber at a far-field observer location. The sound in the far-field is attenuated through estimating and subsequently minimizing the pressure in the far-field. The remote microphone technique [35] was the chosen virtual sensing strategy that estimated the far-field pressure using the transfer functions and an observation filter and near-field pressure measurements. The remote microphone technique extends the virtual microphone arrangement [39] and estimates the primary disturbance at the virtual location. It has been demonstrated that the remote microphone technique can estimate the response at the virtual location if the primary disturbance is deterministic [29]. As rotor noise is usually dominated by tonal noise, this suggests that the remote microphone technique might be a practical solution to in-flight UAS noise.

### 1.2.1 Organization

Chapter 2 provides a review of active noise control. Feedforward and feedback control are introduced. Digital filters that were used to apply ANC in this study are discussed. Chapter 3 outlines virtual error sensing approaches. Studies that use virtual error sensing techniques are discussed. Chapter 4 describes the numerical model that was used to evaluate the feasibility of applying ANC using virtual error sensors. The numerical model also aided in understanding how surrounding locations responded during ANC. Chapter 5 discusses the experimental testing setup and describe the control system that was used to apply ANC at several rotor rotation rates. The virtual error sensor results are presented and discussed in Chapter 6. ANC system results are presented in Chapter 7; the SPL reduction at an observer location through ANC using a physical error sensor was compared to that achieved using a virtual error sensor to apply ANC. Concluding remarks and future work recommendations are stated and offered in Chapter 8.

# Chapter 2

# Active Noise Control

This chapter further discusses ANC theory as it applies to this work. ANC architectures are described and an overview of digital filters is included in this chapter. Additionally, digital filters that were used in this work are detailed.

In traditional ANC applications, a primary source radiates a disturbance sound to some location and an error sensor, usually a microphone, is physically located at the desired location of attenuation [11]. Figure 2.1 illustrates a generic ANC system which relies on an error microphone to measure the disturbance input. A secondary source, typically a loudspeaker, produces acoustic sound waves of the same amplitude as the disturbance noise that are 180 degrees out of phase, producing a signal that destructively interferes with the primary disturbance noise. The amplitude and phase of this control signal is dependent on the pressure field information that is provided by the error microphone. ANC is typically most effective at low frequencies. At higher frequencies, the sound field can become increasingly complex, leading to less efficient attenuation and making ANC a less desirable solution [7].

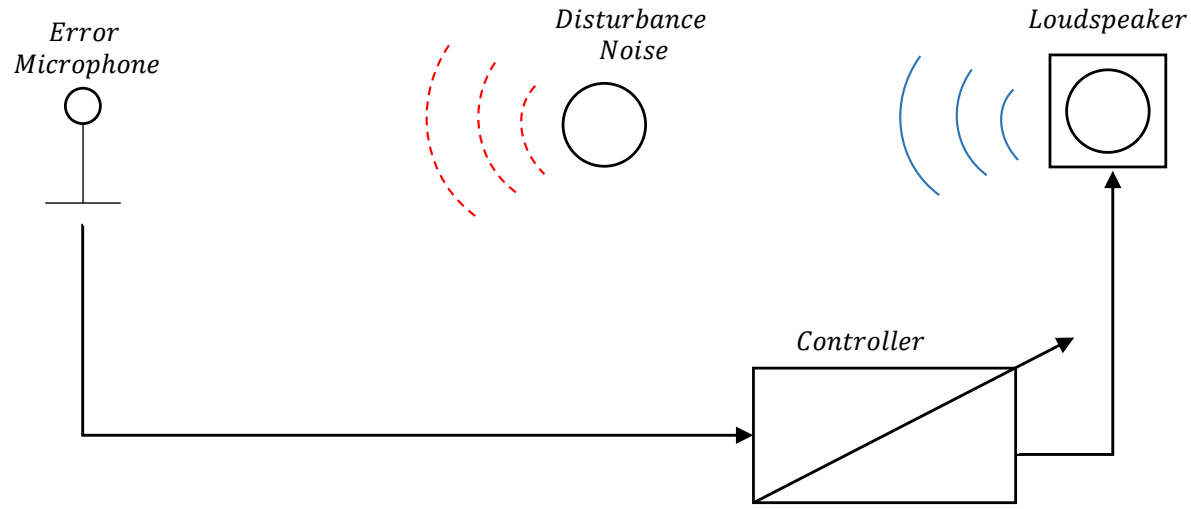


Figure 2.1: Traditional ANC system using an error sensor to measure the disturbance signal and estimate a control input.

ANC can attenuate noise either locally or globally. Global ANC achieves noise control throughout an acoustic space by minimizing the total energy in a system. Elliott et. al. [13, 14, 15] studied the feasibility of employing global ANC in a modally dense three-dimensional sound field. The studies found that global reduction was achieved using secondary sources that were placed less than one-half of the acoustic wavelength, $\lambda$, from the primary noise source. While global ANC aims to minimize the energy in a sound field, local ANC attempts to minimize the local sound pressure, which might require less effort than global ANC. For this reason, local ANC is commonly applied. These studies also examined the size of the zone of quiet in a diffuse sound field using acoustic monopoles as both the primary and secondary sources. They demonstrated that when the distance between the secondary source and the cancellation point was greater than the wavelength, the zone of quiet was spherical at the cancellation point. In this application, the zone of quiet extended $\lambda/10$ in diameter and reduced the SPL inside the sphere by 10 dB. The zone of quiet limits the attenuation to the location of the error microphone and requires observers to be close to the microphone in order to perceive noise reduction, which is often impractical. Additionally, the pressure field surrounding the error sensor can become amplified when control is applied, further

restricting the effectiveness of ANC. Control systems can have either feedback or feedforward architectures. The architecture is usually contingent on whether or not a reference signal is available to the system. For example, feedforward arrangements are applied if a reference signal is available and coherent with the disturbance noise [40].

## 2.1 Feedback ANC

ANC systems are categorized in two architectures: feedback and feedforward. This section will discuss feedback control; feedforward ANC will be discussed in the next section. Feedback ANC can be used when a reference signal is not available to provide time-advanced information to the controller. Rather, a disturbance signal is measured by an error sensor that is located near the desired location of attenuation. The measured error response is then fed back through the fixed or adaptive controller which establishes the control input that rejects the disturbance noise [41]. Figure 2.2 shows a block diagram of a feedback control system similar to the one discussed in [41]. The error signal, $e(n)$, is passed through the controller, $-H(z)$, to generate a control signal. The plant, $G(z)$, estimates the path from the control output to the disturbance noise, $d(n)$, and generates a noise canceling signal.

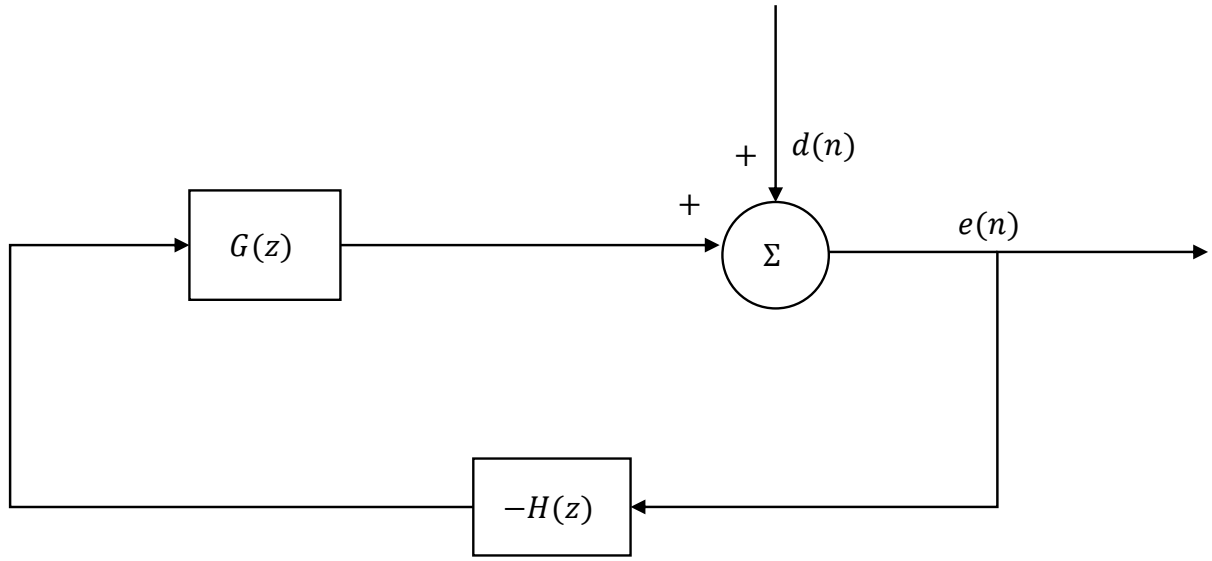


Figure 2.2: Feedback block diagram.

Feedback control is advantageous because it does not require a coherent reference signal. For example, cabin noise in aircrafts or automobiles can be produced by a variety of sources. In these applications, a coherent reference signal is not available, and feedback control may be applied. Olson and May designed an active headrest for cabin noise using feedback ANC [42]. This design used an error microphone to detect the noise in the system, which was then passed through a signal conditioner and a canceling loudspeaker that was located close to the error microphone. This configuration achieved 25 dB attenuation in the cabin. Although feedback ANC is convenient to apply when a coherent reference signal is not available to the system, feedback controllers are only updated after a disturbance noise affects the system. This limitation usually leads to some time delay associated with feedback controllers. Additionally, although feedback controllers are stable over a specific bandwidth, feedback control systems used in [42] risk instability due to feedback at high frequencies where the phase is not easily controlled.

## 2.2 Feedforward ANC

In contrast to feedback control, feedforward ANC can be applied when a reference signal is available to monitor the disturbance noise. Reference signals are derived from the primary disturbance (i.e. a tachometer provides relevant information of a rotating shaft) [43]. The reference signal can be captured using either acoustic or nonacoustic sensors, and is chosen considering the spectral content of the disturbance noise as long as it is highly correlated with the error sensor. For example, ANC applications aiming to reduce broadband noise cannot use a nonacoustic reference sensor which relies on periodicity, like a tachometer, to appropriately monitor the primary disturbance. A tachometer is only capable of measuring the deterministic content of the disturbance noise, and the random content would remain undetected. In order to measure broadband noise, a sensor that can monitor the entire disturbance must be used, like a microphone or an accelerometer. For example, Cheer [44] demonstrated that the noise radiating from a plate can be reduced using a feedforward arrangement, where an accelerometer monitored the plate vibration. Feedforward control is advantageous because the reference sensor allows the disturbance noise to be measured and used to update the controller before it affects the desired location of attenuation, whereas a feedback controller is only updated after the disturbance signal affects the location of attenuation.

Figure 2.3 shows a diagram of a standard feedforward block diagram where a reference signal, $x(n)$, and controller, $W(z)$, estimate a control signal $u(n)$. Once the control input is passed through the plant $G(z)$, the noise canceling output signal, $y(n)$ is estimated. The error signal $e(n)$ can be calculated by taking the sum of the disturbance signal, $d(n)$, and the output signal, $y(n)$, which has opposite phase of $d(n)$.

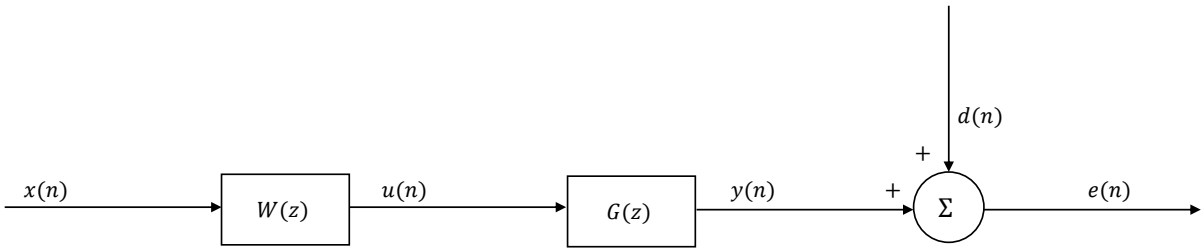


Figure 2.3: Feedforward block diagram.

Although broadband feedforward ANC is limited by causality, which relies on past and current input values, narrowband disturbances are not and can use nonacoustic sensors like a laser tachometer or an optical sensor to provide the reference signal. Additionally, nonacoustic reference sensors afford more flexibility in the placement of the secondary source. Nonacoustic reference sensors are advantageous because they eliminate acoustic feedback from the secondary speaker to the reference microphone [40]. Without feedback from the speaker to the reference sensor, the controller is able to operate using an FIR filter, thereby guaranteeing that the system remains stable. The inherent stability provided by feedfoward controllers makes them advantageous over feedback controller; if a coherent reference signal is available, it is common to opt to use feedforward controllers over a feedback structure.

As previously mentioned, Lueg [12] first suggested the concept of feedforward ANC in a simple one-dimensional duct, in which an upstream microphone measured a disturbance noise, which provided the controller input. A control signal was created and passed to a loudspeaker at the end of the duct. This setup has since successfully demonstrated global attenuation throughout the duct. Feedforward ANC has also been demonstrated in a more complex sound field [18, 19, 20]. Due to their similarity to electrical noise cancellation systems, feedforward ANC systems are often based on adaptive filtering techniques.

## 2.3 Digital Filters

Filtering is the method of altering the characteristics of an input signal to appropriately estimate an output signal. Time invariant filters are linear and perform a constant set of operations on the input signal. Adaptive filters are continuously updated, so the filter parameters are changed with time. The filter coefficients are continuously adapted using an adaptive algorithm. Adaptive digital filters therefore consist of the filter and the adaptive algorithm. Digital filters estimate a discrete time-sampled output response using a discrete time-sampled input sequence. Digital filters are commonly used for their adaptability, accuracy, and cost effectiveness and are classified as finite impulse response (FIR) or infinite impulse response (IIR) filters. Although IIR filters are low order and have a fast computational speed, they use feedback of the filter output as the input and as a result, are not always stable [40]. This section will focus on FIR filters, as they are used during experimental testing.

An FIR filter is implemented in practice by setting a finite length for the filter to operate on the input signal, which can be seen in Figure 2.4. FIR filters are causal and therefore use past and current inputs to determine a system output. Systems that operate in real-time must be causal in order to be realizable, because it is impossible for them to act on future input. Causality refers to the cause and effect relationship that physical control systems share while operating in the real world. FIR filters are attractive because they are always stable, are robust in that small changes to the disturbance input result in small changes in the output estimate, and can easily be designed to provide a linear phase response. The estimated FIR filter response signal, $y(n)$, is given,

$$y(n) = \sum_{i=0}^{I-1} w_i x(n-i) \tag{2.1}$$

through the summation of the digital filter coefficients, $w_i$, and the past and present input

signals, $x(n)$. The filter length, $I$, dictates the number of filter coefficients. It should be noted that Equation 2.2 shows that the current output only depends on the current input, and assumes that the filter can calculate the output instantaneously. However, this assumption is unrealistic, so a one sample delay is assumed in practical applications. This sample delay allows for computation time. The estimated, delayed filter output is expressed by rewriting the Equation 2.2 as,

$$y(n) = \sum_{i=1}^{I} w_i x(n-i) \tag{2.2}$$

where the delay is included. Figure 2.4 shows a block diagram of an FIR representation with unit delay operator $z^{-1}$. The past and present input signal values are convolved with the filter coefficients, which are added together to estimate the output $y$ at the discrete sample $n$.

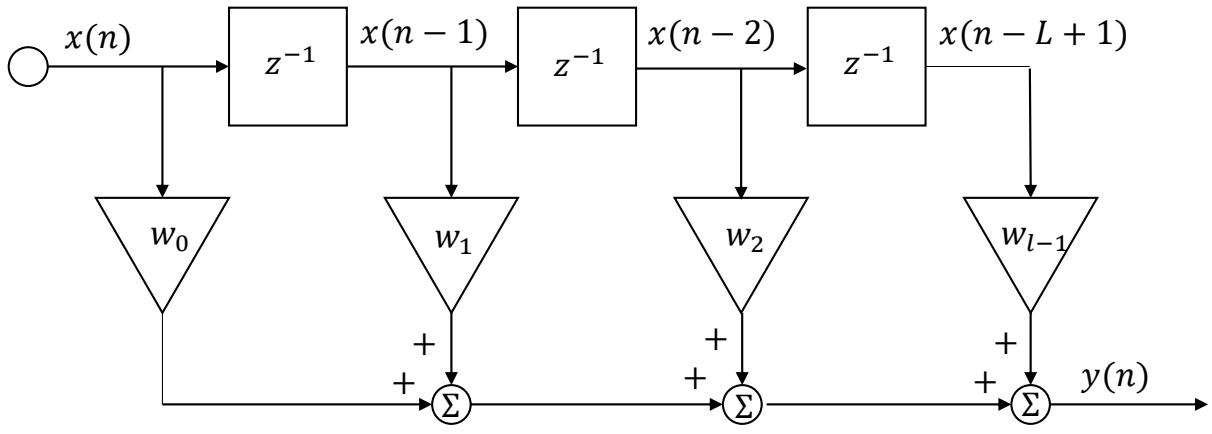


Figure 2.4: Block diagram of an FIR filter

For simplification, a vector of filter coefficients, **w**, and a reference vector of input signals, $\mathbf{x}(n)$, are defined

$$\mathbf{w} = \begin{bmatrix} w_0 & w_1 & w_2 & \dots & w_{I-1} \end{bmatrix}$$

$$\mathbf{x}(n) = \begin{bmatrix} x(n) & x(n-1) & x(n-2) & \dots & x(n-I-1) \end{bmatrix}$$

Therefore, the output response, $y(n)$, is equal to

$$y(n) = \mathbf{w}^T(n)\mathbf{x}(n) \tag{2.3}$$

as shown in Figure 2.3. Additionally, the output response can be compared with the disturbance signal,

$$e(n) = d(n) - y(n) \tag{2.4}$$

where $e(n)$ is the error between the disturbance signal, $d(n)$, and the output response, $y(n)$.

## 2.4 Wiener Filter

This discussion closely follows the one provided in Elliott [41]. The Wiener filter is an optimal FIR filter that uses coefficients to estimate the output signal using an input signal through minimizing the mean square error (MSE). The Wiener filter is helpful in identifying the model that best estimates the path between the reference sensors and error sensors at desired locations. The

optimal FIR coefficients can be calculated using the equation

$$\mathbf{w}_{opt} = \mathbf{A}^{-1}\mathbf{b}. \tag{2.5}$$

where **A** is the autocorrelation matrix of the input, which is the speaker input in this application, and **b** is the cross-correlation vector between the speaker and the far-field microphone. The frequency response was estimated using the optimal filter coefficients and the far-field microphone data. The measured transfer function was estimated using the validation data set and the H1 estimator, which yields the transfer function from the ratio of cross-spectral density to auto-spectral density.

## 2.5 LMS Algorithm

The least mean square (LMS) algorithm adaptively determines the optimal coefficients of an FIR filter and subsequently minimizes the mean-square error (MSE) between the desired and estimated response signals. The LMS algorithm is often used because it is easy to implement and has adaptive qualities. Data is sequentially passed through the LMS algorithm to continuously adjust the filter coefficients, allowing the algorithm to accurately adapt to unpredicted changes in the input signal [40]. Figure 2.5 illustrates how the LMS algorithm is used in calculating an estimated response signal.

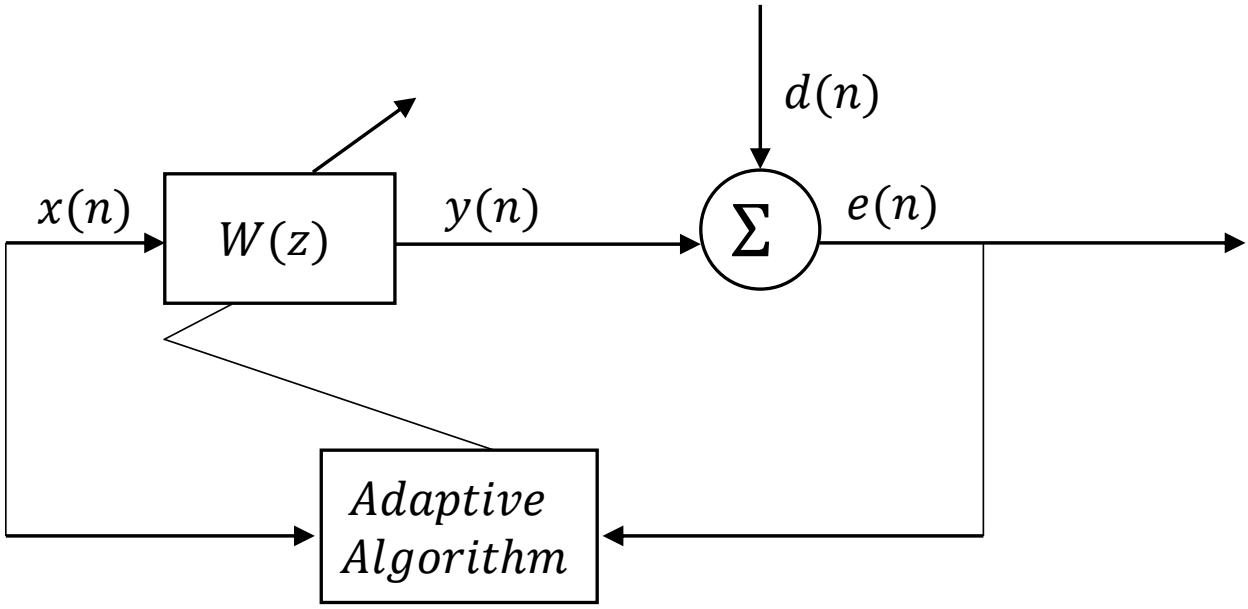


Figure 2.5: Simplified block diagram of the LMS algorithm using an adaptive FIR filter.

First, the parameters $L$, $\mu$, and $\mathbf{w}(0)$ are chosen; these parameters are the filter length, the convergence factor, and the initial weight vector at $n$ = 0, respectively. The error between the measured response and the estimated response is calculated

$$e(n) = d(n) - \mathbf{x}^T(n)\mathbf{w}(n) \tag{2.6}$$

This calculated error is applied to the LMS algorithm, defined by Elliott [11] as,

$$\mathbf{w}(n+1) = \mathbf{w}(n) - \mu e(n)\mathbf{x}(n) \tag{2.7}$$

where $\mathbf{w}(n+1)$ is the filter coefficient at the next time step in the vector $\mathbf{w}$ and $\mu$ is the step size that is either increased or decreased to increase the speed of convergence in the algorithm.

Convergence can be determined by examining the MSE of the LMS algorithm. The MSE is the expected value of the squared error response.

## 2.6 FxLMS Algorithm

The filtered-x LMS (FxLMS), also known as the filtered reference LMS algorithm, is a modification of the LMS algorithm that uses an estimate of the system's secondary path, $\hat{G}(z)$, to filter the reference signal, $x(n)$, in order to provide a time-aligned signal to the LMS update equation [40]. The secondary path models the controller output to the error microphone, which consists of the physical components of the control system, including the A/D and D/A converters, the reconstruction and anti-aliasing filters, amplifiers, loudspeakers, and the acoustic path from the loudspeaker to the error microphone. The LMS algorithm determines the optimal filter coefficients to compensate for the time delay that is created by the physical distance between the reference microphone and the control speaker. The filtered-x LMS algorithm was developed to compensate for the time delay that is prevalent in feedforward systems due to the physical distance that separates the control speaker and the error microphone. In the LMS algorithm, the error is directly multiplied to the reference signal to produce a cross-correlation estimate that is used to update the filter. However, in the feedforward ANC approach, the error is first filtered by the secondary path and the cross-correlation is subsequently distorted [41]. The inherent time delay that is created by the physical distance between the actuator and the error sensor and the time delay caused by the components of the control system that are used in practice should be accounted for. The FxLMS algorithm pre-filters the reference input signal using an estimate of the secondary path so that the measured error signal will be time-aligned with the filtered reference signal to produce an accurate cross-correlation estimate. The FxLMS algorithm has been widely used in active noise control applications due to its simplicity and adaptability. Studies aiming to reduce duct noise, turbofan engine

noise, generator noise, have all used the FxLMS algorithm to update the adaptive controllers in their ANC systems. A block diagram of the FxLMS algorithm is shown in Figure 2.6.

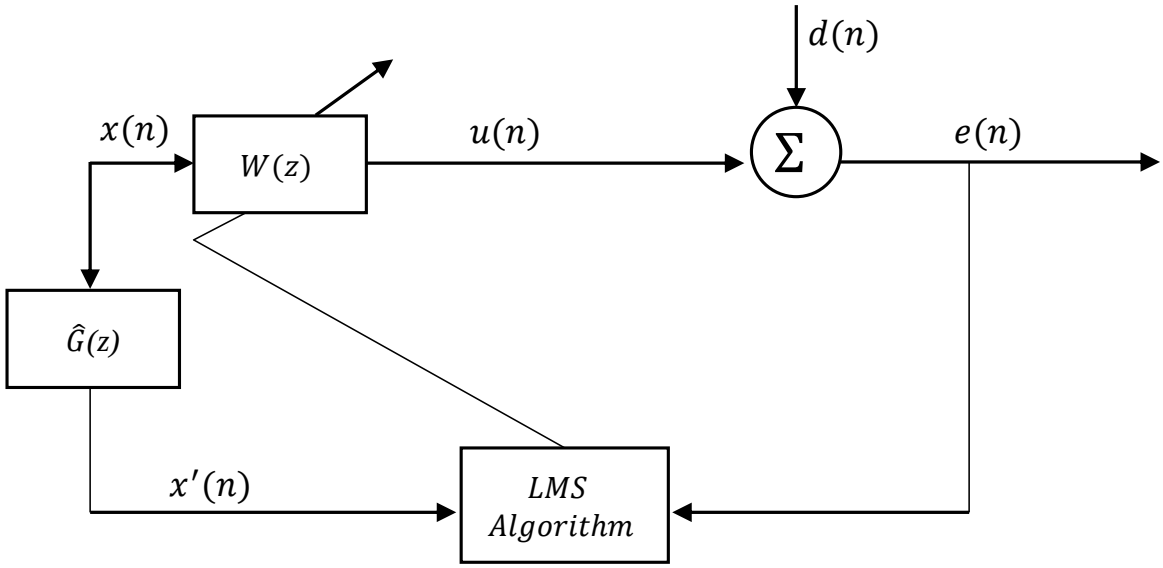


Figure 2.6: Block diagram of the FxLMS algorithm.

This derivation closely follows the one described by Elliott [41]. As shown in Figure 2.6, $x(n)$ is the reference signal. The control filter, $W(z)$, and the secondary path, $S(z)$, are both modelled as FIR filters. The error signal is subsequently calculated using the equation

$$e(n) = d(n) + \sum_{j=0}^{J-1} \sum_{i=0}^{I-1} \mathbf{w}_i(n-j) s_j x(n-i-j) \tag{2.8}$$

where $i$ is the length of the controller, $W(z)$, and $j$ is the length of the secondary path, $\hat{G}(z)$. The FxLMS algorithm accounts for the time delay introduced by the secondary path $\hat{G}(z)$ by creating a secondary path model $\hat{G}(z)$ and pre-filtering the reference signal $x(n)$. The filtered reference signal $x'(n)$ is calculated through

$$x'(n) = \sum_{j=0}^{J-1} \hat{g}_j x(n-j) \tag{2.9}$$

with $\hat{g}_j$ being the secondary path model. Equation 2.10,

$$e(n) = d(n) + \sum_{i=0}^{I-1} w_i x'(n-j) \tag{2.10}$$

calculates the error signal using the disturbance signal, $d(n)$, and the estimated response signal. The filter update equation for the FxLMS algorithm is

$$\mathbf{w}(n+1) = \mathbf{w}(n) + \mu \mathbf{x}'(n) e(n) \tag{2.11}$$

where $\mathbf{w}(n)$ is the filter coefficient at the current sample, $n$, and $\mathbf{w}(n+1)$ is the filter coefficient at the next sample. Additionally, similar to the filter update equation used in the LMS algorithm, $\mu$ is the convergence factor.

# Chapter 3

# Virtual Error Sensing

This chapter discusses the concept of virtual error sensing and the motivation behind employing virtual sensors in ANC systems. The virtual error sensing strategy that was used in this study is also outlined and past work that has applied ANC using this strategy is discussed. Although a number of virtual error sensing algorithms have been developed, this chapter will focus on the virtual microphone arrangement and the remote microphone technique, as they are relevant to the progression of this work. Virtual error sensing is examined due to the impracticality of using a physical sensor at a far-field observer location to provide an error sensor to the control system to attenuate the noise produced by an in-flight UAS , like in traditional ANC practices. Virtual error sensing estimates the response at the far-field observer location, removing the constraint of using a physical sensor and was identified as a possible solution to attenuate the far-field SPL from a small UAS.

While traditional ANC minimizes pressure in the far-field using a physical microphone located at the desired location of attenuation to provide an error signal to the system, ANC through virtual error sensing is a technique that attenuates sound at a desired location by minimizing the filtered error at a physical sensor. Virtual sensing uses prior knowledge of the system, a controller, and a

microphone in close proximity to the noise source to estimate the error at some desired observer location. This microphone in close proximity provides the error measurement for the system and is also referred to as the error sensor. Signal data acquired using an observer microphone is first passed through a virtual sensing algorithm to create an estimate of the pressure response at a remote "virtual," desired location. Similar to traditional ANC, a canceling loudspeaker in placed in close proximity to the disturbance noise produces a noise canceling signal. Rather than providing the controller with a measured error signal using a physical microphone, the control input is determined based on the estimated pressure at the virtual location. Virtual error sensors are able to shift the zone of attenuation from the error sensor to a desired virtual location, which subsequently eliminates the requirement of physical microphones at the locations of attenuation [29].

## 3.1 Virtual Microphone Arrangement

The virtual microphone arrangement (VMA), proposed by Elliott and David [39], was the first virtual sensing algorithm that was developed for ANC. The VMA assumes that the pressure at the physical sensor location caused by the primary disturbance is equal to the pressure at virtual microphone locations such that $\mathbf{d}_v = \mathbf{d}_p$. This assumption holds if the primary sound field does not significantly change between the physical and virtual microphones, which can be true when the separation distance between the physical sensor and the virtual location is small compared to the wavelength of the primary disturbance. The virtual microphone arrangement is most easily implemented using the same number of virtual and physical microphones, however, it is possible to use an unequal number of physical and virtual sensors. Similar to the notation used in [29], the physical microphones in a system that uses $M$ microphones can be described,

$$\mathbf{e}(n) = \begin{bmatrix} e_1(n) & e_2(n) & \dots & e_M(n) \end{bmatrix}$$

which provide the error signals to the control system. A system with $S$ secondary sources requires a primary path, $\mathbf{G}_{vu}$ with the dimensions $M$ x $S$. A block diagram of the VMA is shown in Figure 3.1. A preliminary identification stage is required to identify the paths between the control signal and the physical microphone $\mathbf{G}_{pu}$ and the control signal and the virtual microphone $\mathbf{G}_{vu}$. The path $\mathbf{G}_{vu}$ is identified using temporarily placed microphones at the virtual locations; once $\mathbf{G}_{vu}$ is created, the temporary microphones are removed.

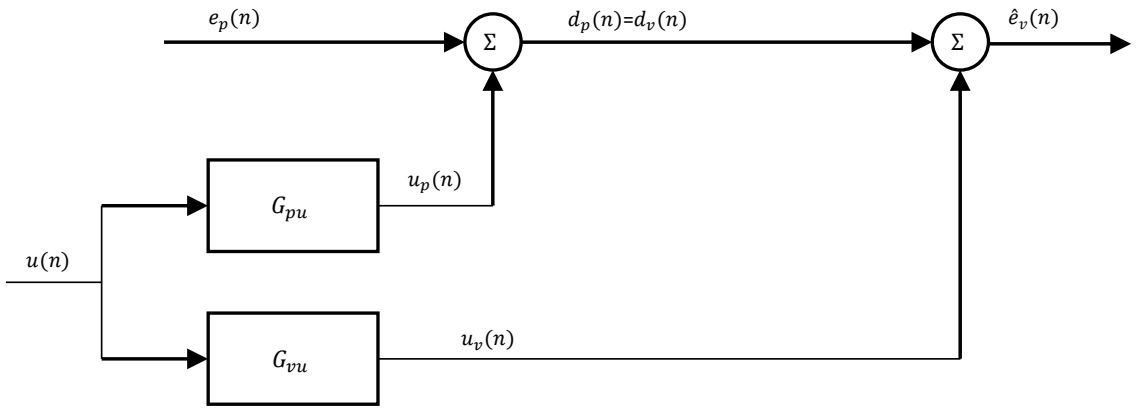


Figure 3.1: Block diagram of the virtual microphone arrangement

The estimated error $\hat{\mathbf{e}}_v(n)$ is then given by the equation,

$$\hat{\mathbf{e}}_v(n) = \mathbf{e}_p(n)[\mathbf{G}_{vu} - \mathbf{G}_{pu}]\mathbf{u}(n) \tag{3.1}$$

Tonal performance has been analyzed in several studies using the VMA; the virtual microphone

arrangement created a zone of quiet that was comparable to that created by directly minimizing the pressure at the virtual locations at low frequencies under 500 Hz. The zone of quiet using the virtual microphone arrangement was significantly smaller for higher frequencies, indicating that the assumption of equal pressure at the physical and virtual microphones becomes less valid as the acoustic wavelength decreases [39]. Garcia-Bonito, Elliott, and Boucher [32] extended Olson and May's design and demonstrated the effectiveness of the virtual microphone arrangement in an active headrest. Using a single channel, feedforward control system using the LMS algorithm; two speakers were used as the secondary speakers to control sound at the left and right ears. This study demonstrated that it is possible to use the VMA to project the zone of quiet away from the secondary source. At low frequencies, the primary acoustic field at the physical and virtual microphone locations are very similar. Therefore, the assumption $\mathbf{d}_p(n) = \mathbf{d}_v(n)$ holds and the controller can attenuate the disturbance sound at the virtual microphone position. At frequencies above 1000 Hz, however, the primary field at the physical and virtual sensor locations is too different and the assumption $\mathbf{d}_p(n) = \mathbf{d}_v(n)$ is not true and the VMA cannot be used. This study found that the head can move laterally without changing the zone of quiet, which is 10 dB.

## 3.2 Remote Microphone Technique

While the VMA has been proven successful in estimating and reducing the noise at virtual locations that are close to the primary disturbance, it struggles in achieving comparable noise control at far-field locations. This degradation in performance can be attributed to the assumption of equal pressure fields at the physical and virtual microphones. This assumption does not hold in virtual sensing applications which aim to reduce the noise at far-field locations. The remote microphone technique (RMT) [35] is an extension of the VMA that does not assume equal pressure at the physical sensor and the virtual location and instead requires a third path. Similar to the VMA, the

RMT uses a preliminary identification process to estimate the required paths. Figure 3.2 shows a block diagram depicting the RMT.

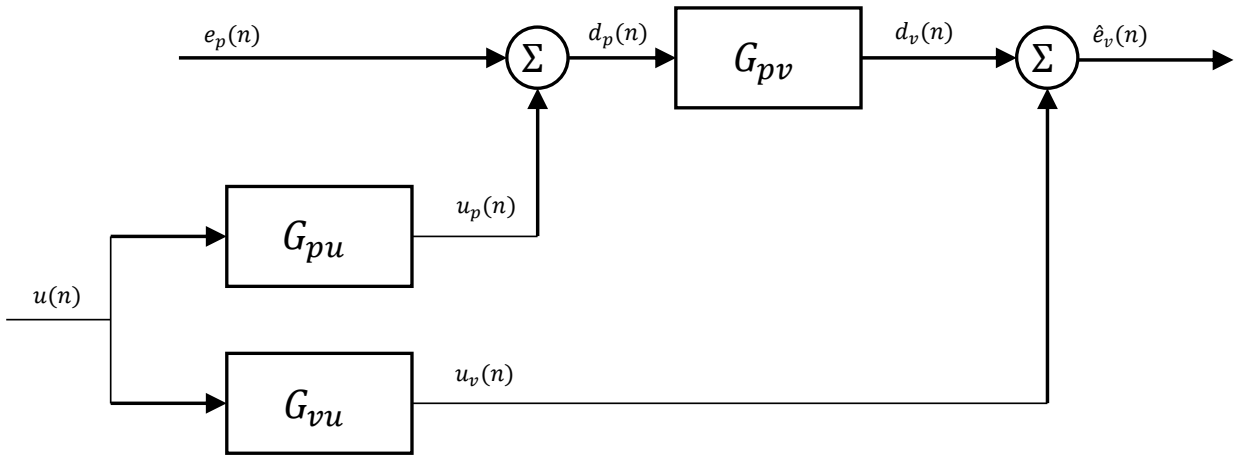


Figure 3.2: Block diagram of the remote microphone technique

Like the VMA, the RMT can also be designed with an unequal number of physical microphones and virtual locations. The primary path $\mathbf{G}_{pv}$ describes the relationship from the physical microphone to the virtual microphone location due to the primary disturbance. The secondary paths from the control signal to the physical error sensor, $\mathbf{G}_{pu}$, and the control signal to the virtual error sensor, $\mathbf{G}_{vu}$, are also estimated during the preliminary identification stage. The paths including virtual microphones use temporarily placed microphones at the virtual locations to identify the paths. The pressure at the physical error sensors due to the primary disturbance is calculated using the equation,

$$\mathbf{d}_p(n) = \mathbf{e}_p(n) - \mathbf{u}_p(n) \tag{3.2}$$

where $\mathbf{e}_p(n)$ is the total measured response at the physical sensor and $u_p(n)$ is the response to the control input at the physical sensor, which leads to,

$$\mathbf{d}_p(n) = \mathbf{e}_p(n) - \mathbf{G}_{pu}\mathbf{u}(n) \tag{3.3}$$

using the relationship $\mathbf{G}_{pu}$ and the total control input, $\mathbf{u}(n)$. The pressure response to the primary disturbance at the virtual error sensor locations is determined by the equation,

$$\mathbf{d}_v(n) = \mathbf{G}_{pv}\mathbf{d}_p(n) \tag{3.4}$$

which uses the path $\mathbf{G}_{pv}$ and the response to the disturbance at the physical sensor, $\mathbf{d}_p(n)$. The estimated response at the virtual location is

$$\hat{\mathbf{e}}_v(n) = \mathbf{d}_v(n) + \mathbf{u}_v(n) \tag{3.5}$$

where the response to the control input at the virtual location $\mathbf{u}_v(n)$ is

$$\mathbf{u}_v(n) = \mathbf{G}_{vu}\mathbf{u}(n) \tag{3.6}$$

using $\mathbf{G}_{vu}$ and the control input $u(n)$ to calculate $\mathbf{u}_v(n)$. The complete equation to estimate the response to a disturbance noise and control input at a virtual location is

$$\hat{\mathbf{e}}(n) = \mathbf{G}_{pv}[\mathbf{e}_p(n) - \mathbf{G}_{pu}u(n)] + \mathbf{G}_{vu}(n)u(n) \tag{3.7}$$

which uses the primary and secondary paths, the signal provided by the physical sensor, and the control input.

Roure and Albarrazin [35] implemented the RMT in an aircraft cabin using twelve virtual microphones, six physical microphones and nine secondary sources. Using this experimental setup, the SPL of the deterministic noise of 170 Hz was reduced by 20 dB at the virtual locations. Comparatively the SPL was reduced 27 dB, when the pressure at the virtual locations was directly measured and fed through the control system. Roure and Albarrazin attributed the difference in reduction between the two strategies to discrepancies in the transfer function which was formed using the RMT. However, Radcliffe and Gogate [45] developed a finite element model which demonstrated that the RMT can theoretically create a perfect estimate of the pressure at the virtual location when the disturbance is tonal and subsequently predictable. In this numerical model, the RMT yielded the same reduction as directly measuring the pressure at the virtual locations. It should be noted that the RMT is limited by the requirement that the physical and virtual microphones must share a causal relationship. Causality requires the physical microphones to provide time advanced information of the disturbance noise to the filter that describes the path from the physical microphones to the virtual microphones. This constraint is removed when the noise being studied is primarily tonal, due to the predictable nature of periodic noise, like in rotating or repetitive machines [40].

Although deterministic noise removes the constraint of causality, this limitation remains in broadband applications. In more recent studies, the remote microphone technique has been applied to reduce the noise of the surrounding environment when a cell phone user is trying to communicate with someone on the far-end [46]. The remote microphone technique was able to estimate the

pressure at the user's ear using the pressure at the location of the cell phone microphone. An ANC system used the pressure estimate to significantly reduce the sound at the user's ear. The RMT has also been used with a head-tracking system for local ANC, which recognizes a change in the user's head position and provides the system with information regarding change in position and the control system adjusts accordingly, demonstrating that the RMT can be effective in applying ANC when an observer location is not fixed [47]. A local head-tracking device was integrated into the local active control system, to monitor movements of the dummy head. The head-tracking system was required to use the appropriate observation filter as the dummy head was moved to the different pre-determined locations. The study found that it was possible to estimate the observation filter at multiple locations; when the separation distance between the physical sensors and error microphones was small the observation filter and physical sensors estimated the disturbance signals at virtual locations with -10 dB or less error. As the separation distance increased, so did the error estimation.

# Chapter 4

# Numerical Modeling

This chapter uses finite element modeling (FEM) to provide insight of the spatial extent of SPL attenuation when ANC is applied to a far-field observer location using COMSOL Multiphysics and to study the VES technology. FEM is generally beneficial in quickly predicting the response of a system by applying relevant boundary conditions, and allows the model configuration to be changed easily. This model is useful in understanding the response at far-field locations when a rotor source radiates sound. Additionally, the model predicts the SPL reduction at surrounding locations after including a control input in the system. Further, the COMSOL model aids in identifying the locations that would be amplified when ANC is applied to a designated observer location in the far-field. The change in SPL under ANC using control microphones at the observer location is compared to the change in SPL under ANC using virtual sensors. The far-field virtual error estimates are established using relationships between the control input and disturbance rotor at near-field and far-field sensors.

## 4.1 Model Configuration

The model is configured in such a way that could be readily replicated during experimental testing, which will be discussed in detail in the following chapter. Figure 4.1 shows the model configuration and the components. The outer perimeter is defined as a perfectly matched layer (PML) that simulates the conditions of an anechoic environment, allowing sound waves to effectively pass through the boundary to infinite free space with no reflection. This condition ensures that the predicted response at some location in the model is purely free-field radiation without reflections. While the outer perimeter of the hemisphere is defined as a PML, the top of the hemisphere is defined as a sound hard boundary to account for symmetry to reduce computation time and storage.

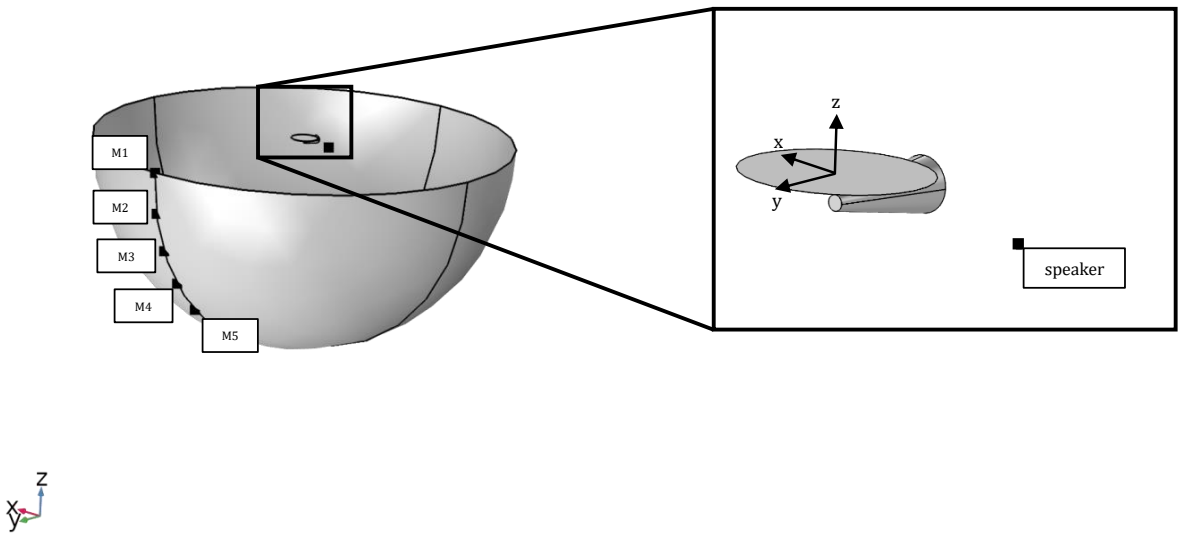


Figure 4.1: Numerical model of the test setup.

The responses at the far-field locations are measured using 5 microphones that are positioned a radial distance of 1.905 meters from the noise source that is located in the center of the model. Figure 4.1 shows how the far-field microphones are positioned relative to the rotor noise source in the center of the model. The elevation angles are evenly spaced, ranging from 0-45°and the

microphones are respectively labeled 1-5. Additionally, Figure 4.1 shows the configuration between the rotor noise source, the conical boom to represent a portion of the airframe, and the loudspeaker. The airframe is positioned directly below the rotor noise source to model a practical rotor-airframe configuration. The noise canceling loudspeaker is modeled using a monopole point source and part of the UAS airframe is modeled in a conical shape for simplicity. Figure 4.2 shows the near-field microphone locations on the conical boom, which represent how the near-field electret microphones were positioned on the airframe during experimental testing to estimate the far-field acoustic pressure response. This study used a mesh size containing 5 elements per wavelength. The model mesh size affects the accuracy of the model; typically, a finer mesh will yield a more accurate model at the cost of greater computation time. The standard criteria in defining the number of mesh elements per wavelength to accurately evaluate the model is between 5 and 10 [48].

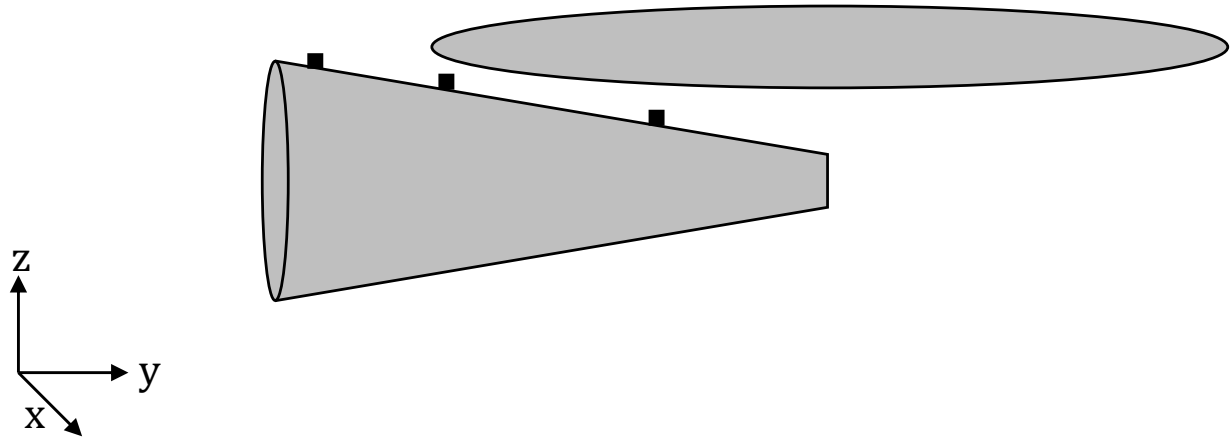


Figure 4.2: Near-field configuration.

The rotor noise source is represented using a rotating ring source, which has been evaluated by Chapman [49] and Prentice [50], who have used the equation

$$h = S_m e^{-imB\theta} \tag{4.1}$$

to characterize the steady thickness noise, $h$, produced by a rotating propeller, where $m$ is the harmonic number, $B$ is the number of rotor blades and $\theta$ is the rotation angle. For example, the harmonic number, $m$, at the BPF is 1, and the blade count, $B$, is 2 for a 2-bladed rotor. The variable $S_m$ is a constant source term. In the study, Prentice developed a numerical model that predicted the field produced by a circular ring source, which represented a non-translating rotating propeller. The numerical predictions closely followed approximations using the given equation. The thickness noise $h$ is periodic to the rotation angle, and as such, equation 4.1 can be treated as a Fourier series. Thickness noise describes the air that is displaced by the rotating propeller blades. Previous work [10] has demonstrated that equation 4.1 can predict the directivity of a 2-bladed rotor. Although equation 4.1 does not account for the loading noise produced by a rotating propeller, the directivity predicted by the model is helpful in understanding the locations of SPL attenuation and amplification when ANC is applied to the system.

The surface model is evaluated in the frequency domain at the frequencies 175 Hz and 200 Hz, which represent the BPFs of a 2-bladed rotor operating at practical in-flight rotor speeds, 5250 and 6000 RPM, respectively. Figure 4.3 shows the rotating pressure field that Equation 4.1 creates while the rotor is operating at 5250 RPM. The frequency domain assumes a harmonically time-varying pressure and Figure 4.3 illustrates the change in phase throughout the system when the rotor noise source is evaluated at a single frequency that corresponds to the rotor BPF at some time $t$ by plotting the real part of the acoustic pressure. The change in pressure demonstrates the difference in phase at the microphone locations.

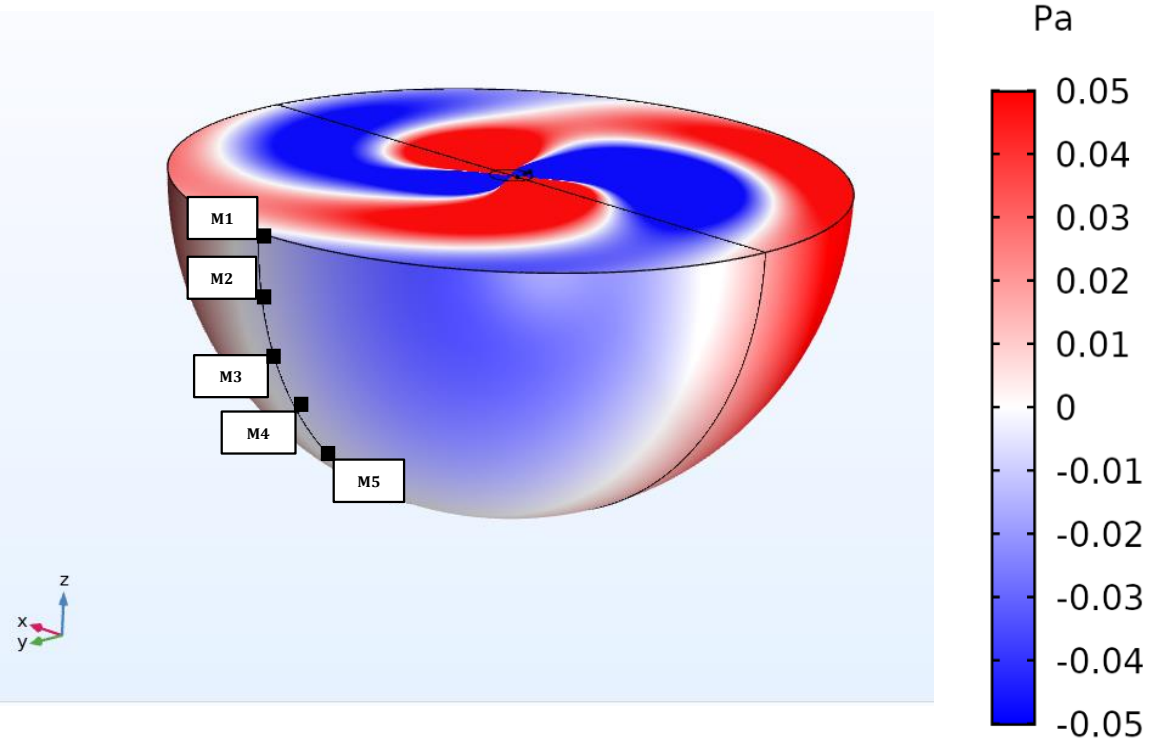


Figure 4.3: The rotating pressure field that models a 2-blade rotor operating at 5250 RPM.

## 4.2 SPL Reduction using Microphones at Observer Locations

The numerical model was used to predict the spatial extent of attenuation. The rotor noise source provided the disturbance noise, and the loudspeaker provided the control input. The loudspeaker control input was modeled as a constant monopole source; a loudspeaker radiates close to that of a monopole if the wavelength is large relative to the size of the speaker. The far-field microphones M1, M3, and M5 were designated as observer locations and will be referred to as observer microphones. This section simulates the spatial change in SPL using physical microphones at the desired location of attenuation to provide the far-field error response in an ANC system.

The SPL reduction to the rotor noise source at a designated observer location is first estimated

using the predicted acoustic pressure at the observer microphone. The rotor noise source and the loudspeaker control input are the only contributors to pressure change in this model, so the far-field pressure, $\hat{e}$, can be estimated through the equation,

$$\hat{e}(e^{j\omega t}) = d(e^{j\omega t}) + G_u(e^{j\omega t})u(e^{j\omega t}) \tag{4.2}$$

in which $d$ is the predicted pressure due to the rotor noise source at the observer location, and $G_u$ is the plant [41]. The plant, $G_u$, quantifies the relationship between the loudspeaker control input $u$ and the observer microphone. Equation 4.2 estimates the total far-field response using the predicted acoustic pressure at the observer microphone. This study aimed to attenuate the SPL at a far-field location caused by a rotor noise source through minimizing the pressure at that location. The loudspeaker control input, $u$, is calculated to drive the acoustic pressure response at the observer microphone to zero using the equation

$$u(e^{j\omega t}) = -G_u^{-1}(e^{j\omega t})d(e^{j\omega t}) \tag{4.3}$$

First, the plant $G_u$ was estimated using the control input with unity amplitude while the rotor noise source was not active. Then, the loudspeaker control input was turned off and the rotor noise source was turned on to determine the predicted pressure at the observer microphone due to the rotor noise source. Equation 4.3 was used to calculate the control input that would theoretically result in a null complex pressure at the virtual location. Once the control input that was required to minimize the pressure at the observer location was calculated, both the rotor and the speaker were turned on with the appropriate control input to simulate ANC at the observer microphone.

The sound pressure level (SPL) is calculated using the equation,

$$SPL = 20log_{10}(p_{rms}/p_{ref}) \tag{4.4}$$

where $p_{rms}$ is the square root of the time-averaged pressure squared. Figure 4.4a shows the predicted time-averaged spatial change in SPL at 175 Hz when M1 was the observer location and the primary disturbance is operating at 5250 RPM. The SPL is reduced most at M1 by more than 20 dB, the SPL at M3 is reduced by 15 dB, and the SPL at M5 is reduced least by about 3 dB. However, other locations in the system are amplified by about 20 dB, verifying the assumption that global ANC cannot be achieved in this particular control system, as the secondary loudspeaker control input and the primary rotor noise source do not radiate noise in the same manner and the two sources are not collocated [10, 51]. Figure 4.4b shows the spatial SPL change when the observer location is M3 at the BPF 175 Hz. Similar to Figure 4.4a, the greatest SPL attenuation is achieved at M3, which is reduced by about 20 dB. The SPLs at the surrounding locations M1 and M5 are less significantly reduced by 10 dB and 5 dB, respectively. Again, the SPLs at locations further from the observer location are reduced least. Additionally, Figure 4.4c shows that when M5 is the observer location, the SPL at M5 is reduced by about 13 dB, but the change in SPL at M1 is negligible.

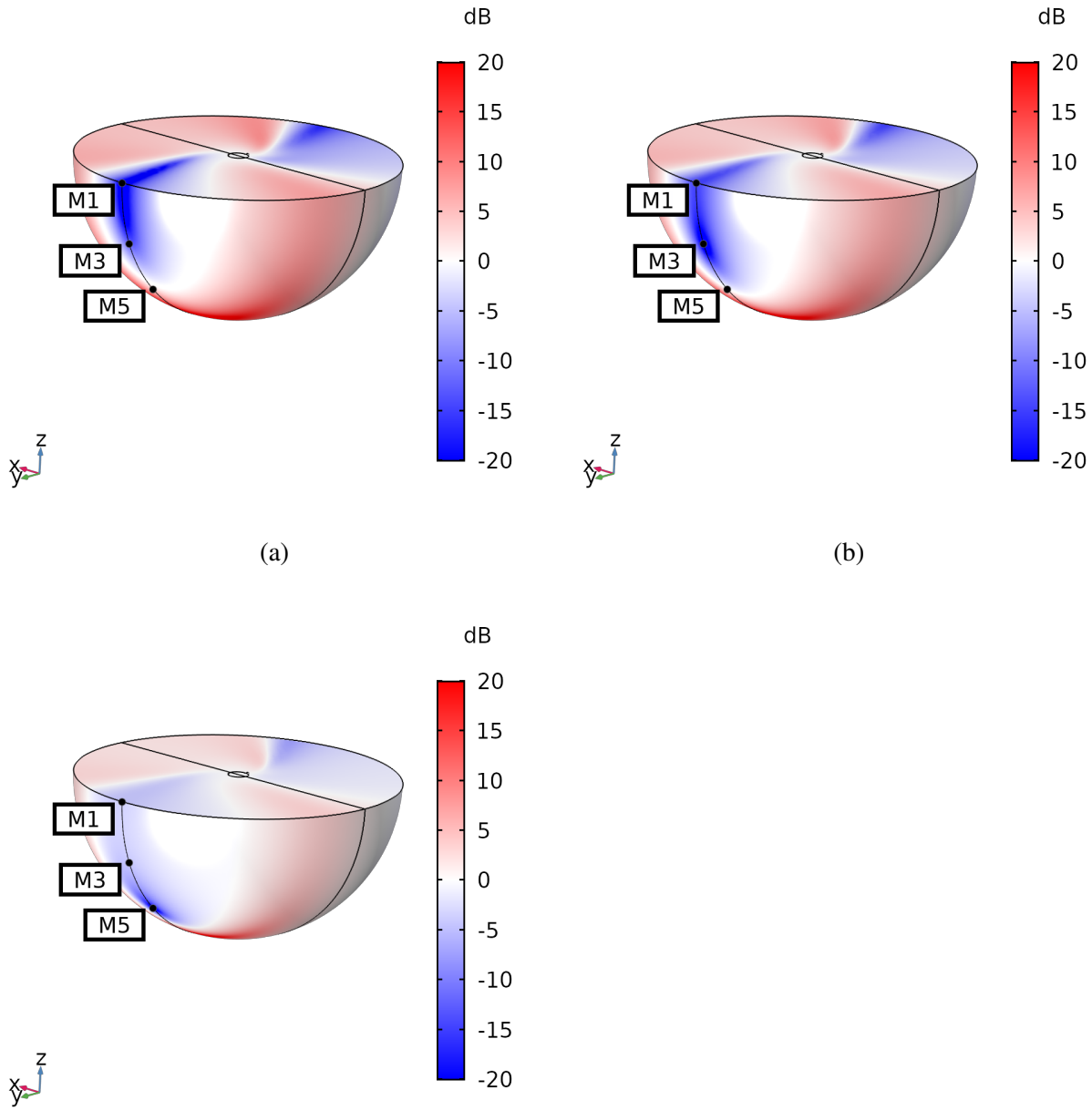


Figure 4.4: Numerical predictions showing the change in SPL at 175 Hz using ANC with an observer microphone located at (a) M1, (b) M3, and (c) M5.

Figure 4.5 shows the predicted time-averaged spatial change in SPL throughout the model at the observer locations M1, M3, and M5 when the model is evaluated at 200 Hz, which represents

the BPF of a 2-bladed rotor operating at 6000 RPM. The SPL attenuation achieved at far-field observer locations at 200 Hz is similar to that predicted in Figure 4.4. In Figure 4.5a, when M1 is the observer location, the SPL of M1 is most attenuated by 20 dB, and the SPL of M5 is reduced least by 2 dB. In Figure 4.5b, M3 is the designated observer location. The predicted SPLs at the surrounding microphones M1 and M5 are also reduced by 10 dB and 5 dB, respectively, suggesting that the entire microphone array is included in the zone of quiet. The spatial change in SPL when M5 is the observer location is shown in Figure 4.5c. The SPL at M5 is reduced most, by around 15 dB, and the predicted SPL at M1 is reduced least, by 4 dB. Similar to Figure 4.4, Figure 4.5 is consistent in showing SPL amplification at some locations within the model, demonstrating that global ANC cannot be achieved when the secondary loudspeaker control input does not radiate in the same manner as the primary rotor noise source and only single input single output (SISO) control is applied to the system.

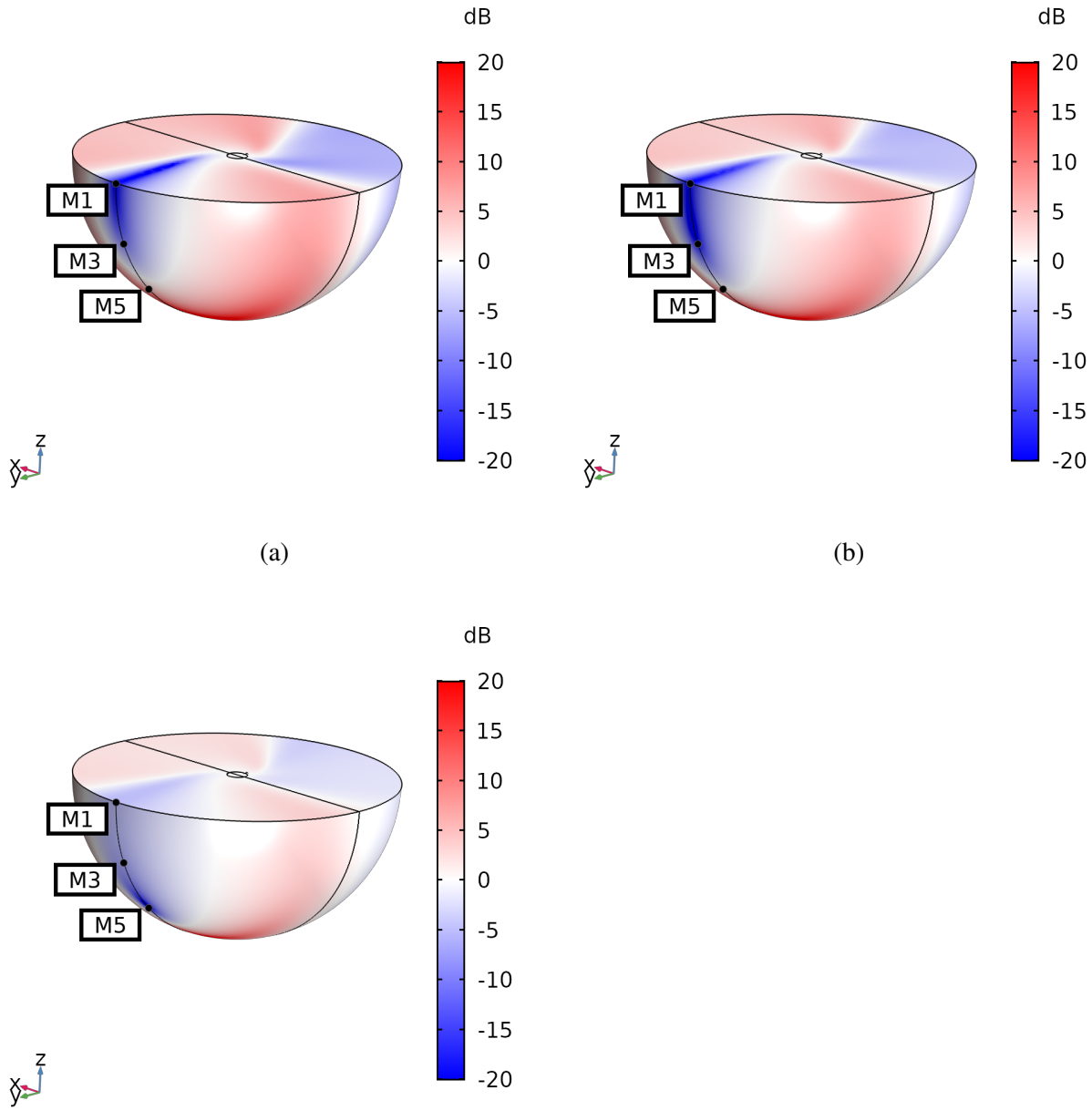


Figure 4.5: Numerical predictions showing the change in SPL at 200 Hz using ANC with an observer microphone targeting, (a) M1, (b) M3, and (c) M5.

### 4.2.1 Summary

This section used the predicted pressure response at the observer microphones M1, M3, and M5 at the BPF of the rotor noise source to apply ANC at these locations. This simulated the spatial change in SPL using a physical microphone at the desired location of attenuation to provide the error response to the ANC system. The observer microphones were defined in locations that were representative of the microphone array used during experimental testing. Generally, the microphone array was located within the predicted zone of quiet. The SPL of the observer microphone that was used to generate the loudspeaker control input was reduced the most. The predicted SPL attenuation was smallest at microphones furthest from the observer microphone. Additionally, this section demonstrated that global ANC could not be achieved, as this model only predicts the spatial change of SISO control.

## 4.3 Establishing the Virtual Error Sensor

After predicting the change in SPL throughout the model using observer microphones at the far-field locations, the spatial extent of attenuation achieved using a virtual error sensor (VES) to apply ANC was assessed. This section simulates ANC using a VES to estimate the response at a far-field observer location. The VES is established using a near-field sensor located on the representative conical airframe.

The VES is established using the remote microphone technique (RMT) [35]. The RMT requires knowledge of the plants, $G_{pu}$ and $G_{vu}$, and observation filter (OF). The plants describe the relationship between the loudspeaker control input and the near-field and far-field sensors and the OF estimated the path from the near-field to the far-field when only the rotor noise source was contributing to the system. The OF was calculated through the near-field and far-field responses

that were predicted through disabling the loudspeaker control input and enabling the rotor noise source. The initial loudspeaker control input with unity amplitude was then applied to the system and the rotor noise source was disabled. The transfer functions $G_{pu}$ and $G_{vu}$ were established. Then, the loudspeaker control input was turned off while the rotor noise source was enabled to establish the OF. The RMT assumes that if the three aforementioned paths along with the known near-field pressure and loudspeaker control input could create an accurate estimate of the virtual error, the remote microphone technique can be applied to perform ANC at the virtual location.

By the principle of linear superposition, the pressure field at the virtual location is the total pressure

$$v_t(e^{j\omega t}) = v_r(e^{j\omega t}) + v_u(e^{j\omega t}) \tag{4.5}$$

where $v_r$ and $v_u$ are the far-field pressure fields caused by the primary noise source and the secondary source, the rotor noise source and the loudspeaker control input, respectively. The response at the virtual location caused by the rotor noise source alone was estimated by

$$v_r(e^{j\omega t}) = OF(e^{j\omega t})p_r(e^{j\omega t}) \tag{4.6}$$

In practice, the near-field physical sensor will provide the total near-field pressure when both the primary and secondary sources are operating. However, the pressure at the physical sensor caused by the rotor noise source and loudspeaker control input individually will not be known directly. Again, linear superposition can be applied to calculate the near-field pressure caused by the rotor noise source

$$p_r(e^{j\omega t}) = p_t(e^{j\omega t}) - p_u(e^{j\omega t}) \tag{4.7}$$

where the total disturbance $p_t$ is provided to the control system by the near-field measurement. The subscripts $r$ and $u$ refer to the rotor noise source and the loudspeaker control input. The loudspeaker control input at the physical sensor $p_u$ is found by

$$p_u(e^{j\omega t}) = G_{pu}(e^{j\omega t})u(e^{j\omega t}) \tag{4.8}$$

The transfer function $G_{pu}$ was determined by setting the loudspeaker control input to unity, and measuring the pressure at the near-field physical sensor. So, the equation that estimates the pressure at the virtual location that is caused by the rotor noise source, $v_r$, is

$$v_r(e^{j\omega t}) = OF(e^{j\omega t})[p_t(e^{j\omega t}) - G_{pu}(e^{j\omega t})u(e^{j\omega t})] \tag{4.9}$$

The pressure response to the loudspeaker control input at the virtual location is

$$v_u = G_{vu}(e^{j\omega t})u(e^{j\omega t}) \tag{4.10}$$

Therefore, the total estimate of the far-field pressure is the sum of the pressure caused by the rotor noise source and the loudspeaker control input

$$\hat{e}(e^{j\omega t}) = OF(e^{j\omega t})[p_t(e^{j\omega t}) - G_{pu}(e^{j\omega t})u(e^{j\omega t})] + G_{vu}(e^{j\omega t})u(e^{j\omega t}) \tag{4.11}$$

The virtual error estimate was subsequently used to calculate the loudspeaker control input required to minimize the pressure at the observer location obtained from the VES. The reduction using this estimate was compared to the reduction achieved using the measured pressure at the observer location. Using equation 4.11 to drive the virtual error estimate to zero when the loudspeaker

control input is applied, the loudspeaker control input was found to be equal to

$$u(e^{j\omega t}) = -[G_{vu}(e^{j\omega t}) - OF(e^{j\omega t}G_{pu}(e^{j\omega t}]^{-1}OF(e^{j\omega t}p_r(e^{j\omega t}) \tag{4.12}$$

## 4.4 SPL Reduction at Observer Locations using a VES

Figures 4.6 and 4.7 show that the predicted SPL at the observer location is attenuated by about 20 dB using a VES to calculate the loudspeaker control input. The model was evaluated at the BPFs 175 Hz and 200 Hz, shown in Figures 4.6 and 4.7, respectively. Very similar levels of attenuation were achieved using an observer microphone to determine the loudspeaker control input. The change in SPL throughout the model when M1 was the observer location and the model was evaluated at 175 Hz is shown in Figure 4.6a. While the model predicted significant SPL attenuation at M1 and M3, the predicted SPL attenuation at M5 was small, about 3 dB. The change in SPL when M3 was used as the observer location is shown in Figure 4.6b. Similar to Figures 4.4b and 4.5b, the SPL attenuation is greatest at M3. Here, the SPL is reduced by 20 dB, and the SPLs at M1 and M5 are reduced as well. Figure 4.6c shows the change in SPL throughout the model when the observer location is M5. The SPL attenuation is greatest at M5. Here, the SPL is attenuated by 16 dB, while the change in SPLs at M3 and M1 is negligible. Figure 4.7 shows the change in SPL at the observer locations when the model was evaluated at 200 Hz; the changes in SPL throughout the model are similar to those shown in figure 4.6. Additionally, the change in SPL in figures 4.6 and 4.7 are nearly identical those achieved in figures 4.4 and 4.5.

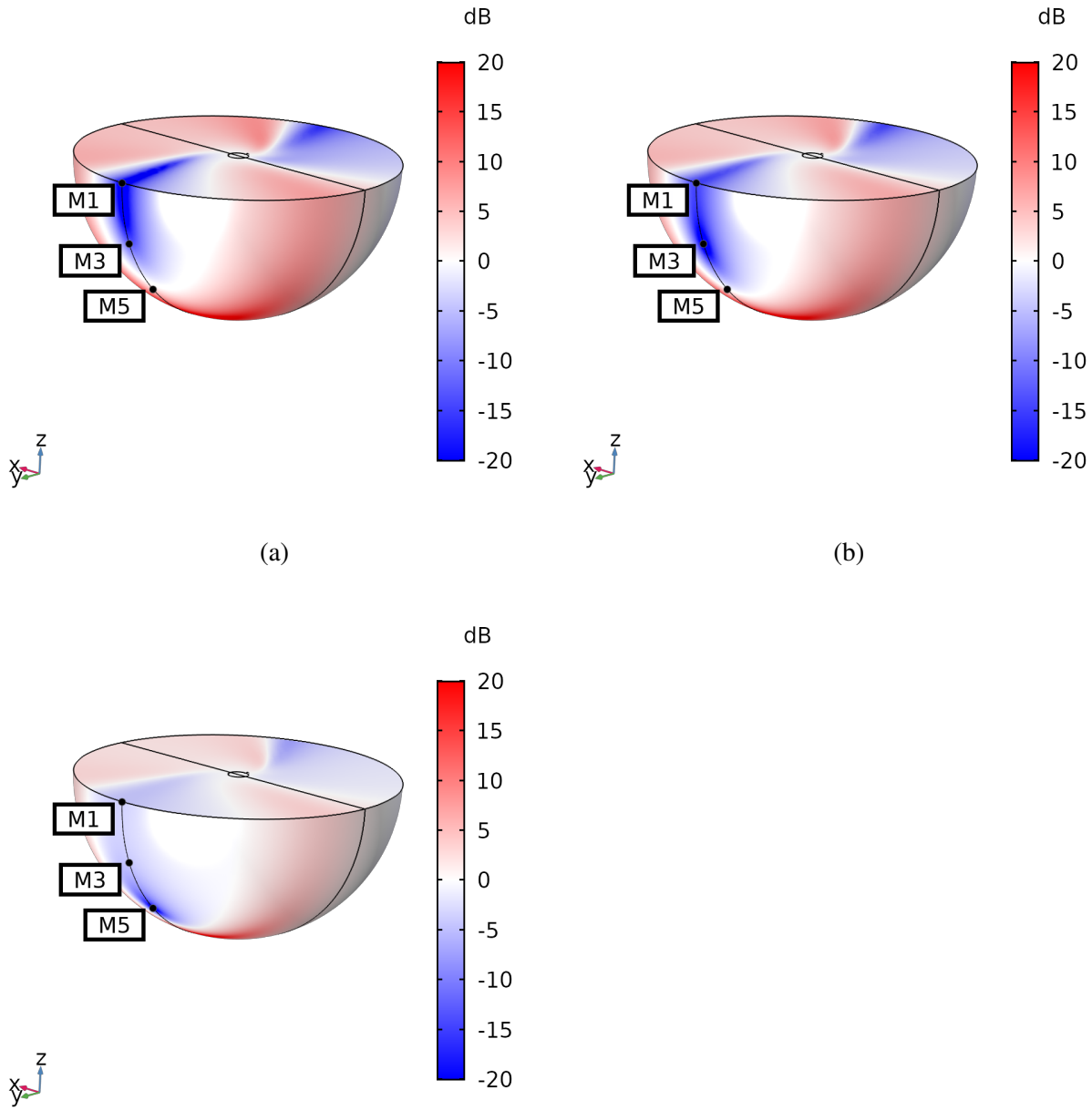


Figure 4.6: Numerical predictions showing the change in SPL at 175 Hz using ANC with a VES targeting, (a) M1, (b), M3, and (c) M5.

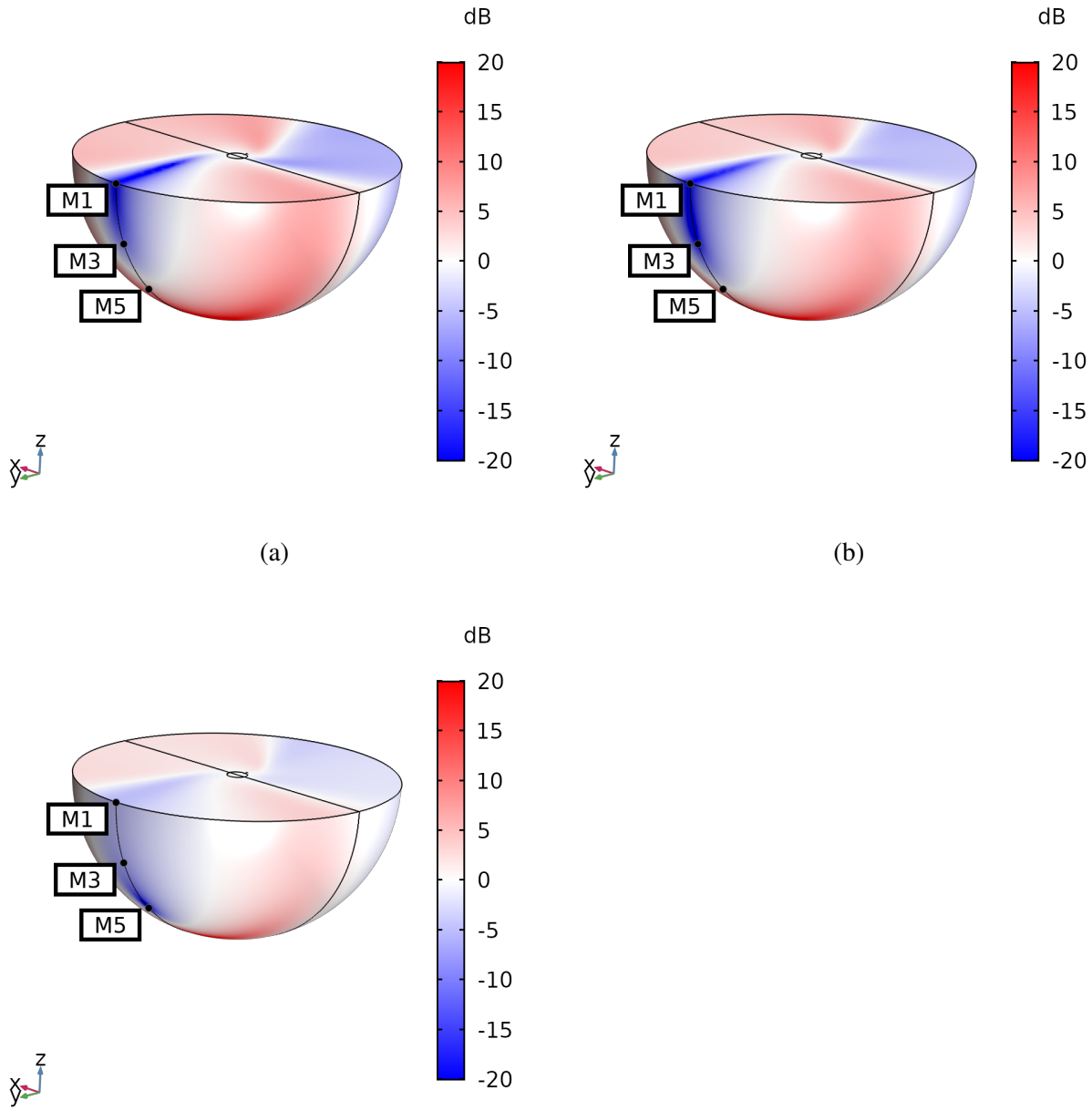


Figure 4.7: Numerical predictions showing the change in SPL at 200 Hz using ANC with a VES targeting, (a) M1, (b), M3, and (c) M5.

### 4.4.1 Summary

This section generated the loudspeaker control input using a virtual error sensor to estimate the far-field pressure response at the location of attenuation at the rotor BPFs 175 Hz and 200 Hz, which correspond to the rotor rotation rates 5250 RPM and 6000 RPM. The VES was established using the remote microphone technique and a predicted near-field pressure response from a location that was representative of a near-field sensor location that was used in experimental testing. The targeted locations of attenuation were M1, M3, and M5. The loudspeaker control input that was generated using a VES achieved nearly 20 dB of SPL attenuation at the targeted locations, while the SPL attenuation at locations further from the targeted location was much less. The predicted spatial change in SPL is similar to that achieved in 4.2.

## 4.5 Discussion

This chapter studied the predicted spatial change in SPL using a loudspeaker control input to cancel the sound generated from a primary noise source at some targeted location. The rotor noise source was studied at the BPFs (175 Hz and 200 Hz) corresponding to the rotor rotation rates 5250 RPM and 6000 RPM. The SPL reduction at observer locations when the far-field pressure response is directly used to calculate the control input is very similar, within 1 dB, to the SPL reduction achieved when the virtual sensors are used to calculate the loudspeaker control input. This is consistent for each observer location (M1, M3, and M5). The SPL attenuation achieved when observer microphones are used to calculate the loudspeaker control input was about 20 dB at each observer location. Similarly, the SPL at the observer location is attenuated by about 20 dB when a virtual sensor estimated the far-field response and subsequently determined the control input. This suggests that the remote microphone technique can provide an appropriate estimate of the response at the far-field location. Additionally, the level of SPL attenuation experienced

at surrounding microphone locations using an observer microphone to generate the loudspeaker control input matches that achieved using a VES to generate the loudspeaker control input. The SPL at M5 is reduced the least when M1 is the designated far-field location, and M1 is reduced the least when M5 is the targeted far-field location. When M3 is the observer location, the SPLs at M1, M3, and M5 are simultaneously reduced, which indicates that each microphone is included in the zone of quiet.

While the predicted level of SPL attenuation throughout the model was the same using observer and virtual microphones, the locations of amplification were similar. As expected, when the monopole loudspeaker introduced the control input to the system, locations throughout the sound field that were not in phase with the observer location were amplified. This follows with the understanding that global attenuation cannot be achieved if the primary and secondary sources do not radiate sound in the same manner and only a SISO system is used. Although this model does not capture the loading noise that a rotating propeller produces, it provided insight to the spatial extent of attenuation using a VES to apply ANC at a far-field location. The level of SPL attenuation achieved using observer microphones was consistent with that achieved using a VES, verifying that the RMT could be applied to the system and achieve SPL reduction.

# Chapter 5

# Experimental Testing

This chapter details the experimental setup and the methods that are used to establish a virtual error sensor (VES). The VES is subsequently used to apply ANC on radiated sound from a UAS rotor at a remote location. The filtered-x LMS (FxLMS) algorithm was applied to the remote microphone technique (RMT) to implement ANC in real-time based on the reference signal provided by the optical tachometer and the pressure measured by a sensor on an airframe. The closed-loop SPL at the BPF and harmonics of two common operational rotor speeds were examined during open-loop and closed loop data collection. Two sets of closed-loop measurements were compared: traditional ANC which used a physical microphone to measure the far-field pressure response, and ANC using the virtual sensor to provide the error estimate.

## 5.1 Experimental Setup

Experimental testing was conducted in NASA Langley's Structural Acoustic Loads and Transmission (SALT) anechoic chamber. Foam wedges line the walls, ceiling, and floor of the chamber to create an anechoic environment that absorbs sound above 100 Hz. The noise source was a single

rotor with two-blades with a tip radius of 11.94 cm, which was secured to a test stand located in the center of the chamber. The rotor was connected to a motor that was driven using an electronic speed controller (ESC). A 3D printed cone was used to represent part of a small UAS airframe. Electret microphones were embedded into the cone to measure the near-field acoustic pressure response of the rotor noise and secondary loudspeaker. A Kulite pressure transducer was secured to the cone using electrical tape to provide supplementary near-field data. A 5 microphone array located 1.905 meters from the rotor test stand captured the far-field pressure response. A 7.62 cm diameter loudspeaker was used as the secondary source to provide the noise-canceling sound to the system. The center of the loudspeaker was positioned next to the cone, 8.89 cm below the rotor plane, offset 13.97 cm to the left of the far-field microphone array, and was offset 17.78 cm from the center of the rotor. Measurements were collected when the airframe was positioned in-line and perpendicular relative to the microphone array. Figure 5.1 shows the near-field and far-field test configuration, including the rotor and boom to represent part of a small UAS airframe. The microphones labeled M1, M3, and M5 were designated observer locations, where ANC would be applied to reduce the SPL. Microphones M2 and M4 provided supplementary information on the change in SPL at surrounding microphones when ANC is applied to a designated observer location.

(a) (b)

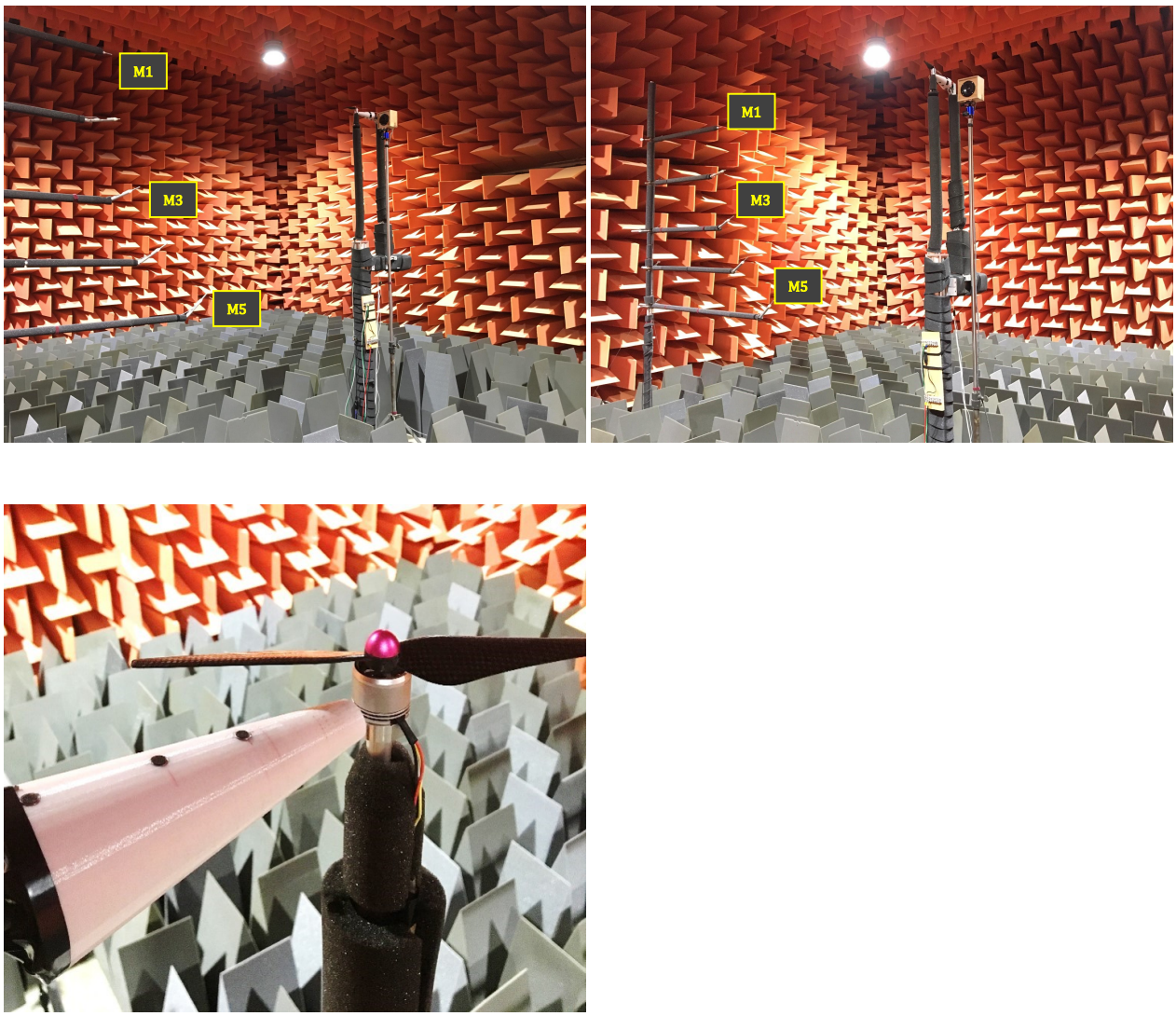


(c)

Figure 5.1: (a) Test setup when the cone is in-line with the microphone array. (b) Test setup when the cone is perpendicular with the microphone array. (c) Electrets embedded in the cone.

## 5.2 Components

### 5.2.1 Control System Hardware

The control system was implemented using a Speedgoat Real-Time target machine and corresponding I/O 104 board to the target computer. The signals were processed on the target computer using Matlab and Simulink. Low-pass anti-aliasing and reconstruction filters with a cutoff frequency of 1500 Hz were used on both the inputs and outputs of the digital controller. Filtering was performed with a PCB Piezotronics signal conditioner. The signal conditioner has both voltage and current inputs and outputs. The signal conditioner voltage output associated with the control output was connected to the input of a TFM-42 Carver Amplifier. The amplifier output provided the gain and power to the control speaker. Figure 5.2 shows how the hardware interacts with the sensors. Individual components are explained in more detail below.

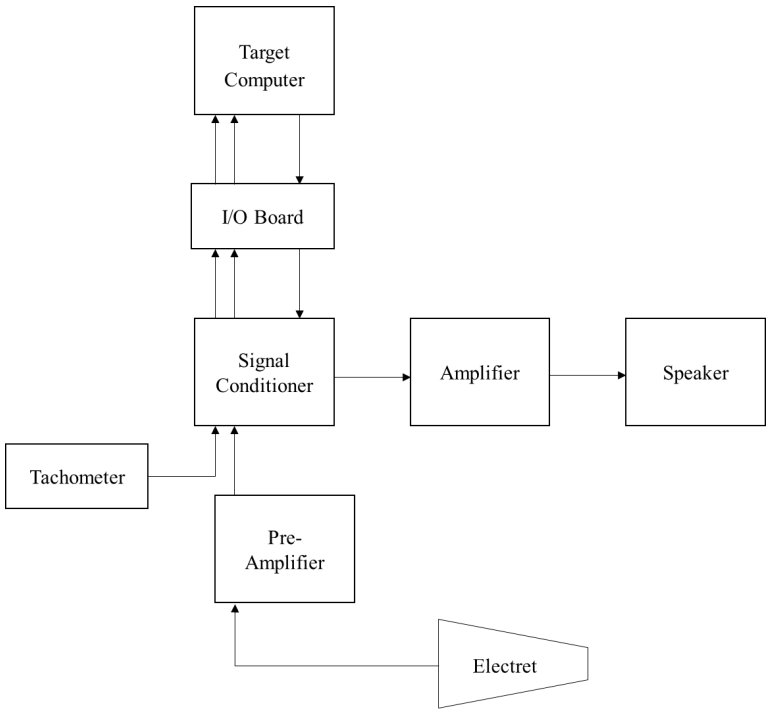


Figure 5.2: Diagram illustrating the arrangement of the control system hardware components.

**Rotor**

A brushless DJI 2212 motor was secured to a test stand and placed in the center of the anechoic chamber, 1.90 m offset from the far-field microphone array. A carbon fiber (CF) replica of a two-blade DJI propeller served as the rotor during experimental testing. The rotor stood 3.20 m above the floor. The rotor's radius was 119 mm. The rotor was mounted to the motor, which was controlled by a DJI Opto E300 ESC. A Sorenson DC power supply provided the required 14.8 V and up to 15 A to the motor. The rotation speed of the motor was set using a Pololu USB servo controller.

### Airframe

The airframe was represented as a conical long boom which traditionally supports the rotor and motor in a real drone application. Including a representative airframe is beneficial while collecting data because the interaction effects with the cone change the acoustic pressure response at the far-field microphones. Additionally, the airframe provides a location where near-field sensors can be positioned in a practical application. The cone was mounted to a test stand which was placed directly under the rotor, to mimic the configuration of a UAS airframe and rotor. The cone was 163 mm long, 51 mm tall, and had a minor and major diameter of 20 mm and 70 mm, respectively. The cone was placed 11.98 mm below the rotor; the ratio of separation distance to rotor tip radius $\delta$/R was -0.1. Data was collected when the airframe was positioned at the azimuthal angles 0 and 90 degrees relative to the microphone array.

### Near-field Sensors

A Kulite pressure transducer was used to verify the dynamic range of the electret microphones. The Kuite transducer was secured to the cone using electrical tape; the Kulite was initially chosen due to its high dynamic range, affording confidence in the pressure measurements at the harmonic content. A Hewlett Packard DC power supply provided 12 V and 16 mA to the Kulite. Three electret microphones were embedded into the cone. Electret microphones were used in favor of the Kulite transducer due to their low noise floor and low cost, making them easier to be used in practical applications. The electrets were positioned in a straight line on the cone so that their diaphragms were flush with the surface of the cone. The electrets were labeled Electret 1, Electret 2, and Electret 3. Electret 1 was positioned furthest from the rotor, Electret 2 was directly under the rotor tip, and Electret 3 was positioned closest to the rotor, which can be seen in Figure 5.1. The electrets were paired with pre-amplifiers. The electrets were subsequently passed through a

PCB Piezotronics signal conditioner using the cutoff frequency 1500 Hz.

### Far-field Sensors

Five Bruel&Kjaer (B&K) Type 4939 microphones and Type 2670 pre-amplifiers were used to measure the sound pressure in the far-field. They were placed in the microphone array located 1.905 m away from the motor stand at inclination angles 0, 11.25, 22.5, 33.75, and 45 degrees and were labeled 1-5, respectively.

### Optical Tachometer

A Monarch Instrument optical tachometer was used to provide a reference signal to the ANC system. The tachometer laser was positioned to detect a reflective strip placed on the motor and provided RPM measurements to the control system after the analog tachometer signal was converted to the digital domain using the ADC. The tachometer signal output was post-processed using the built-in Matlab function "tachorpm," which extracts an RPM signal from the tachometer pulse signal using a 10 coefficient B-spline least squares filter to avoid overfitting.

### Active Speaker

A 7.62 cm diameter Dayton audio enclosed speaker, model DSA90-8, provided the control input to the system. The speaker was mounted to a test stand and was placed on the left side of the cone to simulate a probable location in practical applications. The center of the speaker was positioned 8.89 cm below the plane of the rotor and was offset 17.78 cm from the center of the rotor. Additionally, the speaker center was offset 13.97 cm to the left of the microphone array. Although the speaker is too large to place on the body of the cone and would not be used in a practical application, this speaker can help identify limitations of the system setup relative to testing the use of

virtual error sensors.

### 5.2.2 Control System

Refer to Figure 5.2. The control system was applied on the target computer using a Speedgoat Real-Time target machine I/O 104 board. The digital control system applied the filtered-x LMS algorithm (FxLMS) and updated the controller using Matlab and Simulink software, which will be further discussed below. As previously mentioned, the target computer was used to implement real-time control. The sample rate of the target computer was 5000 Hz. The reference tachometer signal and the near-field electret microphone provided inputs to the control system.

#### Controller

Figure 5.3 shows the block diagram of the filtered-x LMS algorithm, which was used in this study to update the controller. The FxLMS algorithm adapts the LMS algorithm to include the path from the loudspeaker to the far-field microphone location, $\hat{G}_{vu}$. The equation,

$$x'(n) = \hat{G}_{vu}x(n) \tag{5.1}$$

filters the tachometer reference signal $x(n)$ through $\hat{G}_{vu}$. The reference signal and the error signal, $\hat{e}(n)$, are then used to update the controller, $W(z)$ using the update equation

$$\mathbf{w}(n+1) = \mathbf{w}(n) + \mu\mathbf{x}'(n)\hat{e}(n) \tag{5.2}$$

and the control input, $u(n)$ is generated.

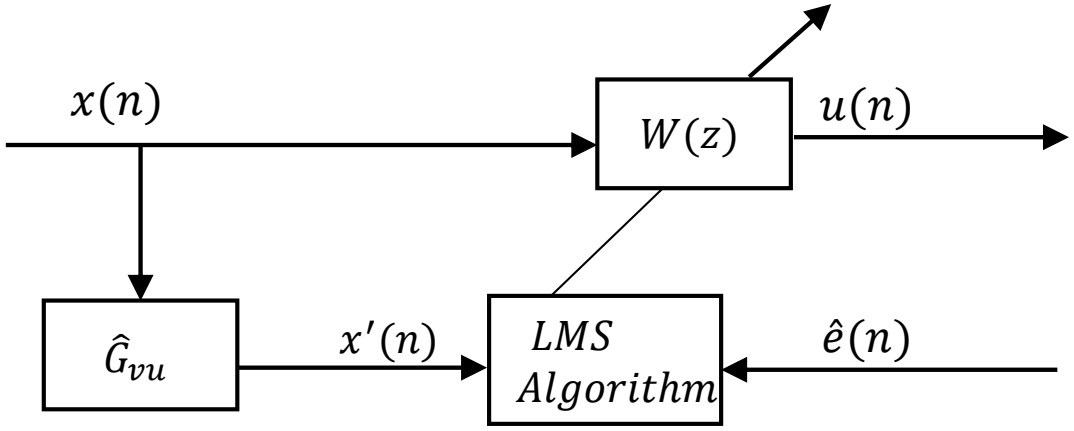


Figure 5.3: Block diagram of feedforward control using the FxLMS algorithm.

**Virtual Error Sensor System**

The remote microphone technique was used to establish the virtual error sensor during experimental testing. The block diagram shown in Figure 5.4 illustrates how the remote microphone technique was implemented within a Simulink model to create the virtual error estimate.

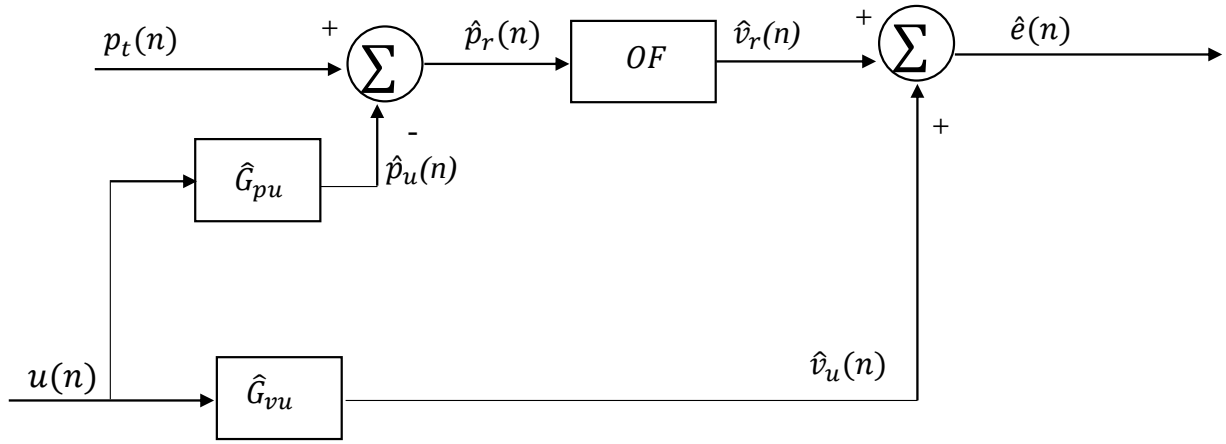


Figure 5.4: Block diagram of the remote microphone technique.

The tachometer provided the reference signal to the control system, and the electret measured the near-field acoustic pressure. These signals were processed by the VES system to establish a useful estimate of the acoustic pressure response at the far-field microphone. The physical microphones in the far-field were only used to view the pressure at these locations and did not affect the control system. The remote microphone technique was applied to create an estimate of the far-field pressure, which provided the error measurement in the FxLMS algorithm.

The OF captures the linear relationship between the near-field sensor and the far-field microphone and was estimated during a preliminary identification step, which will be discussed in detail in section 5.3. The transfer functions from the control signal to the near-field sensor, $\hat{G}_{pu}$, and from the control signal to the far-field (virtual location), $\hat{G}_{vu}$, are also estimated during the preliminary identification step. The pressure in the near-field due to the rotor is calculated as

$$\hat{p}_r(n) = p_t(n) - \hat{p}_u(n) \tag{5.3}$$

where $p_t$ is the total measured near-field response and $\hat{p}_u$ is the near-field response due to the loudspeaker, which leads to

$$\hat{p}_r(n) = p_t(n) - \hat{G}_{pu}u(n) \tag{5.4}$$

using the transfer function $\hat{G}_{pu}$ and the loudspeaker signal, $u$. The pressure response due to the rotor at the far-field (i.e., virtual error sensor) location is determined by the equation

$$\hat{v}_r(n) = OF\hat{p}_r(n). \tag{5.5}$$

The estimated far-field response is

$$\hat{e}(n) = \hat{v}_r(n) + \hat{v}_u(n) \tag{5.6}$$

where $\hat{v}_u$ is the far-field response due to the loudspeaker, defined as

$$\hat{v}_u(n) = \hat{G}_{vu}u(n). \tag{5.7}$$

The complete equation to estimate the far-field response due to the rotor and loudspeaker is

$$\hat{e}(n) = OF[p_t - \hat{G}_{pu}u(n)] + \hat{G}_{vu}u(n), \tag{5.8}$$

which uses the transfer functions, the near-field measurement, and the loudspeaker signal.

**Hardware and Control System**

Figure 5.5 illustrates how the hardware interacted with the control system and how the control system established the virtual error estimate. The hardware is shown outside the bounds of the dotted line, and the digital control system is contained within the dotted line. The digital control system was implemented within Simulink, where a virtual error sensor was established using the RMT, and the controller was updated using the FxLMS algorithm. A 6th order bandpass digital Butterworth filter from 50-425 Hz was applied to the reference signal and the near-field signal to reduce the amplitude of the DC offset and higher harmonic content while also including the shaft harmonic up and the first several rotor harmonics at each of the rotation rates that were considered in this study. The reference signal, provided by the tachometer, was filtered using the secondary path between the control input and the far-field microphone, $G_{pu}$. The filtered reference signal was then passed through the LMS algorithm. Here, the controller was updated and the adaptive

filter coefficients were established. The controller contained 1024 filter coefficients. The controller output a control signal which was then passed through the DAC and signal conditioner. This control output signal was ultimately passed through the loudspeaker to attenuate the SPL at the designated far-field observer location. Figure 5.5 also shows where the RMT is used to establish the virtual error estimate, $\hat{e}(n)$.

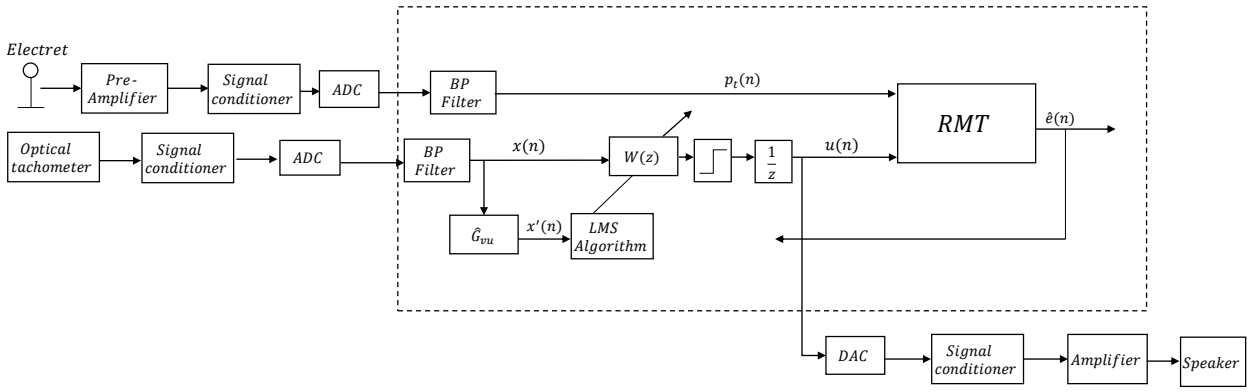


Figure 5.5: Diagram of the external hardware and digital control system used to establish a virtual error sensor.

Figure 5.5 shows that a saturation limit was used to prevent the control input from growing too large and subsequently providing the speaker with more than the maximum allowable voltage. Additionally, a one sample delay was included in the block diagram after the control input signal is created to prevent an algebraic loop from being created in Simulink. An algebraic loop can be formed when the system requires a value that is not yet available.

## 5.3 Methods

It should be noted that these tests used two computer systems: the target computer, to implement real-time control, and one that was used for data acquisition. The sampling rate of the data acquisition computer was 50 kHz over a total sampling time of 20 seconds. The rotor speed was chosen

on the data acquisition computer. Data acquisition began once the rotor converged to the desired rotation speed. Once the data set was collected, the rotor speed was zeroed and the next data set was collected after at least 20 seconds to limit flow recirculation in the chamber. Recirculation will likely not affect the system in an open air environment, like an in-flight UAS that is operating outdoors. However, flow recirculation can occur while the rotor is operating in an enclosed space, and can amplify the higher harmonics by more than 15 dB [6].

Since testing was conducted in an anechoic chamber, the effects of flow recirculation were mitigated by waiting for the air to settle after collecting data before collecting another set. The rotor was mainly operated at speeds of 5250 and 6000 RPM. Microphones 1, 3, and 5 were chosen as targeted locations of control, and Microphones 2 and 4 provided supplementary far-field sensor pressure responses. Data sets during which no control input was applied are referred to as open-loop; closed-loop data sets refer to those during which ANC was turned on. Closed-loop data sets were collected as follows: the rotor was turned on and allowed to converge to the set speed, then the control system was enabled and the adaptive filter was allowed to converge. Once the control system was converged, data acquisition began. After the acquisition period of 20 seconds, the rotor and control system were turned off. Control was either applied using a physical microphone to provide the error response to the system or using a virtual sensor that estimated the far-field error based on the VES filtered signal from near-field electrets.

The B&K microphones were calibrated using a GenRad pistonphone sound level calibrator. The calibration tone was 500 Hz at 94 dB SPL as the reference level. The pistonphone was positioned over the microphone diaphragm while the tone played and the microphone response was measured for 10 seconds. The microphone response was compared to the reference level at 500 Hz and the unique sensitivity in units of mV/Pa was calculated.

First the far-field SPL created by the isolated rotor with no airframe included in the setup was measured, which was useful in comparing how the addition of an airframe changes the acoustic

far-field pressure response. The isolated rotor was observed at 5250 and 6000 RPM. An open-loop test that included the cone measured the far-field SPL at the rotor BPF and harmonics over the range of 5000-5500 RPM, in increments of 50 RPM. These initial tests were conducted to determine the feasibility in estimating the far-field pressure given near-field measurements. Later tests also applied ANC with both a physical microphone and a VES providing error signals to the control system.

### 5.3.1 System Identification

Feedforward ANC requires knowledge of the plant, which describes the acoustic path between an input signal and the response at the desired location of attenuation, prior to noise control. This estimation step is referred to as system identification. System identification uses a reference microphone to measure the input disturbance noise and passes the input signal through a filter to create an estimate of the plant. The plant output is the desired signal response for the adaptive filter and includes the effects of the system's physical components: the anti-aliasing filters, the ADC/DAC, power suppliers, amplifier, and the speaker and far-field microphone responses. The FxLMS algorithm, that was implemented within a Simulink model and used during testing, requires the identification of the plant between the control actuator, usually provided by a noise-canceling loudspeaker, and the desired location of attenuation, measured by the error sensor.

The active loudspeaker was positioned as previously described in 5.2.1 and the preliminary system identification was performed. The speaker outputted band-limited white noise and the far-field microphone measured the pressure response for 10 seconds. The data was separated into halves in terms of the time record. The first 5 seconds were used to create a frequency response model and the last five seconds were used to validate the model. Then, the Wiener filter calculated the optimal filter coefficients using the model data set. The Wiener filter calculates the optimal FIR

filter coefficients by the equation 2.5.

In order to perform ANC with a virtual error sensor, three paths must be identified: an observation filter (OF) between the physical error sensor and the virtual error sensor due to the disturbance noise, the plant $\hat{G}_{pu}$ from the control signal to the physical error sensor, and the plant $\hat{G}_{vu}$ from the control actuator to the virtual location. Figure 5.6 illustrates how the RMT was used in the control system to establish the virtual error estimate, $\hat{e}(n)$. An electret microphone served as the physical error sensor, and the far-field microphones served as the virtual location. The microphones at the virtual locations were only used to identify the paths during the system identification and to view how the SPL at these locations changed during open and closed loop data collection.

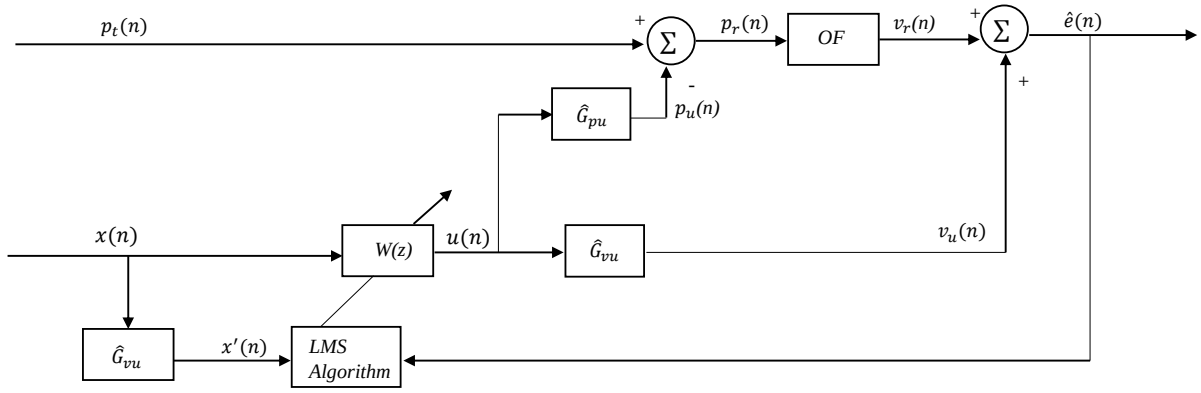


Figure 5.6: Diagram the digital controller using a virtual error sensor.

The $OF$ was estimated by measuring the pressure response at the electret and the far-field microphones when the rotor was turned on to 5250 RPM. The data was split into halves, one half was used to create a model and the other a validation set. Then, the optimal filter coefficients were calculated using the Wiener filter and the model data set. The measured transfer function was

estimated using the validation data and compared to the estimated frequency response at the BPF and harmonics. The filter coefficients were then saved. This was repeated each time the rotation rate was changed. Then, broadband noise was played through the control speaker and the acoustic pressure at the electret was recorded to estimate the path $\hat{G}_{pu}$. Again, the Wiener filter was used to create a model, which was compared to the measured transfer function. The coefficients were then saved. This was repeated to estimate the path $\hat{G}_{vu}$.

### 5.3.2 Active Noise Control using a Physical Error Sensor

ANC was applied at a designated far-field observer location using the output of a microphone located at the observer location as the error signal for the control system. Figure 5.7 shows the external hardware and the digital control system interact when a physical microphone was used to provide the error estimate $e(n)$ to the system. The plant $G$ was between the control speaker and the far-field microphone. The FxLMS algorithm was used to update the controller. The reference signal, measured by the optical tachometer, was filtered by the plant estimate $\hat{G}$ to compensate for system delay. The filtered reference signal and the error signal were passed through the LMS algorithm and adaptive controller to create an appropriate control input. The control input was played through the loudspeaker and subsequently canceled the disturbance produced by the rotor.

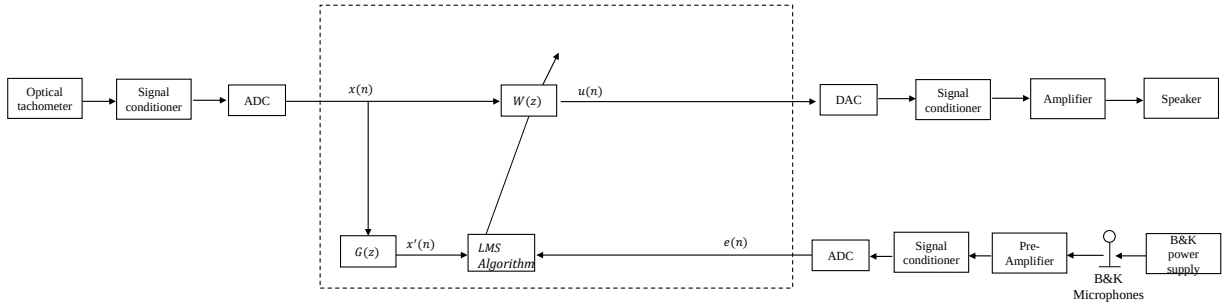


Figure 5.7: Block diagram showing the external hardware and digitial control system using a physical error sensor at the desired location of attenuation.

## 5.4 Verifying Equipment

As previously mentioned, the RPM signal was extracted from the tachometer pulse signal, which was used as a reference signal in the control system. The RPM signal was extracted to verify that the tachometer pulse signal corresponded to the user defined rotor speed. Figure 5.8 shows the raw tachometer pulse signal. Figure 5.9 shows a comparison of the corresponding raw and smoothed rotation rate in RPM. Smoothing was achieved using a 10 coefficient B-spline least squares filter. The rotor BPF (in Hertz) was calculated using

$$BPF = \frac{nt_{RPM}}{60} \tag{5.9}$$

where $n$ is the number of propeller blades and $t_{RPM}$ is the tachometer RPM output.

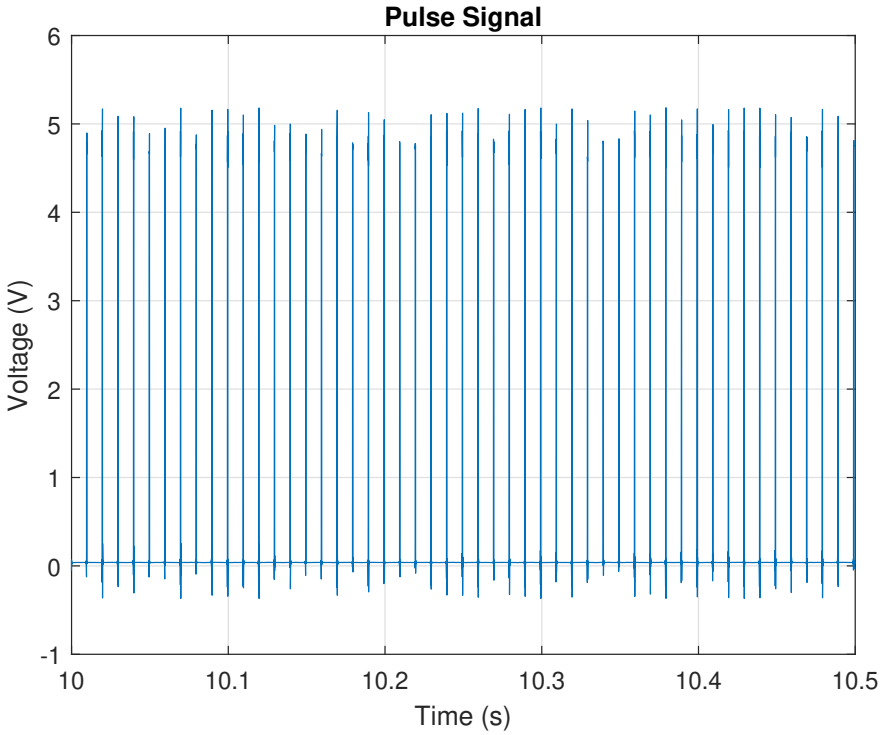


Figure 5.8: Representative tachometer pulse signal.

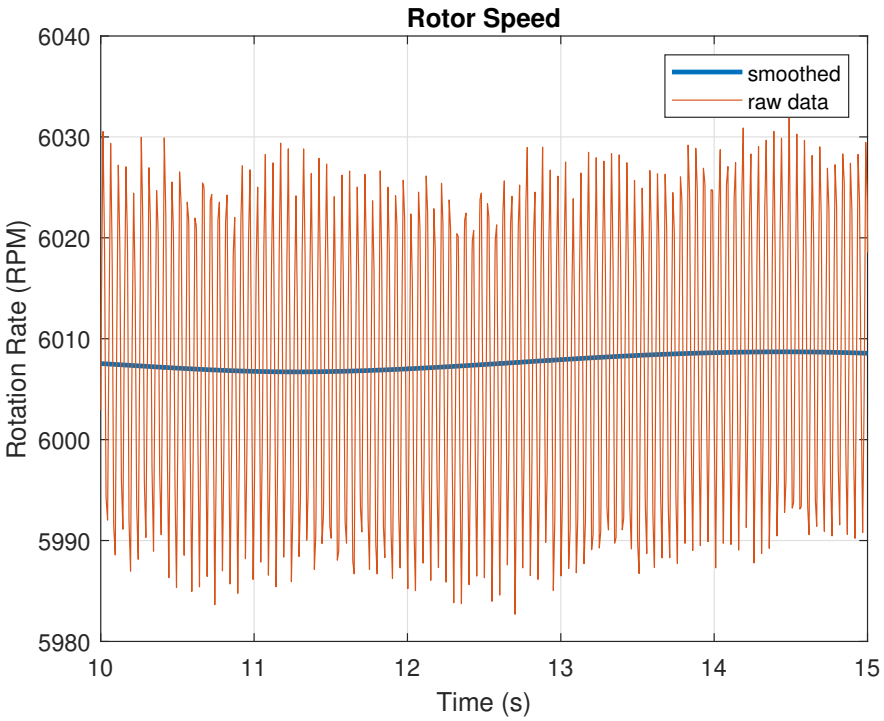


Figure 5.9: Comparison of the raw and smoothed rotation rate.

The acoustic pressure responses were measured and collected in the time domain and converted to the frequency domain using the Fast Fourier Transform. A Hanning window was applied to the data with 50% overlap. The electret microphones were favored over the Kulite transducer due to the electrets' comparatively low noise floor, which can be seen in Figure 5.10. A trandsucer cannot measure pressure fluctuations with amplitudes lower than its noise floor. The Kulite transducer, however, has a higher dynamic range than the electret microphones. Therefore, the two transducers were placed side-by-side below the rotor and the measured responses were compared. Figure 5.11 shows that the tonal levels measured by the Kulite and electret are similar, indicating that the sound pressure produced by the rotor did not exceed the electrets' linear capabilities. The electrets were subsequently deemed adequate sensors for this test.

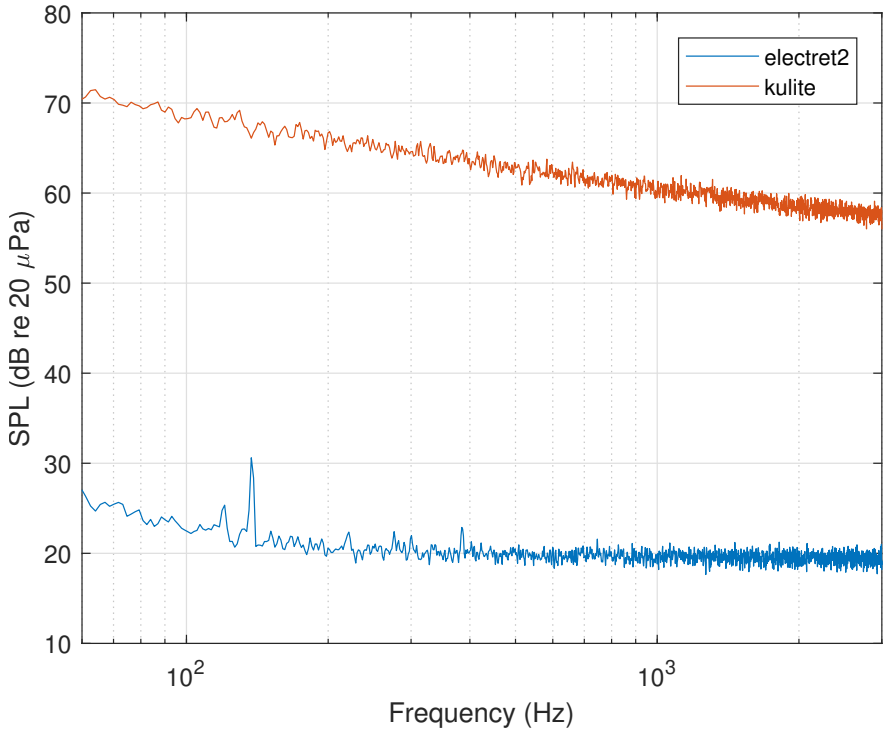


Figure 5.10: Background SPL comparison of the Kulite transducer and electret.

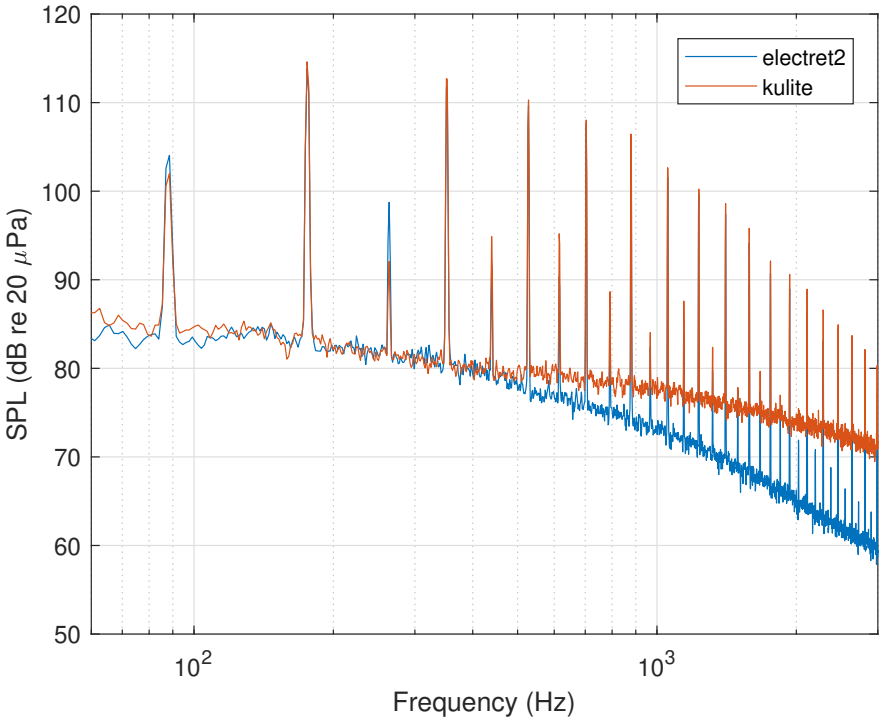


Figure 5.11: Comparison of Kulite pressure response with the response measured at Electret 2.

The coherence between the tachometer and the near-field and far-field sensors was calculated to quantify the linear relationship between the signals. Feedforward control requires an available reference signal, which is determined by the linear relationship between the reference signal and the sensor at the targeted location of reduction. The reference signal in this study is provided by the tachometer, and the far-field microphones were the locations of attenuation. Additionally, in order to establish an accurate observation filter, the near-field electret and far-field microphone signals must be highly correlated. Signals that are highly correlated have a coherence close to 1 and signals that are uncorrelated have a coherence close to 0. The ratio of auto and cross-spectral densities is used to calculate coherence

$$\gamma_{xy}^2 = \frac{|S_{xy}|^2}{S_{xx}S_{yy}} \tag{5.10}$$

where the $x$ denotes the reference signal and $y$ denotes the response at the targeted location of attenuation. The amount of attenuation at the desired location is dependent on the coherence between the reference signal and the sensor at the location of reduction [41]. The maximum attenuation $\Delta$ in dB can be calculated as

$$\Delta = -10log_{10}(1 - \gamma_{xy}^2) \tag{5.11}$$

By this equation, signals that are 0.9 coherent can be attenuated by a maximum of 10 dB using SISO feedforward control, assuming that the error response is stationary and the controller is both realizable and time invariant. The coherence between the tachometer and far-field microphone when the rotor is operating at 5250 RPM is shown in Figure 5.12. The coherence is greater than 0.9 at the shaft rotation rate, 87.5 Hz, and the BPF, 175 Hz, as well as several harmonics. Therefore, attenuation greater than 10 dB may be possible to an appropriately designed feedforward control system. Figure 5.13 shows the coherence between the tachometer signal and the near-field sensor, electret 2. Similar to Figure 5.12, coherence is above 0.9 at the BPF and harmonics. Ideally, the coherence would be 0.99 at the rotor BPF and harmonics. This discrepancy could be due to flow recirculation effects. Flow recirculation is not as apparent in the rotor plane, where M1 is positioned [6]. Figure 5.14 shows the coherence between the reference tachometer and M1. Coherence is nearly 0.98 at the shaft harmonic, rotor BPF, and several lower harmonics. Coherence is also higher at higher harmonics than in Figure 5.12, indicating that flow recirculation might have an effect on coherence.

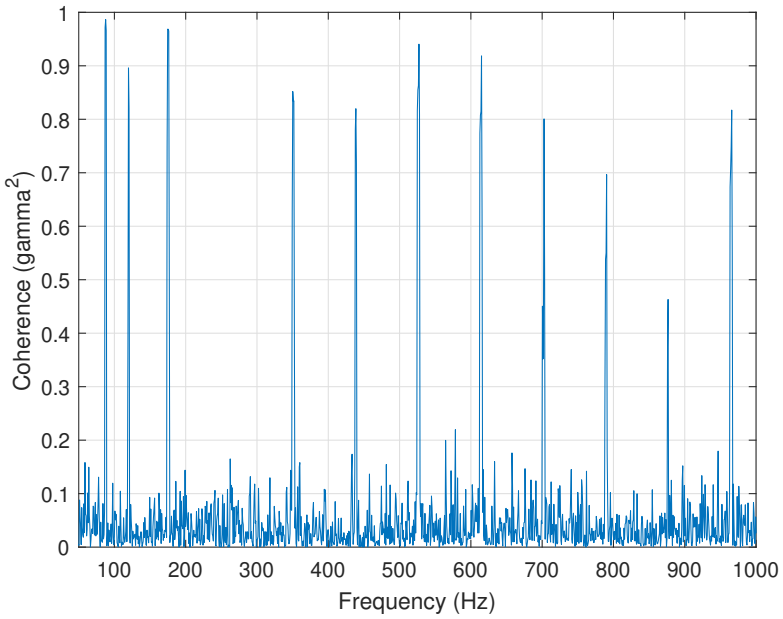


Figure 5.12: Coherence between the error microphone (M3) and the tachometer signal.

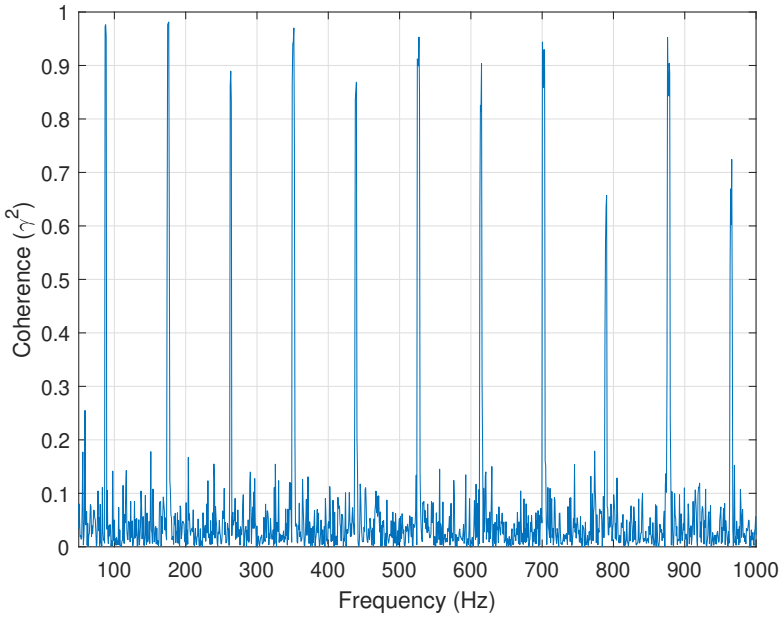


Figure 5.13: Coherence between Electret 2 and the tachometer signal when the BPF is 5250 RPM.

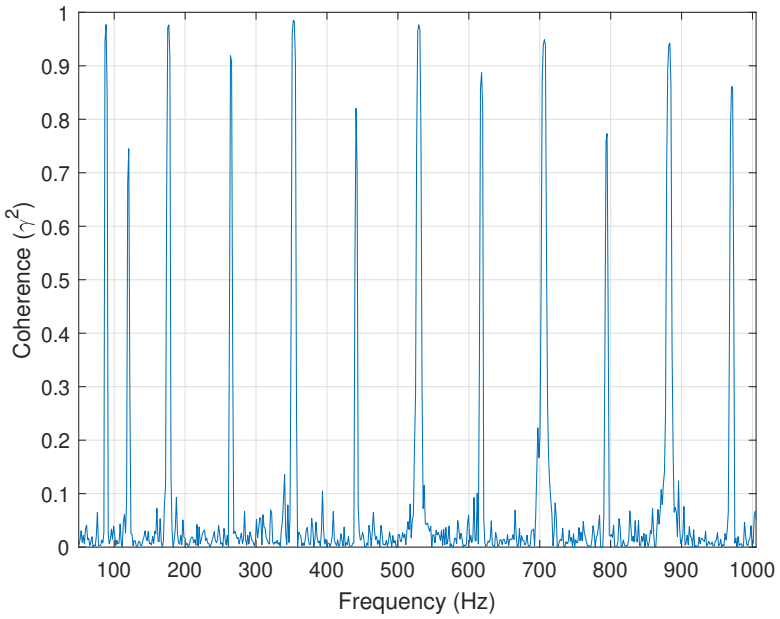


Figure 5.14: Coherence between the error microphone (M1) and the tachometer signal.

## 5.5 System Identification Results

The measured paths between the control speaker to electret 2 and M3 in the far-field were estimated using Welch's averaged periodogram [52], which converts time domain data to the frequency domain by separating the time series into segments, calculating the periodogram for each segment, and averaging. Figures 5.15 and 5.16 show the comparison between the measured and modeled magnitude and phase between the speaker and the far-field microphone and the near-field electret, respectively. Coherence is high, nearly 0.99, between the speaker and the far-field microphone from 50 to 1200 Hz, the frequency range at which the speaker played white noise. This high level of coherence confirms that the speaker shares a linear relationship with the far-field microphone. Coherence between the speaker and the near-field electret is also largely greater than 0.9 across the frequency range 50-1200 Hz, although coherence drops off at a number of frequencies within this

range. The roll off in coherence and subsequent poor match between the measured and modeled transfer functions is due to the physical frequency range over which the speaker would play broadband noise. Figure 5.16 shows that at certain frequencies within the range, the coherence between the speaker and the electret drops. These dropouts in coherence between the loudspeaker and the electret occur at the same locations during both rotation rates, indicating that these dropouts could be due to scattering effects that are introduced by the addition of the conical airframe. This was noted while observing results at these frequencies.

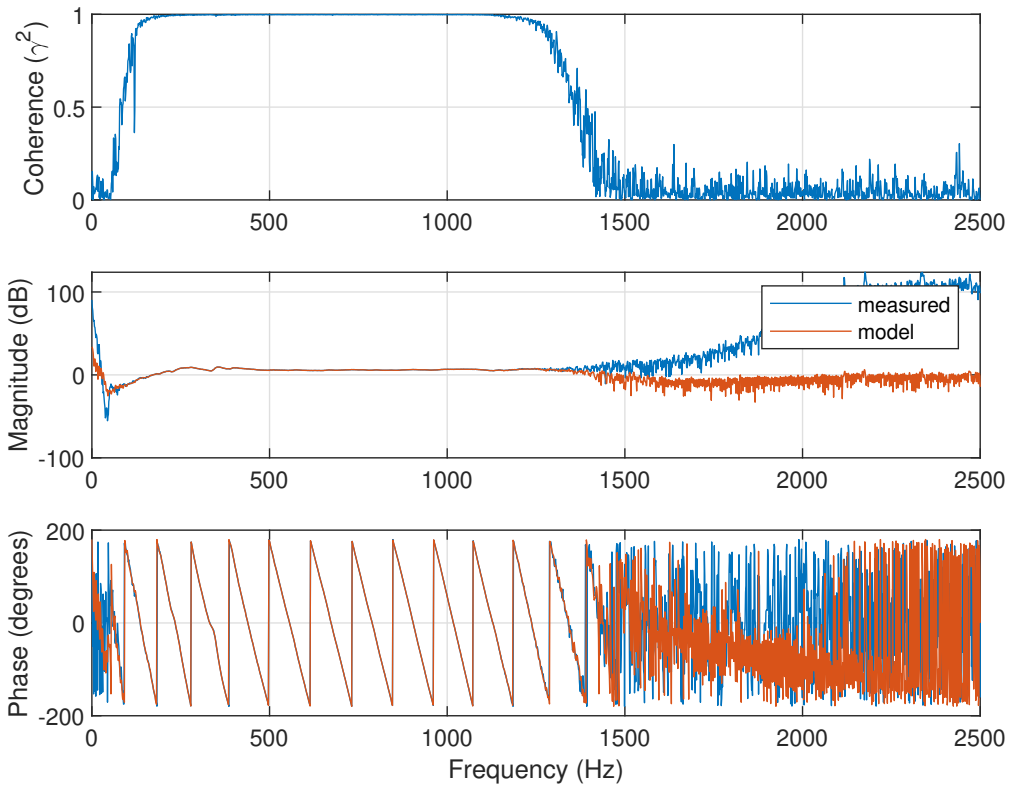


Figure 5.15: System identification between the control speaker and the virtual location, M3.

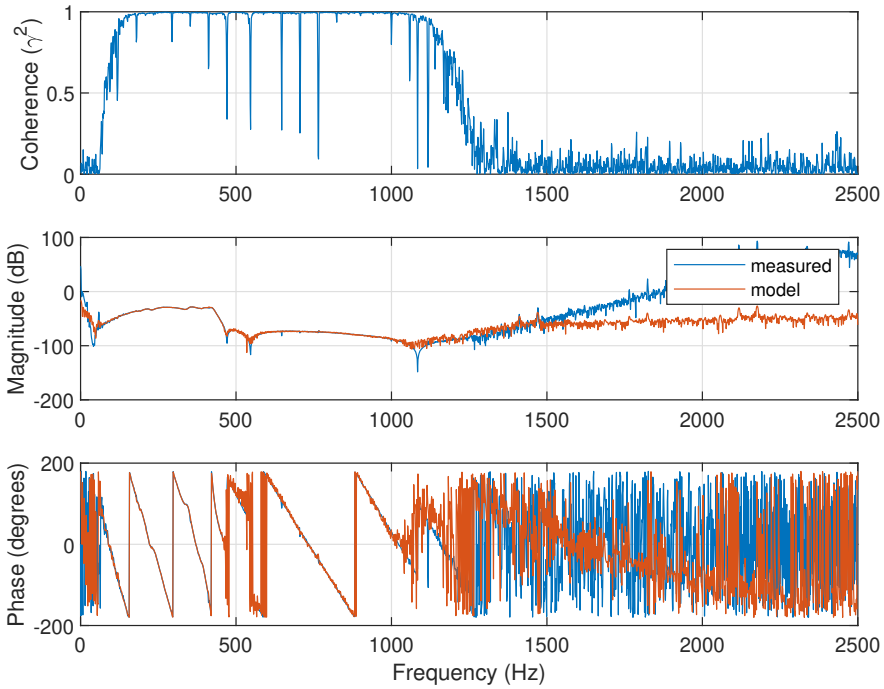


Figure 5.16: System identification between the control speaker and the physical sensor, electret 2.

The quality of the paths $\hat{G}_{pu}$ and $\hat{G}_{vu}$ were quantified using the variance-accounted-for (VAF) method. The VAF uses the equation

$$VAF = (\frac{var(y_i - \hat{y}_i)}{var(y_i)}) * 100\% \tag{5.12}$$

to calculate the similarity between the modeled path and the measured path, where $y_i$ is the measured response and $\hat{y}_i$ is the response estimated using the speaker signal and the plant model. A value close to 100 indicates that the two paths are highly similar in dynamics. The VAF between the paths $\hat{G}_{pu}$ and $\hat{G}_{vu}$ are shown in Table 5.1. Using M3 to establish the path $\hat{G}_{vu}$ establishes a plant model with a high VAF, above 98, indicating that the path successfully models the relationship between the control input and the virtual location. Additionally, the VAF estimations between the electrets and the control input are above 94, also indicating that each electret can accurately estimate the path $\hat{G}_{pu}$. The lower VAF value could be a result of the dropouts in coherence demon-

strated in Figure 5.16.

Table 5.1: VAF for Estimated Plants

| Plant | M3 | Elec1 | Elec2 | Elec3 |
|---|---|---|---|---|
| $\hat{G}_{pu}$ | 99.22 | 94.10 | 96.57 | 95.82 |
| $\hat{G}_{vu}$ | N/A | 98.43 | 99.43 | 99.20 |

### 5.5.1 Observation Filter

The observation filter (OF) describes the path from the near-field electret to the far-field microphone which is temporarily placed at the virtual location while the rotor is operating. The objective in identifying an OF is to accurately estimate the magnitude and phase characteristics where coherence between the near-field electret and far-field microphone is high, above 0.8. Figure 5.17a shows that the coherence is high at the shaft rotation rate, 87.5 Hz, and the BPF, 175 Hz, as well as several harmonics, suggesting that the OF will only be capable of accurately estimating these tones. Figure 5.17a compares the magnitude and phase of the measured and estimated OF when the rotor was operating at 5250 RPM. Locations where coherence is high generally match within 1 dB and 10°, indicating that the virtual sensor will sufficiently estimate the SPL at these tones.

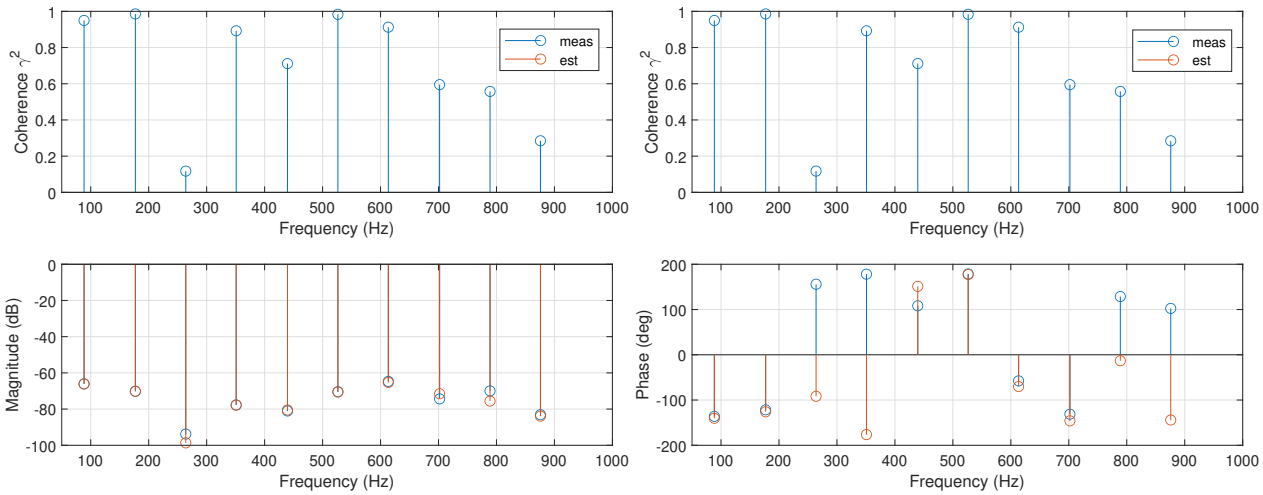


(a) (b)

Figure 5.17: Measured and estimated (a) magnitude and (b) phase of the OF at 5250 RPM between the near-field electret 2 and the far-field microphone M3. The coherence between electret 2 and M3 is shown above.

The estimated and measured magnitude and phase values of the OF between electret 2 and M3 while the rotor is rotating at 6000 RPM are shown in Figure 5.18. Similar to the 5250 RPM case, the coherence between the near-field and far-field microphones is high, above 0.8, at the shaft rotation rate and BPF, 100 Hz and 200 Hz, respectively, and several harmonics. Figures 5.18a and 5.18b show that the estimated magnitude and phase values match within 1 dB and 10°at tones where coherence is above 0.8. Frequencies where the coherence is low, below 0.6, are poorly matched, indicating that the virtual sensor cannot accurately estimate these tones.

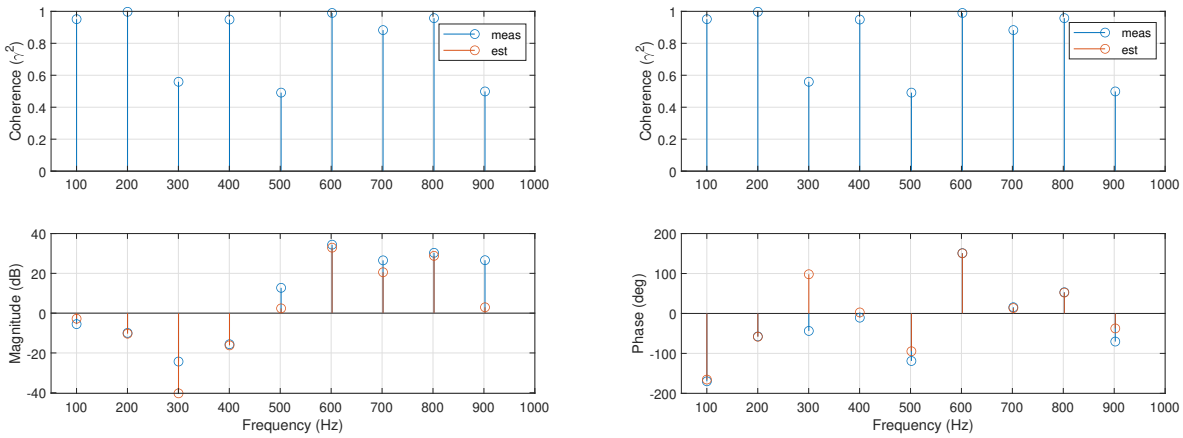


(a) (b)

Figure 5.18: Measured and estimated (a) magnitude and (b) phase of the OF at 6000 RPM between the near-field electret 2 and the far-field microphone M3. The coherence between electret 2 and M3 is shown above.

The VAF was not an appropriate method to quantify the quality of the OF. Unlike the paths $\hat{G}_{pu}$ and $\hat{G}_{vu}$, which were estimated using broadband noise from the speaker, the OF modeled the tonal noise produced by the rotor. Figures 7 and 8 show the comparison of the modeled and measured OF paths at the BPF and harmonics, along with the measured coherence at these frequencies. As the rotor noise is tonal, the only frequencies at which the OF model must match the measured OF in order to be deemed appropriate are the BPF and the harmonics. The coherence is high at the frequencies of interest, indicating that it is possible to create an accurate model at these locations. The mean-squared-error (MSE) was calculated using the equation

$$MSE = \frac{1}{n}\sum_{i=1}^{n}(y_i - \hat{y}_i) \tag{5.13}$$

where $n$ is the number of samples, $\hat{y}_i$ is the measured disturbance pressure measured by the microphone in the far-field, and yhati is the estimated far-field pressure, given by the model OF. The variables $\hat{y}$ and $\hat{y}_i$ represented the pressures at the frequencies of interest, the BPF, harmonics, so

that the MSE was only based on these frequencies. The MSE between the modeled and measured response at these frequencies is shown in Table 5.2. A small MSE value indicates a good match between the measured and modeled OF. Overall, the electrets' MSE during 5250 RPM is considerably less than the MSE during 6000 RPM. Comparatively, electret 2 creates the OF model with the least amount of error.

Table 5.2: MSE between the measured far-field pressure and the modeled far-field pressure using the OF created with each electret.

| MSE | | | |
|---|---|---|---|
| RPM | Elec1 | Elec2 | Elec3 |
| 6000 | 1.53 | 7.096 | 3.054 |
| 5250 | 44.84 | 11.16 | 53.84 |

## 5.6 Discussion

This chapter detailed the setup and outlined the methods that were used in experimental testing. The hardware used to perform ANC is explained. Additionally, the control system used to perform ANC with a physical sensor is discussed as well as the system used to perform ANC using a virtual sensor. The frequency spectrum measured by the Kulite transducer and the electret microphone verified that the rotor noise did not exceed the electret microphones' capabilities. Additionally, the electrets were advantageous due to their low noise floor. The coherence between the tachometer the far-field microphones and the near-field electrets showed that the coherence was high at the BPF and harmonics. The system identification was performed between the far-field microphone and control loudspeaker, as well as the near-field microphone and the control loudspeaker. The VAF is high, between 94% and 99%, indicating that the paths estimated during the system identification can sufficiently model the measured paths. Additionally, the system identification was performed

to estimate the OF, which models the path from the near-field electret to the temporarily placed far-field microphone location. The high coherence between the near-field electret and the virtual location at the BPF and harmonics suggests that the virtual sensor can accurately estimate the SPL at the corresponding tones. The MSE between each electret and the far-field microphone is lowest at electret 2, indicating that electret 2 will achieve the OF model that best matches the measured path, and subsequently establish the virtual sensor that most accurately estimates the response at the virtual location.

# Chapter 6

# Virtual Error Sensor Results

This chapter investigates how effectively a virtual error sensor (VES) system can operate. A VES was established using the remote microphone technique (RMT) with the intent of using it in conjunction with an ANC system. In order to apply ANC to a location using the RMT, an accurate estimate of the response at the virtual location must be established. After performing a system ID to establish an OF between the near-field electrets and a far-field microphone, the far-field SPL was estimated using the OF. The coherence between the reference tachometer and estimated far-field response is also observed. Frequencies where coherence is low indicates that an accurate estimate might not be established. Additionally, the numerical model used different noise sources to predict OFs between the near-field and far-field. An accurate numerically predicted OF could be advantageous in having to obtain measured data to calculate the OF.

## 6.1 Virtual Sensors using Measured Observation Filters

As previously discussed in Chapter 5.3.1, the virtual error sensors were established through estimating the OF. Open-loop data was collected for 10 seconds while the rotor operated at 5250 RPM

and 6000 RPM. The responses at the near-field electrets and far-field microphones were measured and used to estimate the OF. The near-field and far-field data was separated into halves in terms of the time record. The set of first 5 seconds was referred to as the "model data" and the second half was called the "validation data." The OF was an FIR filter of length 1024 filter coefficients that was estimated using the model data. Then, the OF and the validation data calculated an estimate of the far-field response, which was compared to the measured far-field response at the same location.

The coherence between the reference signal and the estimated error signal was estimated to quantify their linear relationship. Frequencies with high coherence, above 0.8, indicate that it is possible to pass the signal from the reference tachometer through a linear system to estimate a far-field response. These frequencies of interest include the shaft rotation rate and rotor BPF, and their harmonics, where most of the content in the frequency spectrum is contained. Coherence between the reference signal and the estimated far-field signal is not always high at these frequencies. Harmonics of the shaft rotation rate that have low coherence indicate that the far-field response might not be accurately estimated using a reference tachometer signal and a linear system. An inaccurate estimate of the far-field response indicates that the ANC system will not effectively attenuate the SPL at such frequency. Additionally, an inaccurate virtual sensor at certain frequencies could possibly lead to amplification at the corresponding frequencies when the ANC system is on.

Figure 6.1 shows the comparison of the measured and estimated SPL at M3 using electret 1 while the rotor is operating at 5250 RPM. The measured SPL was calculated using the validation data collected during system identification. The estimated SPL at the virtual location is determined using the measured near-field response in the validation data set and the OF. The estimated SPL at M3 at the shaft rotation rate, 87.5 Hz, and the BPF, 175 Hz, matches the measured SPL within 3 dB. The coherence between the reference signal, provided by the tachometer, and the estimated far-field response is shown below. The coherence is about 0.9 at the shaft harmonic and BPF, as well as several harmonics. Additionally, the estimated SPL also matches the measured SPL

within 3 dB at the harmonic tones 350, 437.5, 525, 700, and 787.5 Hz. The coherence between the tachometer and the far-field response estimate is also above 0.8. The SPL at tones where coherence is low, for example at 262.5 Hz, are not accurately estimated. Figure 6.2 shows the estimated and measured SPL using electret 2 to establish the virtual sensor. Again, estimated far-field SPL at the shaft rotation rate frequency and BPF match the measured SPL at these tones. Coherence at these tones is above 0.9. Locations where coherence is above 0.8 are accurately estimated. Similar trends are shown in Figure 6.3, where electret 3 is used to establish the virtual error sensor.

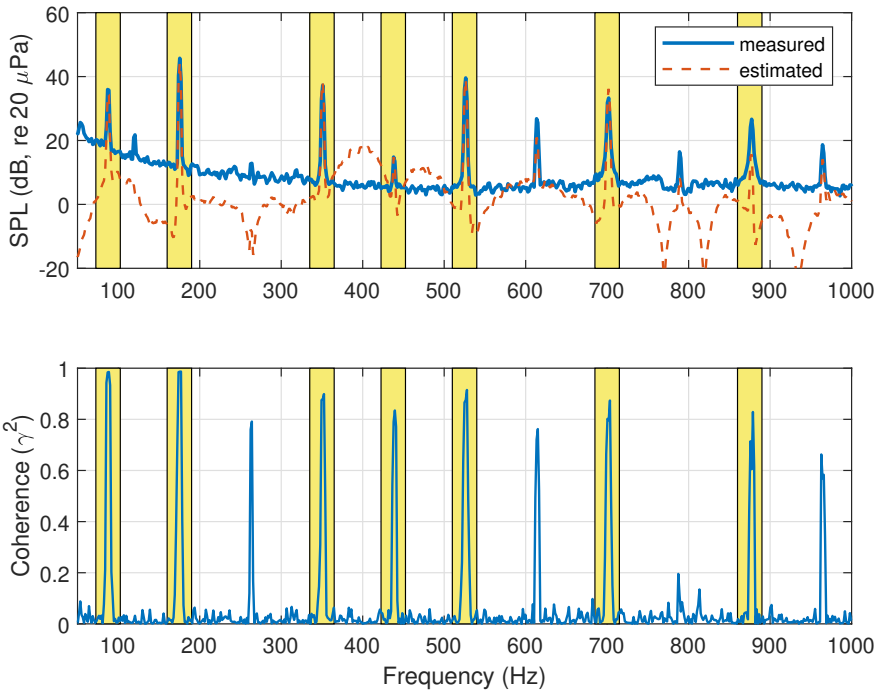


Figure 6.1: Measured and estimated SPL at M3 while the rotor is operating at 5250 RPM using electret 1.

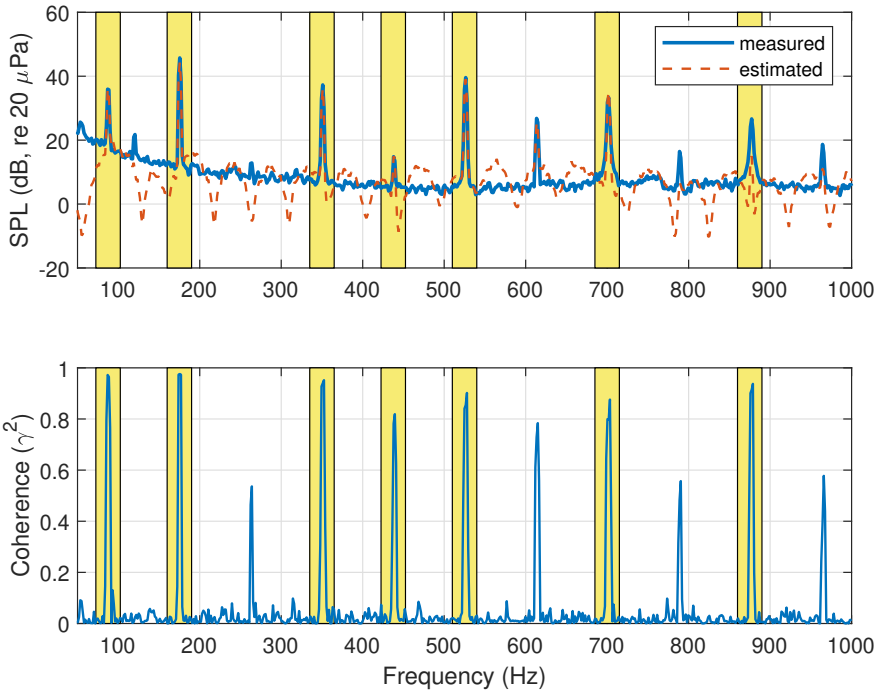


Figure 6.2: Measured and estimated SPL at M3 while the rotor is operating at 5250 RPM using electret 2.

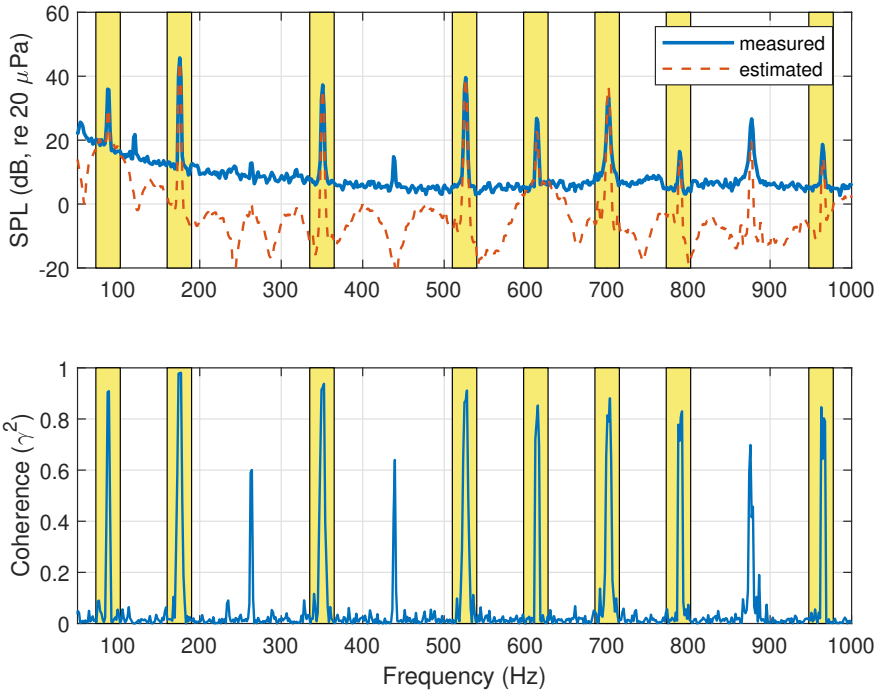


Figure 6.3: Measured and estimated SPL at M3 while the rotor is operating at 5250 RPM using electret 3.

The measured and estimated SPL during the rotor rotation rate 6000 RPM is also compared and the same general trends were observed as when the rotor rotation rate was 5250 RPM. Again, the data used to construct the OF at 6000 RPM was separated into two halves based on the time records. The OF was established using the first half of the time record. The far-field SPL was estimated using the OF and the near-field response from the validation data. The measured far-field SPL was calculated using the near-field and far-field pressure responses from the validation data. Figure 6.4 shows the measured and estimated SPL at M3 using electret 1 to establish the OF. The coherence between the reference signal and the estimated far-field response at M3 is also shown in Figure 6.4. Coherence is above 0.8 at the BPF, 200 Hz, and harmonics through 800 Hz. The virtual sensor is successful in estimating the SPL at M1 at the BPF and several harmonics. However, the virtual sensor does not estimate the SPL at the shaft rotation rate, 100 Hz, and several harmonics, 300 Hz

and 500 Hz. This poor estimate could be a result of low coherene between the near-field electret and the far-field microphone. The measured and estimated SPL using electret 2 to establish the virtual sensor are compared in Figure 6.5. The measured and estimated SPL at M3 using electret 3 to establish the virtual sensor are shown in Figure 6.6. The coherence between the reference signal and the estimated far-field response at M3 is also shown in Figures Figure 6.5 and 6.6. Again, an accurate virtual sensor is generally established at harmonics where coherence is 0.8 or greater. However, there are several harmonics where, although the coherence is high, the virtual sensor does not accurately estimate the SPL. For example, 6.4 shows that although the coherence between the reference signal and the error estimate is high at 500 Hz, the virtual sensor does not estimate the SPL at M3 within 3 dB of the measured SPL. Similarly, Figures 6.5 and 6.6 show the same inaccuracy at 500 Hz, despite the high coherence at the same tone.

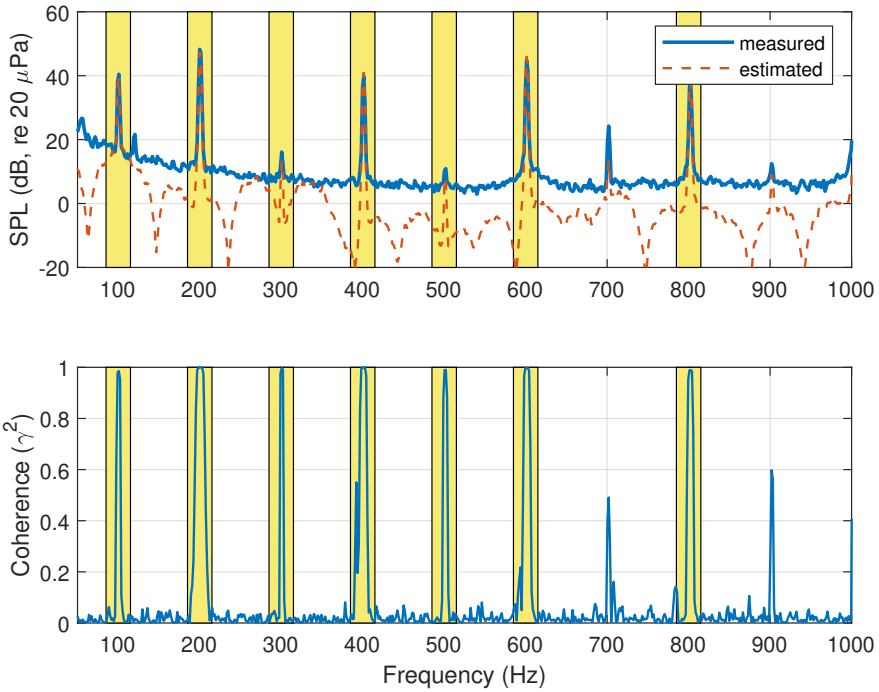


Figure 6.4: Measured and estimated SPL at M3 while the rotor is operating at 6000 RPM using electret 1.

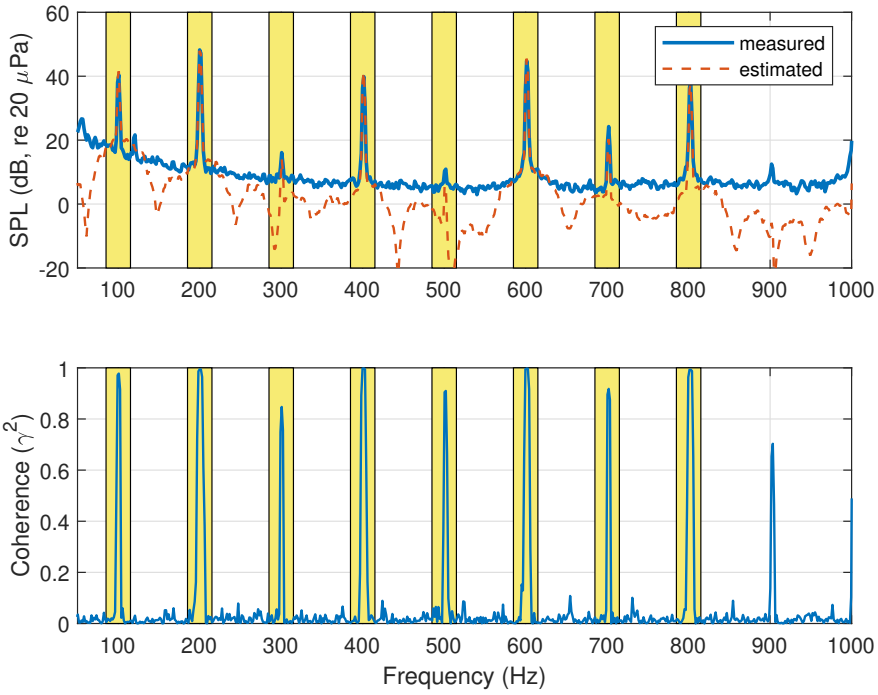


Figure 6.5: Measured and estimated SPL at M3 while the rotor is operating at 6000 RPM using electret 2.

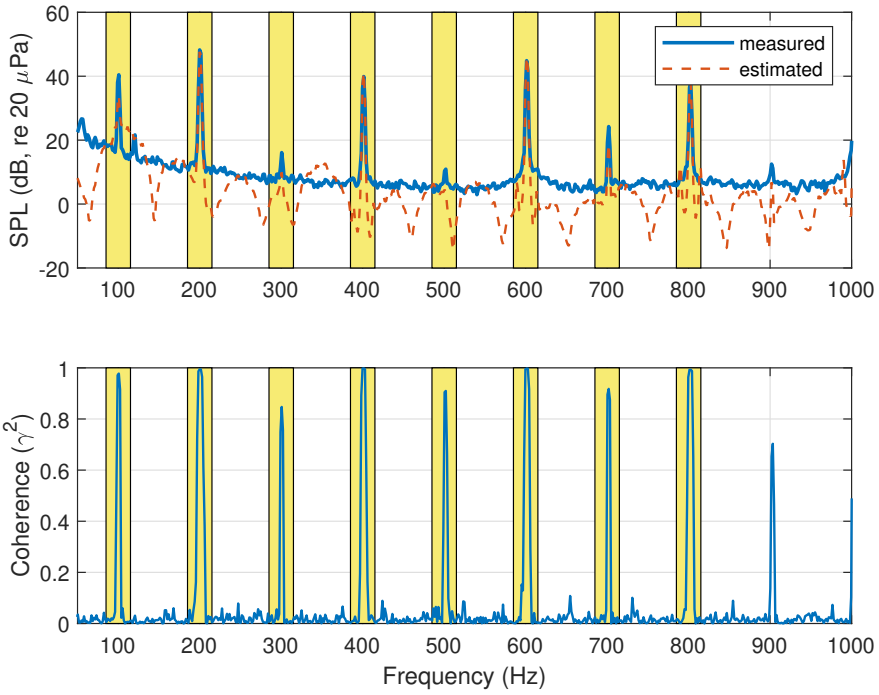


Figure 6.6: Measured and estimated SPL at M3 while the rotor is operating at 6000 RPM using electret 3.

As previously mentioned, electret 2 establishes a virtual sensor with the least MSE. Therefore, electret 2 was the used to establish the virtual sensor at the remaining observer locations M1 and M5. Figure 6.7 shows the comparison of the measured and estimated far-field SPL at M1 during the rotation rates 5250 and 6000 RPM at the observer microphones M1. Figure 6.8 shows the coherence between the reference tachometer and the far-field estimate at the virtual location, M5, that is established using electret 2. The measured and estimated SPL are also compared. Figure 6.8a shows the virtual error estimate when the rotor is operating at 5250 RPM. Figure 6.8b shows the coherence and the measured and estimated SPL at M5 while the rotor is operating at 6000 RPM.

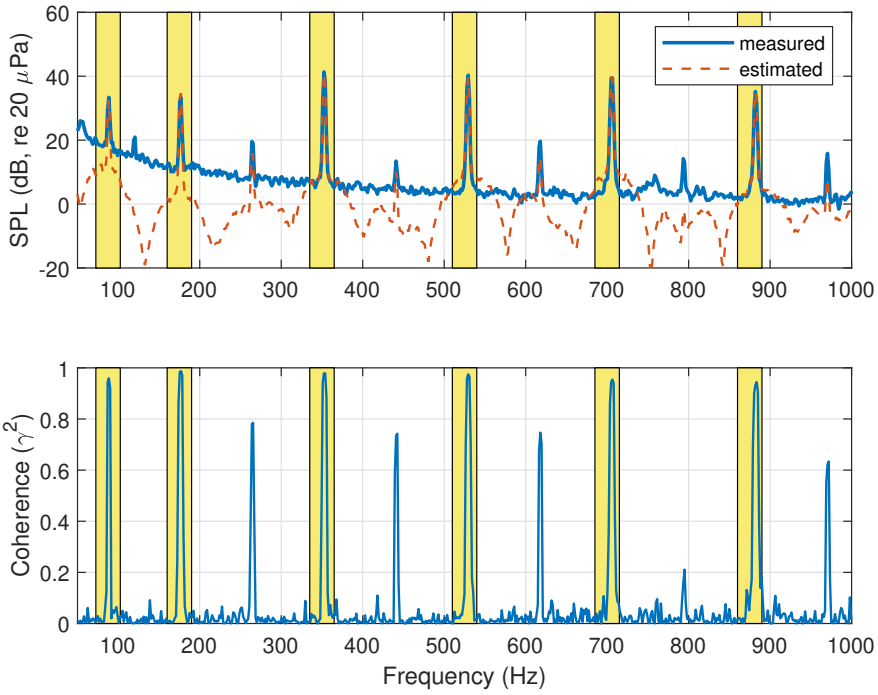


(a)

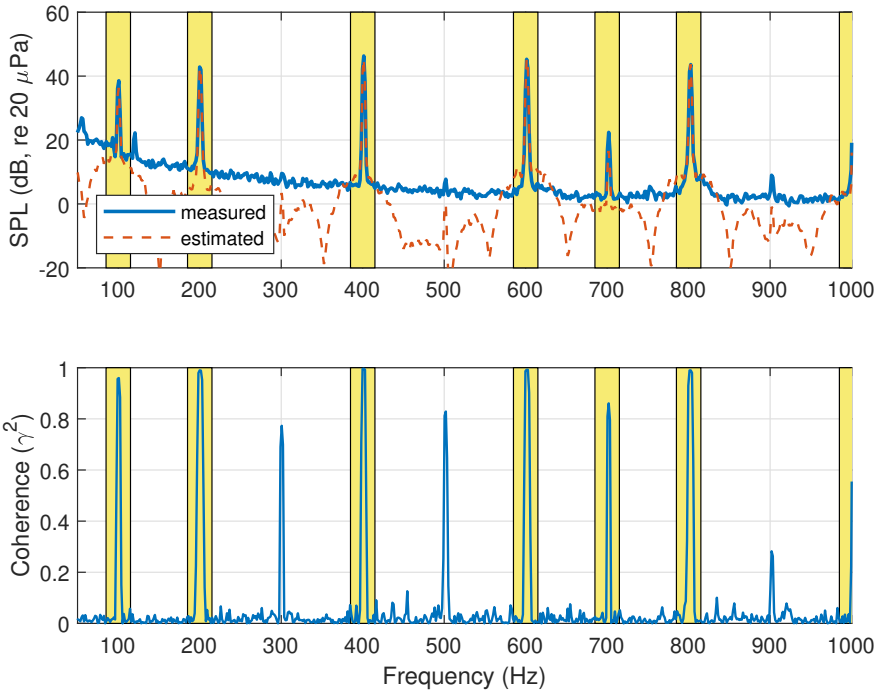


(b)

Figure 6.7: Measured and estimated SPL at M1 using electret 2 while the rotor is operating at (a) 5250 RPM and (b) 6000 RPM.

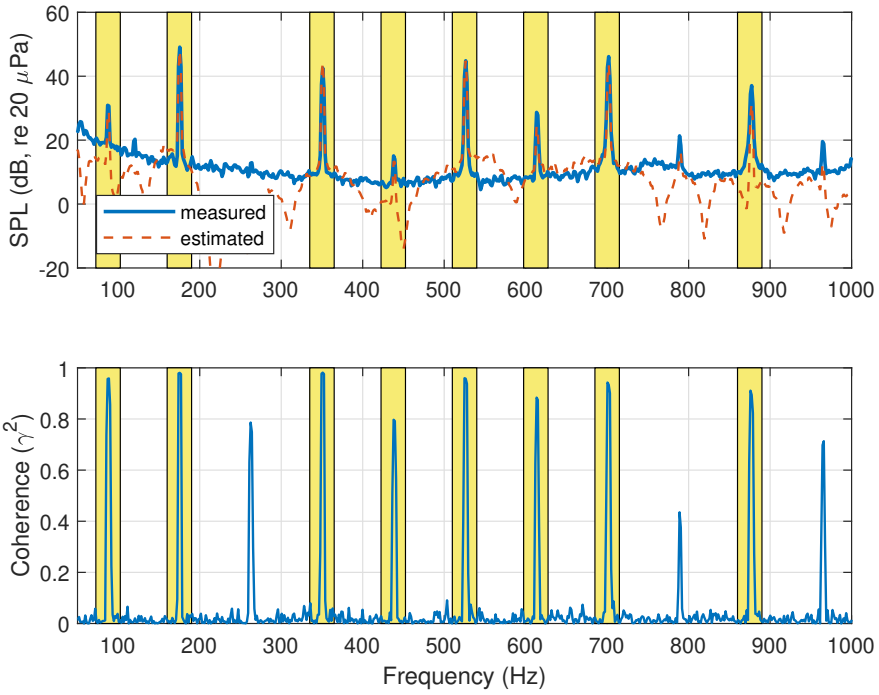


(a)

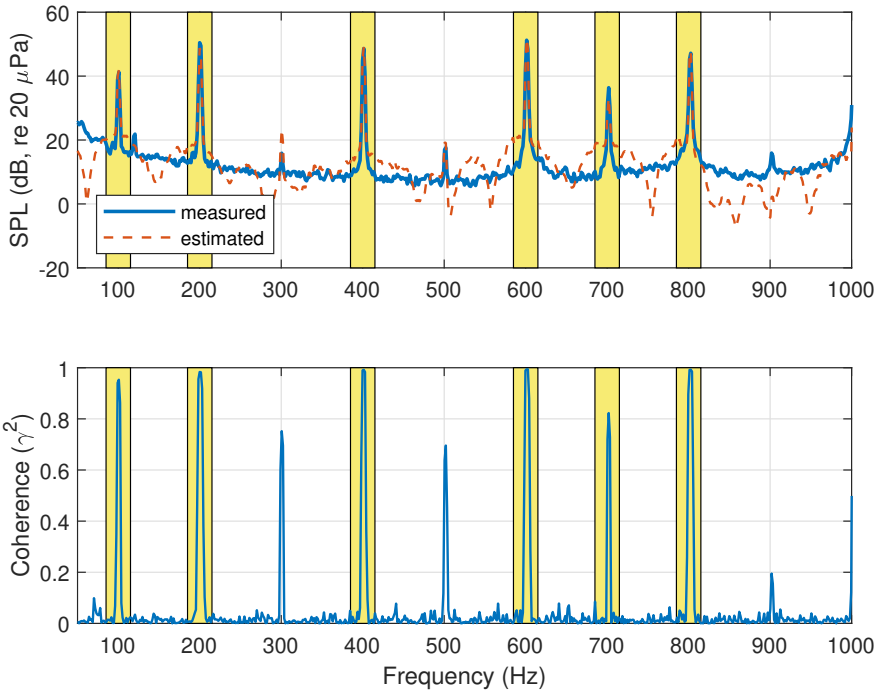


(b)

Figure 6.8: Measured and estimated SPL at M5 using electret 2 while the rotor is operating at (a) 5250 RPM and (b) 6000 RPM.

## 6.2 Virtual Sensors with Numerical Modeling

The most appropriate source model was identified through comparing the near-field and far-field pressure that different types of sources produced. Establishing a source model that accurately captures the characteristics of the rotor is helpful in estimating the potential SPL reduction that could be achieved at far-field locations when the VES is used to provide the ANC system with the far-field pressure estimate. Microphones in the near-field and far-field were used to estimate the complex pressure when a monopole, dipole, and plane wave were used to represent the disturbance noise caused by the rotor. The microphones were placed in locations that corresponded to the far-field microphone array and the near-field electrets used during experimental testing, which are specified in Chapter 5.

### 6.2.1 Observation Filter

The accuracy of the source was determined by using the near-field and far-field complex pressure values to estimate the observation filter (OF), which is required in order to estimate the virtual location's response using the RMT. Under the assumption that a linear relationship between the physical microphones and the location of the virtual microphones exists, the equation

$$d_v(e^{j\omega t}) = OF(e^{j\omega t})d_p(e^{j\omega t}) \tag{6.1}$$

characterizes the path between the physical and virtual microphone locations, $d_p$ and $d_v$ respectively. In equation 6.1, $OF$ is a complex value that represents the relationship between the near-field and the far-field at a discrete frequency. The subscript $p$ denotes the near-field sensor, where a physical sensor will be located in experimental testing. The subscript $v$ represents the virtual location that will be attenuated. In order to identify the OF, a sensor is temporarily placed at the

virtual location.

Elliott and Cheer [51] derived that the optimal OF can be calculated through the power spectral density of the physical sensors and the cross spectral density of the physical sensors and the virtual location. In a multiple-input-multiple-output (MIMO) system, where **x** and **d** are vectors containing the complex pressures caused by the primary disturbance at the near and far-field locations, the power-spectral density $\mathbf{S}_{xx}$

$$\mathbf{S}_{xx}(e^{j\omega t}) = E[\mathbf{x}(e^{j\omega t})\mathbf{x}^H(e^{j\omega t})] \tag{6.2}$$

quantifies the spectral content in each frequency bin. Additionally, the cross-spectral density

$$\mathbf{S}_{dx}(e^{j\omega t}) = E[\mathbf{d}(e^{j\omega t})\mathbf{x}^H(e^{j\omega t})] \tag{6.3}$$

describes the cross-correlation between the near and far-field sensors at each frequency bin.

$$\mathbf{OF}(e^{j\omega t}) = [\mathbf{S}_{dx}(e^{j\omega t})\mathbf{S}_{xx}^{-1}(e^{j\omega t})] \tag{6.4}$$

The power spectral density is $\mathbf{S}_{xx}$ and the cross spectral density is $\mathbf{S}_{dx}$.

The far-field acoustic pressure responses at the rotor BPF were evaluated; at this frequency, the theoretical zone of quiet would be largest and attenuating the SPL would be most effective in practical applications. The OF for each source type was estimated at 175 Hz and 200 Hz, the BPFs corresponding to the the two rotor rotation rates that were measured during experimental testing (5250 RPM and 6000 RPM). The experimental near-field data and the numerically predicted observation filter estimated the far-field acoustic pressure response, which was then compared to experimental far-field acoustic pressure.

### 6.2.2 Noise Sources

Several different OFs were established using the numerically predicted near-field and far-field acoustic pressure responses from several different source types. First, the noise source was modeled as a monopole with unity amplitude, and the near-field and far-field data were predicted. The OF was estimated using the numerically predicted near and far-field complex pressures. The second noise source was modeled using a dipole as two monopoles of equal amplitude and opposite phases. The OF at each of the observer locations was numerically estimated again. The third OF was determined using a dipole to represent the noise source and conical boom to represent the airframe, which provided reflection pressure to the model. The representative airframe shared the same dimensions as the 3D printed boom cone used during experimental testing, with minor and major diameters 20 mm and 70 mm and length 163 mm.

The final OF was constructed using rotating plane wave to model the rotor noise source. The plane wave radiation condition creates a similar directivity pattern to a 2-bladed propeller, which is very similar to a rotating dipole. The noise source was defined as incident pressure, as opposed to total pressure; incident pressure implies that the numerically predicted pressure response is only a result of the source, whereas total pressure includes the sum of incident pressure and reflected pressure, provided by the boom cone. The noise produced by a rotating ring source has been studied by Prentice [50] and Chapman [49], who closely examined the pressure field produced by both thickness and loading noise of a rotating propeller. Schiller [10] demonstrated that a 2-bladed rotor's rotating characteristics could be modeled using a thickness noise component only. The steady thickness noise displacement of a rotating ring, $h$, is defined by the equation,

$$h = Se^{-imB\theta} \tag{6.5}$$

where $\theta$ is the rotation angle of the propeller, and $m$ is the harmonic number, and $B$ is the number

of blades. $S_m$ is a constant source term.

### 6.2.3 Results

Tables 6.1 and 6.2 show the predicted far-field pressure SPL at M1, M3, and M5 using the measured near-field data and the numerically predicted OFs, which were specific to the noise source. These far-field SPL estimates were compared to the measured far-field SPLs. The OF predicted using a monopole noise source created the least accurate estimate of the far-field pressure. The dipole more closely resembled the 2-bladed UAS rotor that this study focused on, where the two rotor blades have equal amplitude and opposite phases. Although the dipole source resembled a 2-bladed rotor more closely than the monopole source, the directivity characteristics of a rotating propeller were not captured, and the estimated far-field pressure does not closely resemble the measured far-field pressure. When the representative conical airframe is included in the model configuration, the near-field SPL is amplified by 5 dB, while the SPL of far-field observer locations largely remained the same. This prediction does not agree with the experimental far-field acoustic pressure data, which demonstrated amplification at the far-field microphone locations by about 6 dB at the BPF and the second harmonic when the cone was included in the test setup. This discrepancy could be a result of interaction effects that are introduced by the addition of the airframe during experimental testing.

The far-field SPL that was estimated using the measured near-field data and the rotating plane wave OF is much closer to the measured far-field SPL, indicating that the quality of the observation filter is source dependent. For example, if the source is modeled as a monopole rather than a plane wave, the observation filter will be drastically changed and the far-field estimate will not accurately model the rotor characteristics. Additionally, an inaccurate rotor noise source model will ultimately lead to an incorrect loudspeaker control input.

Table 6.1: Comparison of the estimated far-field SPL at 175 Hz using the predicted OFs that were established using electret 2, and the measured far-field SPL.

| | SPL (dB) | | | | |
|---|---|---|---|---|---|
| Location | Monopole | Dipole | Dipole with Airframe | Plane Wave | Measured |
| M1 | 90 | 80 | 77 | 56 | 33 |
| M3 | 90 | 79 | 76 | 54 | 43 |
| M5 | 90 | 77 | 74 | 48 | 46 |

Table 6.2: Comparison of the estimated far-field SPL at 200 Hz using the predicted OFs that were established using electret 2, and the measured far-field SPL.

| | SPL (dB) | | | | |
|---|---|---|---|---|---|
| Location | Monopole | Dipole | Dipole with Airframe | Plane Wave | Measured |
| M1 | 91 | 82 | 79 | 59 | 42 |
| M3 | 91 | 82 | 78 | 57 | 47 |
| M5 | 91 | 79 | 76 | 51 | 48 |

## 6.3 Discussion

The virtual sensors that were established using experimentally determined transfer functions estimate the SPL at the virtual location within 3 dB of the measured SPL at frequencies where coherence between the reference signal and the far-field estimate is high, above 0.8. Frequencies where coherence is highest correspond to the rotor BPF and harmonics. Conversely, the virtual sensors do not accurately estimate the harmonics where coherence is low. This suggests that if a

reference signal and estimated far-field signal share high coherence at certain frequencies, it is possible to establish an accurate virtual error sensor at the corresponding frequencies. The numerical model was used to generate a predicted OF at the rotor BPFs (175 Hz and 200 Hz), using different types of sources to represent the rotor noise source. The rotor noise source was represented using a monopole, dipole, and plane wave ring source. Experimentally measured near-field acoustic pressure measurements were then passed through the numerically predicted OF to estimate the far-field acoustic pressure response. The estimated far-field acoustic pressure response was then compared to the experimentally measured far-field acoustic pressure response. Generating an accurate numerically predicted OF would eliminate the need to use measured data to establish an OF prior to applying ANC. The OF that was predicted using a rotating plane wave to represent the rotor noise source estimates a more accurate far-field acoustic pressure response than an OF that is generated using a monopole does. This suggests that a rotor noise source that is representative of the rotor noise source can numericaly predict an accurate OF, which can ultimately eliminate the constraint of performing a system identification prior to applying ANC.

# Chapter 7

# Active Noise Control Results

This chapter presents and discusses results using physical and virtual error sensors to apply ANC to designated far-field locations. This study focuses on rotor rotation rates at 5250 and 6000 RPM, which represent realistic rotor operating speeds. Additionally, the far-field SPL when the rotor is isolated and operating at the frequencies of interest is measured and compared to the far-field SPL when the cone, which represents part of the UAS airframe, is included in the test setup. The SPL attenuation achieved at a single far-field location using individual electrets which are located at different near-field locations on the representative airframe to estimate the virtual sensor is compared. The change in SPL at surrounding microphone locations are also shown and discussed. Lastly, the SPL attenuation achieved while the rotor operated at several rotor speeds using an observation filter that was identified at a single rotation rate is presented.

## 7.1 Initial Measurements

The SPL measured at M3 when the isolated rotor (i.e., in the free-field with no supporting boom cone included), is operating and when the cone is included in the test setup is shown in Figure 7.1. In both cases, the rotor is operating at the rotation rate 5250 RPM. The BPF, 175 Hz, is the dominant tone at 45 dB during the isolated rotor case, about 10 dB higher than the SPL of the shaft harmonic, at 87.5 Hz, and about 20 dB higher than the SPL of higher harmonics. The SPL at higher harmonics are increased by about 25 dB when the cone is included in the test configuration, due to interaction effects. Zawodny and Boyd [4] demonstrated that an airframe in close proximity to a UAS rotor can significantly amplify the higher harmonics to the same SPL as the BPF.

The cone adds a second noise source to the system, due to reradiation of the fluctuating pressure. The cone and the rotor noise sources are correlated and, depending on the observer location and the path length, the noise radiated by the cone can be either destructive or constructive to the rotor noise. Figure 7.1 shows that the shaft harmonic at 87.5 Hz decreased by 6 dB and the rotor BPF is increased by 4 dB with the addition of the cone. Figure 7.1 shows that the harmonics above 350 Hz are not excited during the isolated rotor case, but they are when the cone is included.

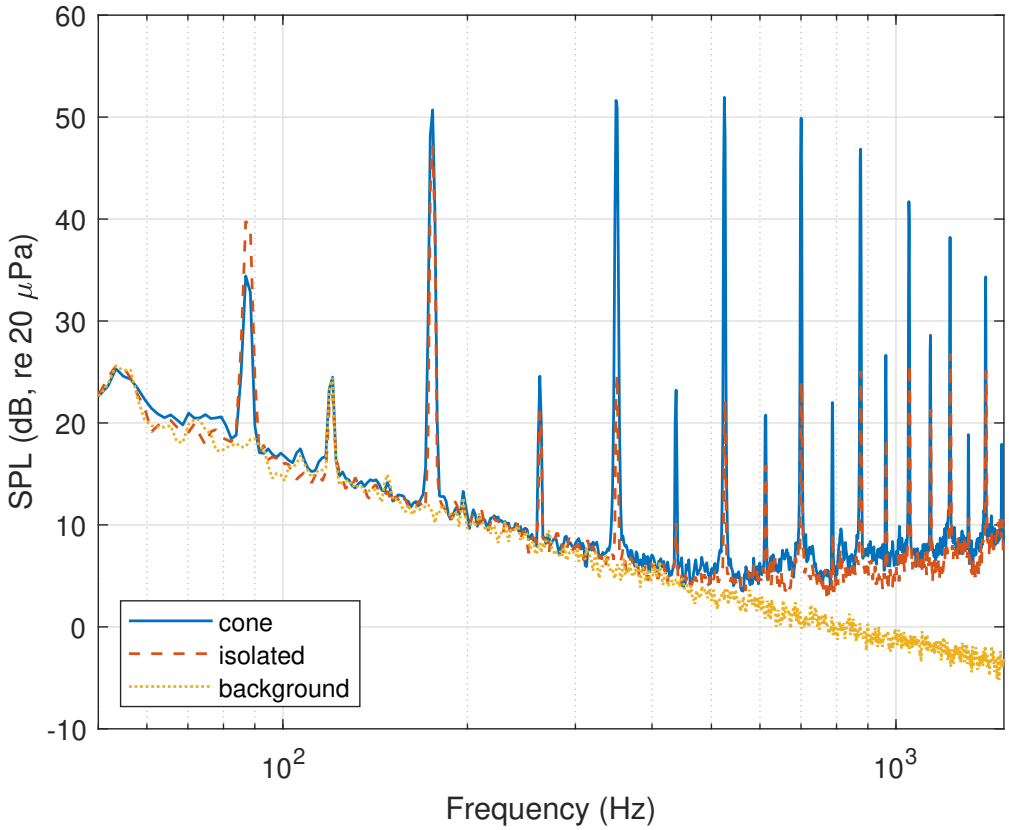


Figure 7.1: Comparison of SPL at M3 using an isolated rotor and the cone included in the test configuration, while the rotor is operating at 5250 RPM.

### 7.1.1 Electrets

Figure 7.2 shows the SPL measured by each of the electrets while the rotor is operating at 5250 RPM. The electrets are located on the surface of the conical airframe, which is placed below the rotor; electret 1 is located furthest from the rotor, electret 2 is located under the tip of the rotor blade, and electret 3 is located directly under the rotor. The SPL is highest at electret 3, while the SPL at electret 1 is the lowest. This is intuitive, given each electret's proximity to the rotor. The BPF, 175 Hz, is the highest measured SPL and the SPL begins to significantly decrease around 700 Hz. This is consistent with each electret. The measured SPLs of the BPF at electret 2 and 3 are 116 and 122 dB, respectively. The measured SPL of the BPF at electret 1 is about 90 dB. Additionally,

Figure 7.2 shows that electret 3 does not measure the third and fifth shaft harmonics, at 350 and 525 Hz, unlike electrets 1 and 2. This could be due to the electret's close proximity to the rotor, manufacturing defect, or a high noise floor. If the near-field sensor is unable to measure sound at certain the shaft harmonics, those tones will obviously not be included in the virtual error sensor, and the ANC system will not attenuate their SPL.

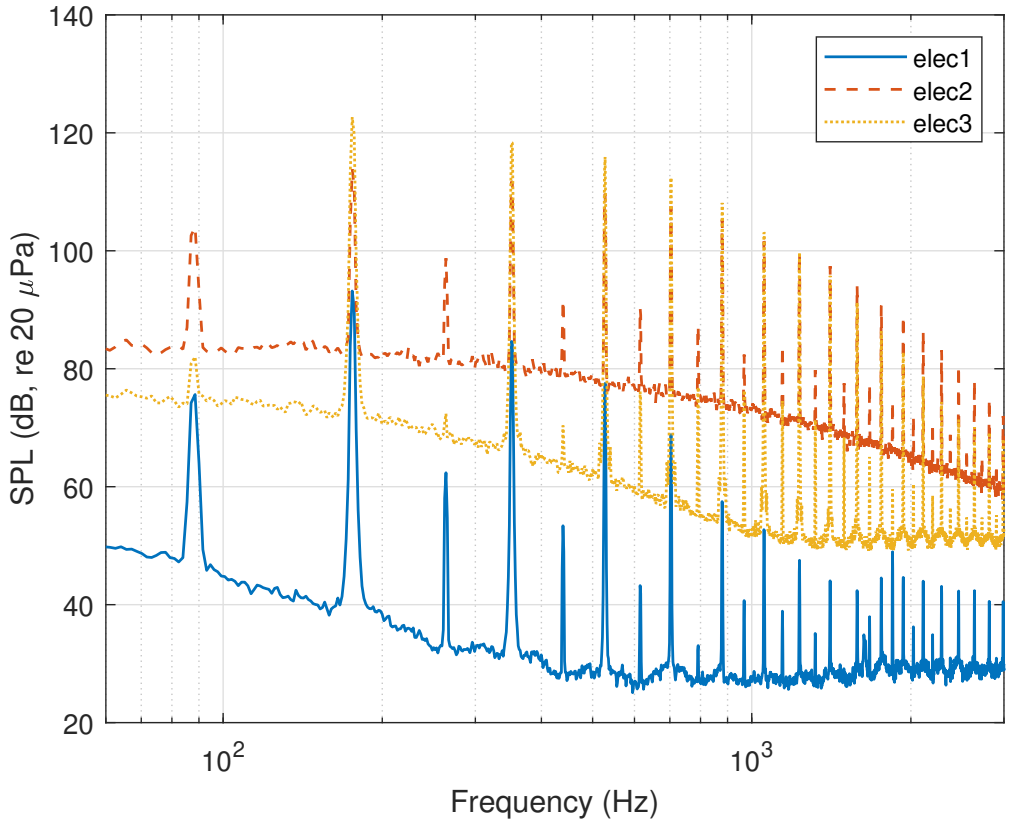


Figure 7.2: Measured SPL of near-field electrets when the cone is included in the test setup (5250 RPM.

## 7.2 ANC using Physical and Virtual Error Sensors

The SPL attenuation at M3 using ANC with virtual error sensors was compared to ANC using a physical error sensor located at M3. The response at M3 was observed first because M3, which was

positioned at the elevation angle 22.5°, captures a majority of harmonic content. In the case using a physical sensor, the designated microphone location, M3, provides the error signal to the control system for both 5250 and 6000 RPM. Figure 7.3a shows the measured far-field SPL using M3 to provide the error response to the system compared to the measured SPL at M3 during open-loop data collection while the rotor is operating at 5250 RPM. ANC using a physical sensor attenuates the SPL of the shaft harmonic, 87.5 Hz, by 17 dB at the sensor location. The SPL of the BPF is also significantly attenuated by 30 dB. The SPL of the third shaft harmonic, 262.5 Hz, is also attenuated. Despite high SPL attenuation at lower harmonics, higher harmonics and tones, above 600 Hz, are significantly amplified. This amplification is called control spillover [53] and could be due recirculation effects in the chamber that are created by long periods of data collection. This spillover should be addressed in future testing. Figure 7.3b shows the measured SPL at M3 using a virtual error sensor to apply ANC at the far-field location compared to the SPL at M3 during open-loop data collection. The far-field SPL is attenuated at the shaft harmonic and BPF by about 7 and 13 dB. The third shaft harmonic is amplified by 9 dB, which could be a result of inaccuracies at this frequency in the OF. However, this amplification is nearly 20 dB lower than the dominant tones and does not amplify the overall SPL.

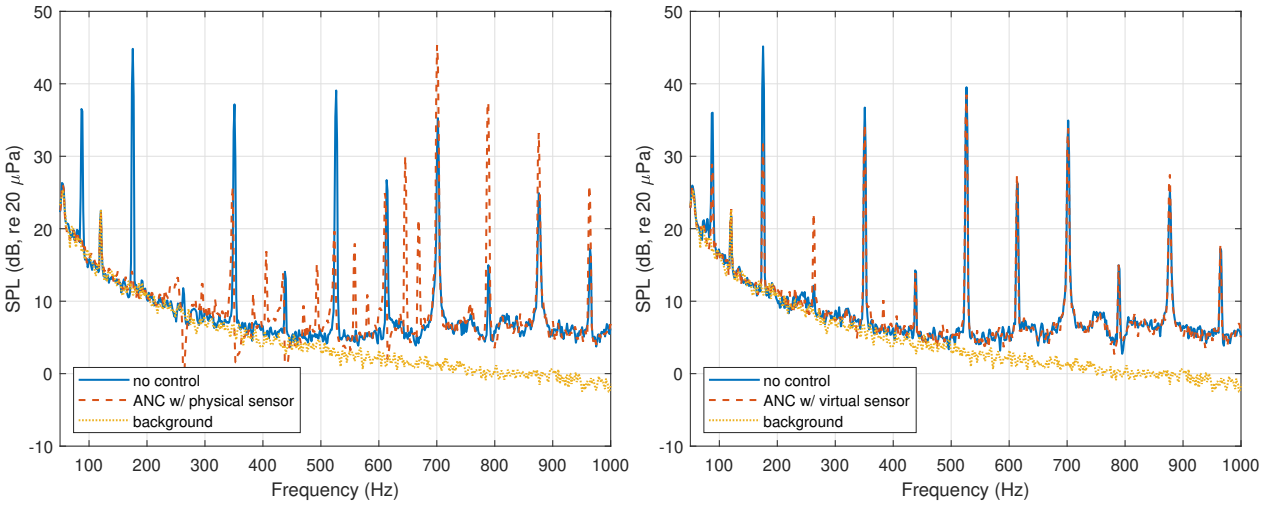


Figure 7.3: Comparison of ANC using (a) a physical sensor at M3 and (b) using a virtual error sensor developed through Electret 2 (RPM = 5250).

Figure 7.4a shows the measured far-field SPL using the physical microphone M3 to provide the error signal to the control system compared to the measured far-field SPL during open-loop data collection while the rotor is operating at 6000 RPM. Similar to the case of 5250 RPM, the SPL of the shaft harmonic, 100 Hz, is attenuated by 20 dB. Additionally, the SPLs of the BPF and third shaft harmonic, 200 Hz and 300 Hz, are attenuated by 40 and 30 dB, respectively. The SPL of the fourth and sixth shaft harmonics, 400 and 600 Hz, are attenuated by about 30 and 15 dB. As in the 5250 RPM case, harmonics above 700 Hz are significantly amplified, which could again indicate a problem related to the controller. The far-field SPL using a virtual error sensor to apply ANC for the case of 6000 RPM is shown in Figure 7.4b. The SPL attenuation is similar to the attenuation achieved during the 5250 RPM case. The SPL of the first shaft harmonic is attenuated by 7 dB and the SPL of the BPF is attenuated by 12 dB. However, the third shaft harmonic is amplified nearly 15 dB. Again, the SPL of the higher harmonics are not amplified. Although ANC using a physical sensor best attenuates the far-field SPL inside the frequency range of interest (50-425 Hz), Figures 7.3b and 7.4b show that changes in the far-field SPL of higher harmonics while applying ANC

using a virtual sensor are small.

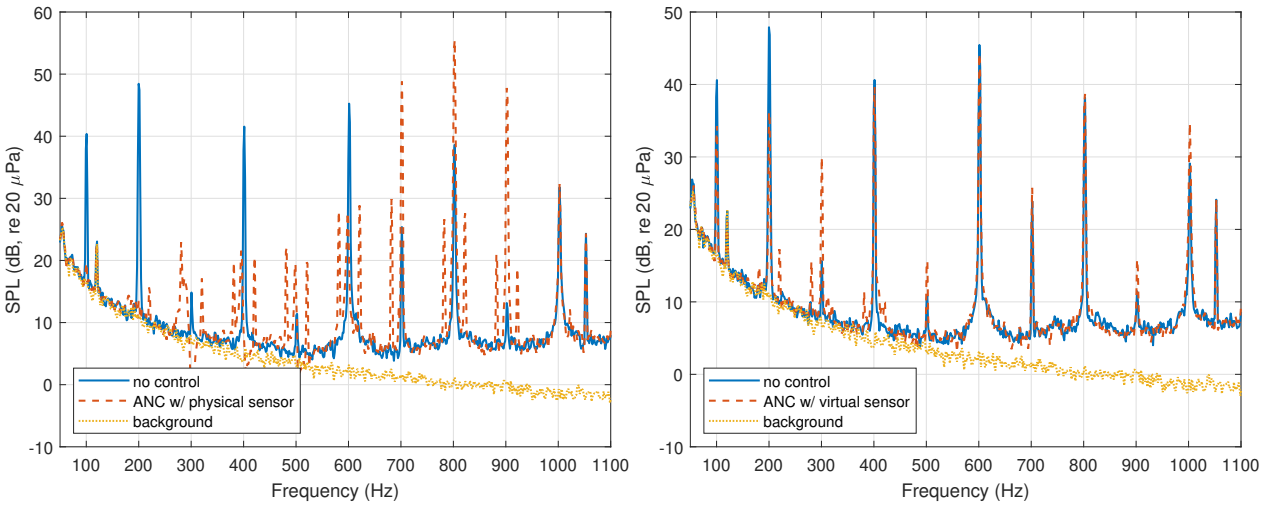


(a) (b)

Figure 7.4: Comparison of ANC using (a) a physical sensor at M3 and (b) using a virtual error sensor developed through Electret 2 (RPM = 6000).

## 7.3 Individual Electret Performance

The signals from each electret were individually used to estimate the far-field response at M3, which was subsequently used to apply ANC to the remote location when the rotor was operating at 5250 and 6000 RPM. Figures 7.5 and 7.6 compare the open-loop far-field SPL at M3 to the SPL at M3 when each individual electret was used to estimate the far-field pressure response. Each electret achieves comparable levels of attenuation. Figure 7.5 shows that each electret attenuated the SPL of the BPF (175 Hz) at M3 between 9 and 12 dB. Changes in SPL at the second harmonic, 350 Hz, and higher harmonics are small. Similarly, Figure 7.6 shows that the SPL of the BPF (200 Hz) at M3 is reduced between 11 and 15 dB when each individual electret is used to establish a virtual sensor and subsequently apply ANC to the remote location at M3. Again, the changes in SPL due to active cancellation at the second harmonic (400 Hz) and higher harmonics are small, as discussed

in section 7.2. Electret 2 models an OF with the least MSE and, as previously demonstrated in Figure 5.11, electret 2 and the Kulite transducer measured similar pressure levels when the Kulite was placed next to electret 2. Therefore, electret 2 was chosen to establish the virtual error sensor for the remainder of testing.

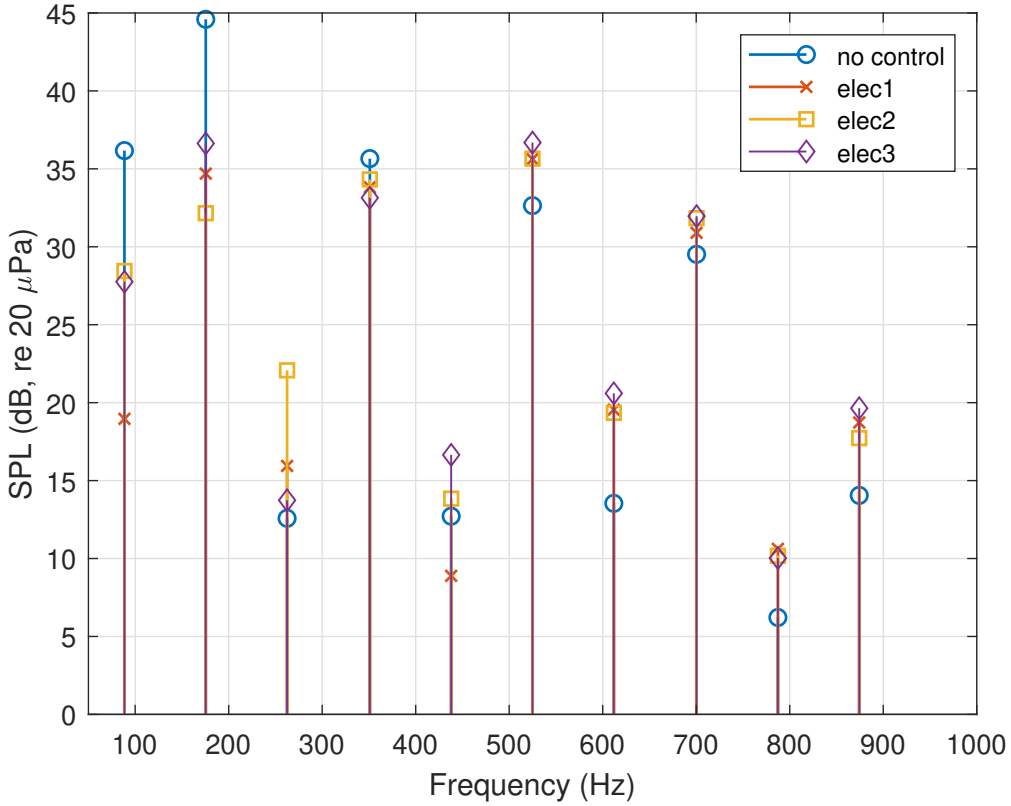


Figure 7.5: Measured SPL at M3 while the rotor is operating at 5250 RPM during open-loop measurement compared to the SPL during ANC using each electret to develop the virtual error sensor.

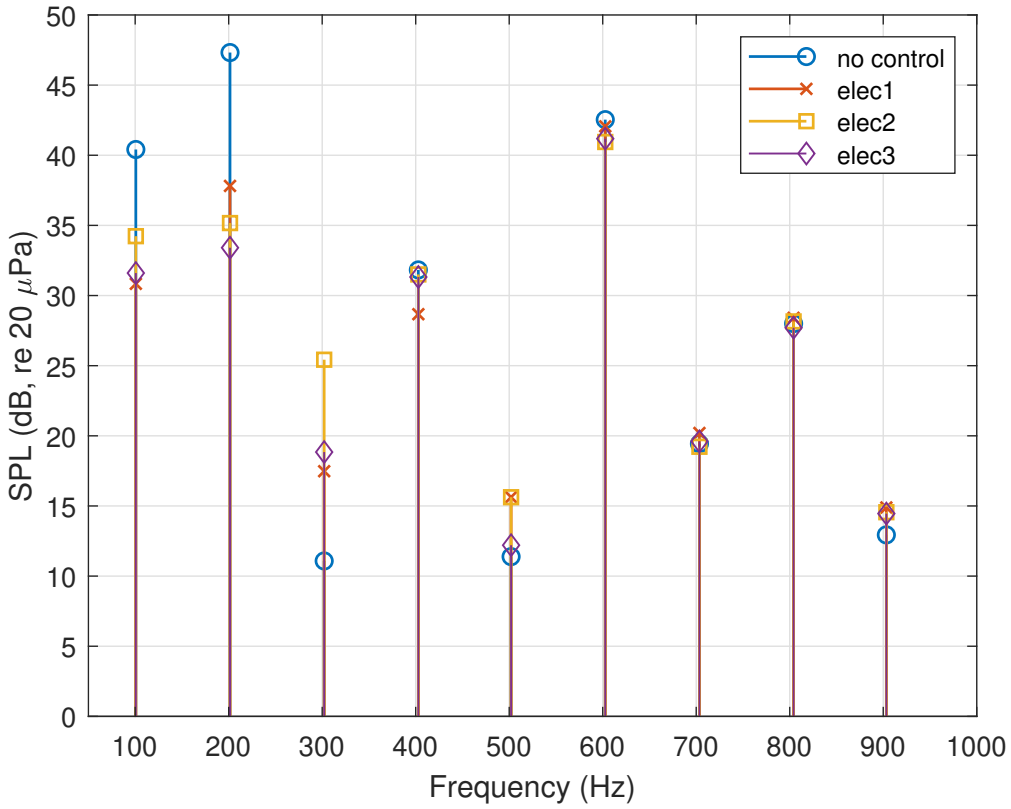


Figure 7.6: Measured SPL at M3 while the rotor is operating at 6000 RPM during open-loop measurement compared to the SPL during ANC using each electret to develop the VES.

## 7.4 SPL Reduction at Surrounding Locations

In addition to measuring the far-field SPL at the targeted microphone location during ANC with a virtual error sensor, the SPL at surrounding microphone locations was also measured. It is worth noting that the microphones are positioned at different elevation angles, but share the same azimuthal angle. Figure 7.7 shows the change in SPL at each microphone using an ANC system designed to minimize the estimated farfield pressure at M3. The SPL is most reduced at microphones closest to M3. The SPL of the shaft harmonic, 87.5 Hz, is reduced at M2 and M4 by 5 and 4 dB, respectively. The SPL of the microphones furthest from M3 are reduced least, following the assumption that the zone of quiet is larger for low frequencies and becomes smaller as wavelength

increases [16]. The SPL of M1 is reduced by 3 dB and the SPL of M5 is amplified by 4 dB at the shaft harmonic. Similar to M3, the SPL of the surrounding microphones are most reduced at the BPF. The measured SPL of the BPF at M2 and M4 are reduced by 10 and 9 dB, respectively, while SPL changes at higher harmonics are small.

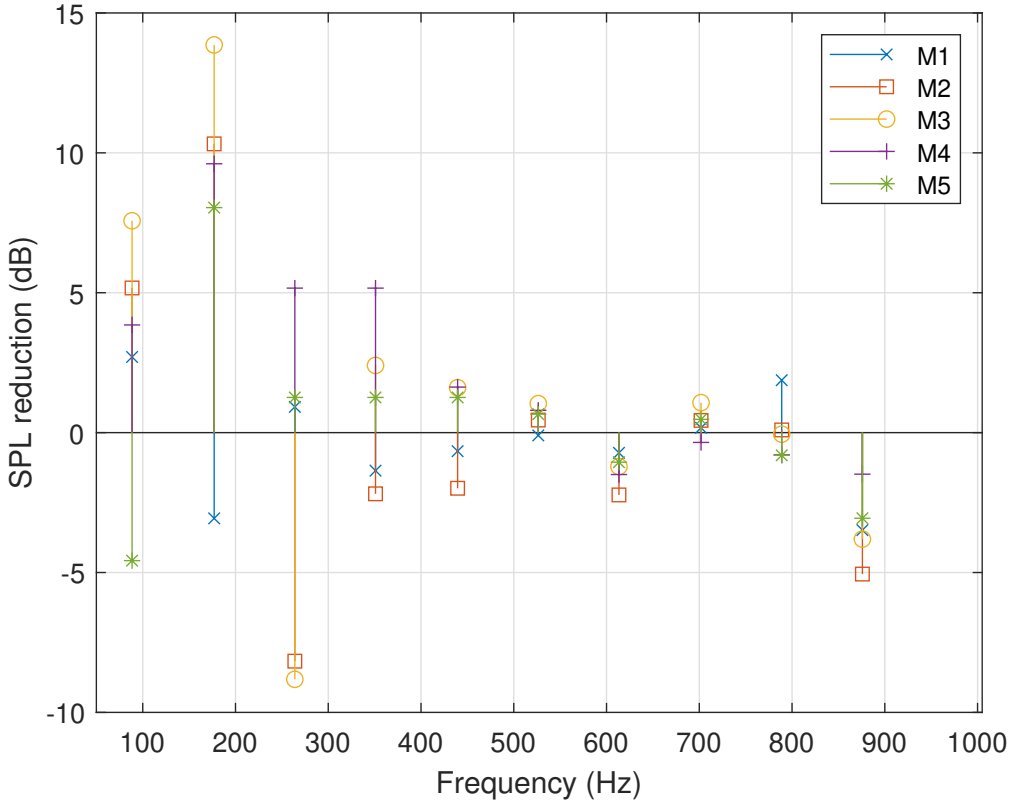


Figure 7.7: Far-field microphone response to ANC using the VES developed with Electret 2 (RPM = 5250).

Figure 7.8 shows the SPL reduction achieved at surrounding microphone locations while the rotor is operating at 6000 RPM. Similar to the results shown in Figure 7.7, the SPL of microphones close to M3 are most reduced. However, unlike the 5250 RPM case, the highest level of SPL attenuation at the shaft harmonic, 100 Hz, is not achieved at M3. The SPL at microphones M4 and M5 are most reduced at the shaft harmonic, 100 Hz, by nearly 10 dB. It is worth pointing out that the SPL at M1 is slightly amplified, similar to the 5250 RPM case. The SPL reduction at the BPF in Figure

7.8 is more consistent with that in Figure 7.7; the SPL at M3 is reduced most, by over 10 dB. Aside from M3, the SPL at surrounding microphone locations M2 and M4 are reduced most by 10 and 7 dB, respectively. Microphones M1 and M5 were also designated as observer locations and the electret 2 was used to create the virtual error sensor at both locations. The SPL reductions at both locations are consistent with those achieved using M3 as the targeted far-field location, and the results are shown in Appendix A.1 and A.2.

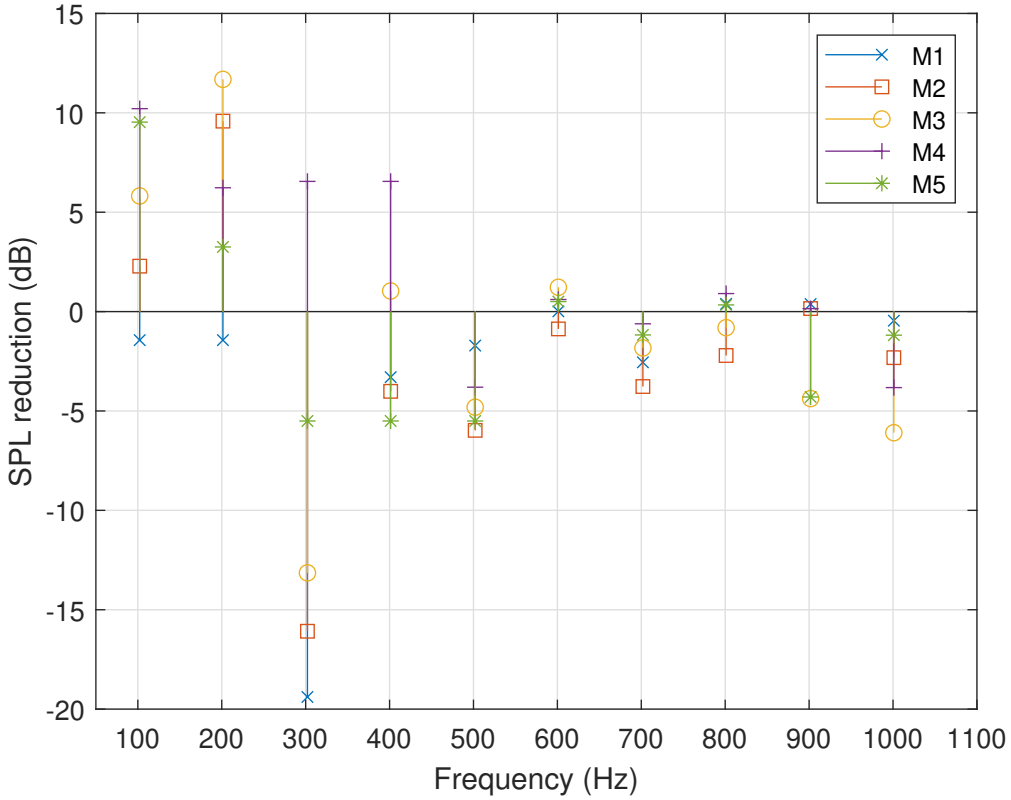


Figure 7.8: Far-field microphone response to ANC using the VES developed with Electret 2 (RPM = 6000).

## 7.5 Observation Filter Length

This section examines the length of the filter required to create an OF model that captures the magnitude and phase characteristics of the OF while the rotor was operating at different speeds.

While it is possible to identify different OFs for different operating speeds and conditions, it is useful to understand how robust the model is to variations in the rotation rate. The rotor rotation rate was measured over the range 5000-5500 RPM in increments of 50 RPM. A model of the OF was identified at the rotation rate 5250 RPM. The OF between electret 2 and M3 during each rotation rate was estimated using the measured data. The estimated magnitude and phase values at the BPF and harmonics were compared to the continuous OF model. The curves in Figure 7.9 show the magnitude and phase of the OF identified with the rotor at 5250 RPM. Magnitude and phase estimates from measured data are shown in Figure 7.9 with data markers. The markers are located at the shaft harmonics that correspond to the rotation rates 5000, 5250, and 5500 RPM. Markers that coincide with the OF model indicate that the OF model is capable of representing a range of rotation rates, and that it might not be necessary to perform a different system ID for each rotation rate.

The number of filter coefficients used to model the OF was changed to determine the length of the filter which creates an OF that captures the magnitude and phase characteristics over the range of rotation rates. Figure 7.9a shows that a filter of 256 coefficients does not capture a majority of the phase components of both 5000 and 5500 RPM. The filter using 512 coefficients, shown in Figure 7.9b better captures the phase characteristics of the rotation rates up to about 350 Hz, the fourth shaft harmonic of the OF identified with the rotor at 5250 RPM. Finally, the OF model that is estimated using 1024 coefficients estimates the phase components of each rotation rate up to around 700 Hz, although the OF model does not capture several phase values between 450 and 500 Hz. The OF model typically estimates the magnitude and phase values when the coherence between the far-field microphone and the near-field electret, which are used to esitmate the OF, is high, above 0.8.

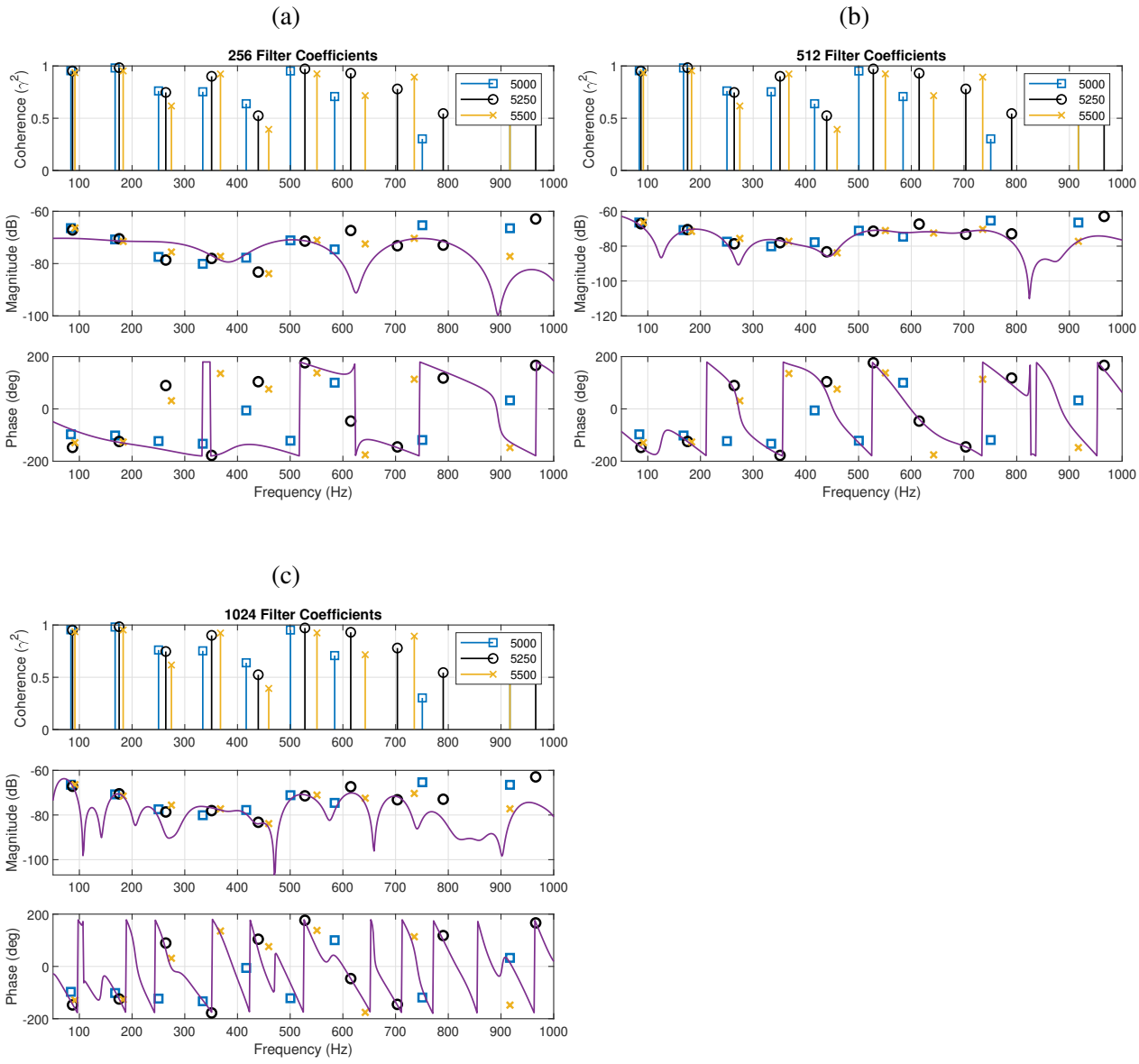


Figure 7.9: Comparison of the magnitude and phase response for the OF (identified at 5250 Hz) with magnitude and phase estimates from measured data at three rotation rates.

The SPL attenuation achieved at the shaft rotation rates (5000, 5250, and 5500 RPM) and several harmonics were measured and compared. Each closed-loop measurement used a single OF, which was identified at 5250 RPM, to explore the range of rotation rates that the OF could accurately

estimate. Figure 7.10 shows the SPL reduction achieved at M3 using the VES to apply ANC during the rotation rates 5000, 5250, and 5500 RPM. The SPL of each rotation rate is most reduced at their respective shaft harmonics and BPFs. The SPL of M3 is most attenuated at frequencies corresponding to the rotation rate 5250 RPM; the SPL of the shaft rotation rate (87.5 Hz) and the BPF (175 Hz) is attenuated by 7 dB and 13 dB, respectively. The SPL of the third shaft harmonic (262.5 Hz) is amplified nearly 9 dB, which could indicate discrepancies in the OF at this frequency. The SPL of the rotation rate of 5000 RPM is attenuated at the corresponding shaft harmonic (83.4 Hz) by about 5 dB. Further, the SPL of the rotation rate of 5500 RPM is attenuated at the corresponding BPF (183.3 Hz) by about 5 dB. The SPL changes at higher harmonics are modest, indicating that the OF can be used to estimate the VES and subsequently apply ANC over the narrow rotation rate range at the frequency range of interest without amplifying higher harmonics.

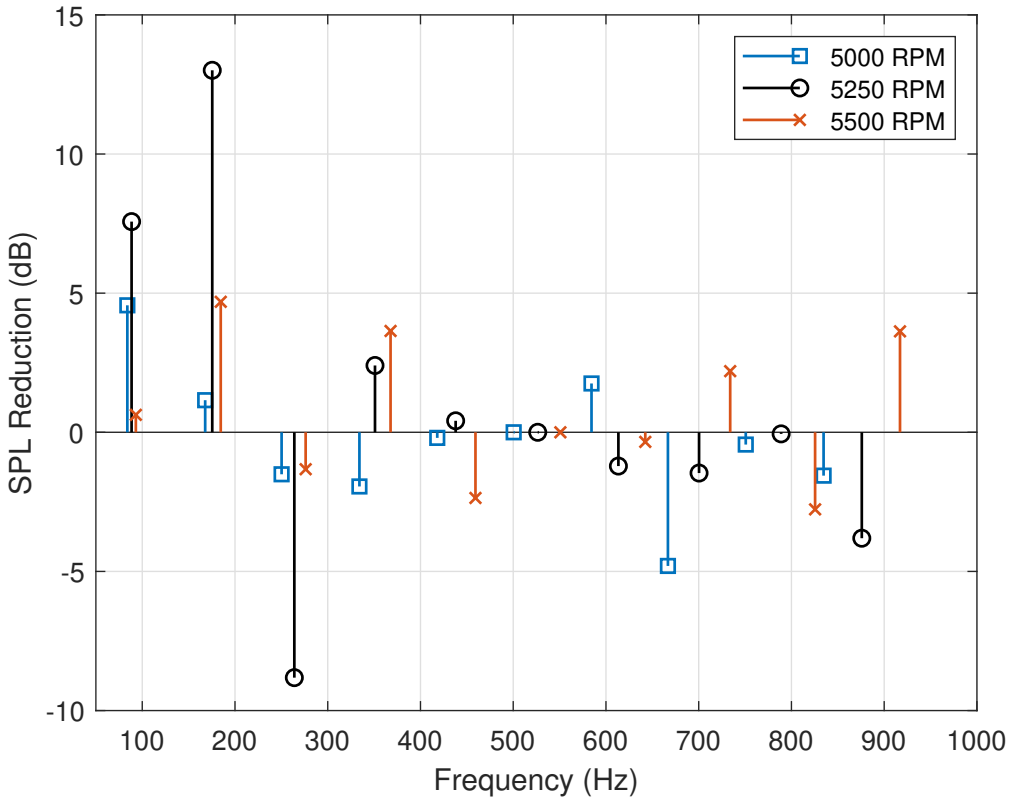


Figure 7.10: Comparison of SPL reduction at M3 when a single OF, identified at 5250 RPM, is used to estimate the virtual sensor and apply ANC during various rotation rates.

Figure 7.11 shows the SPL reduction achieved at M3 when the rotor is operating at speeds ranging from 5150 RPM to 5350 RPM. Again, the OF was identified while the rotor is operating at 5250 RPM. The SPL of the neighboring rotation rates are actively attenuated at their respective shaft harmonics and BPFs. Similar to Figure 7.10, changes in the SPLs of higher harmonics are small, indicating that the OF can be used to estimate the response at the virtual location and subsequently reduce the SPL over a range of rotation rates, and the OF will not need to be identified for each change in rotor speed within a limited rotor speed range.

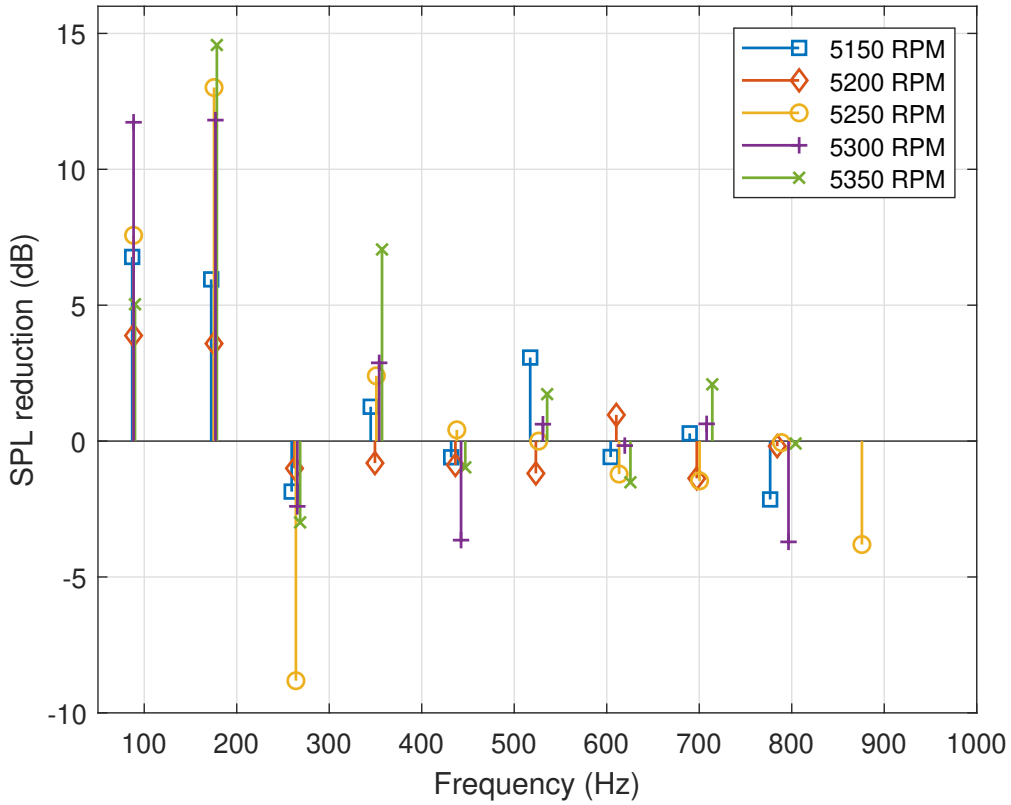


Figure 7.11: Comparison of SPL reduction at M3 when a single OF, identified at 5250 RPM, is used to estimate the virtual sensor and apply ANC during various rotation rates.

## 7.6 Perpendicular Configuration of the Supporting Cone

The active performance of a second configuration in which the rotor supporting boom cone was positioned perpendicular relative to the microphone array was tested. This second configuration is helpful in observing the amount of SPL active attenuation at different testing configuration. Prior to applying ANC at each microphone, a new system ID was performed using electret 2 and a new virtual sensor system was established. While the coherence between the reference tachometer and the electret appears comparable to that of the "in-line" cone configuration, the coherence between the error microphone and the reference tachometer is much lower at the third shaft harmonic, as can be seen in figures 7.12. Figure 7.13 shows that similar to when the cone is in-line to the microphone array, the addition of the cone perpendicular to the microphone array amplifies the SPL of higher harmonics.

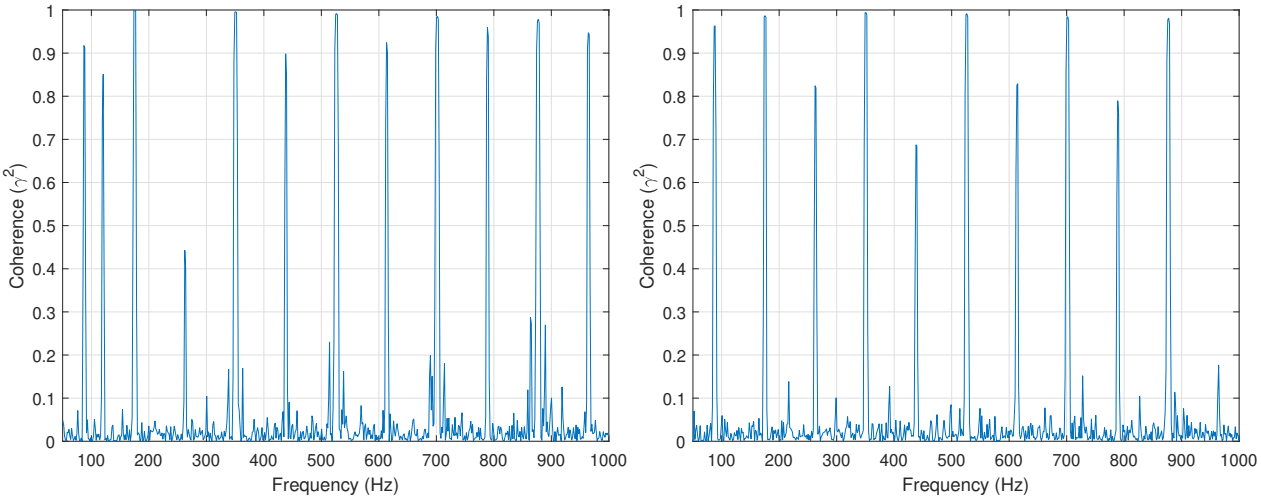


(a) (b)

Figure 7.12: Coherence between the tachometer and (a) M3 and (b) electret 2.

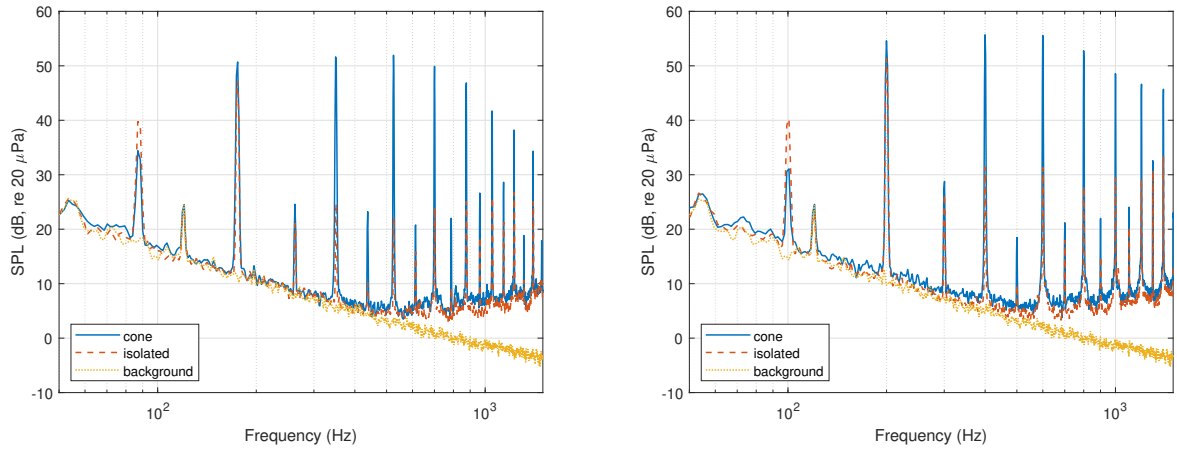


(a) (b)

Figure 7.13: Comparison of the SPL at M3 when the rotor is operating at (a) 5250 RPM and (b) 6000 RPM when the rotor is isolated and then the cone is included in the test setup.

### 7.6.1 ANC at Observer Locations

Electret 2 was used to create virtual sensors at M1, M3, and M5 when the cone was perpendicular to the microphone array. Figure 7.14 compares the SPL reduction at M3 using both traditional ANC and ANC with a virtual error sensor when the rotor is operating at 5250 RPM. The SPL using traditional ANC is shown in Figure 7.14a. The error response signal is measured and provided to the control system using M3. The SPL of the shaft harmonic (87.5 Hz) is reduced by nearly 15 dB. Additionally, SPL of the the BPF (175 Hz) is attenuated by 30 dB. The harmonics up to around 600 Hz are also significantly attenuated. Here the higher harmonic SPL reduction is much higher compared to the results presented in Figure 7.3a. Additionally, Figure 7.14a shows less control spillover, which could be due to a better system identification than the one established in the in-line testing configuration. Figure 7.14b compares the open-loop SPL and the SPL at M3 using electret 2 to establish the virtual error sensor. The SPLs of the shaft harmonic and the BPF are attenuated by about 6 dB and 8 dB, respectively. The SPL at the third shaft harmonic (262.5

Hz) is amplified by about 11 dB. However, similar to Figure 7.3b, the amplification at this tone is still much smaller than the dominant tones. The SPL of the fourth shaft harmonic (350 Hz) is attenuated by 5 dB, while the SPLs of higher harmonics are also not amplified.

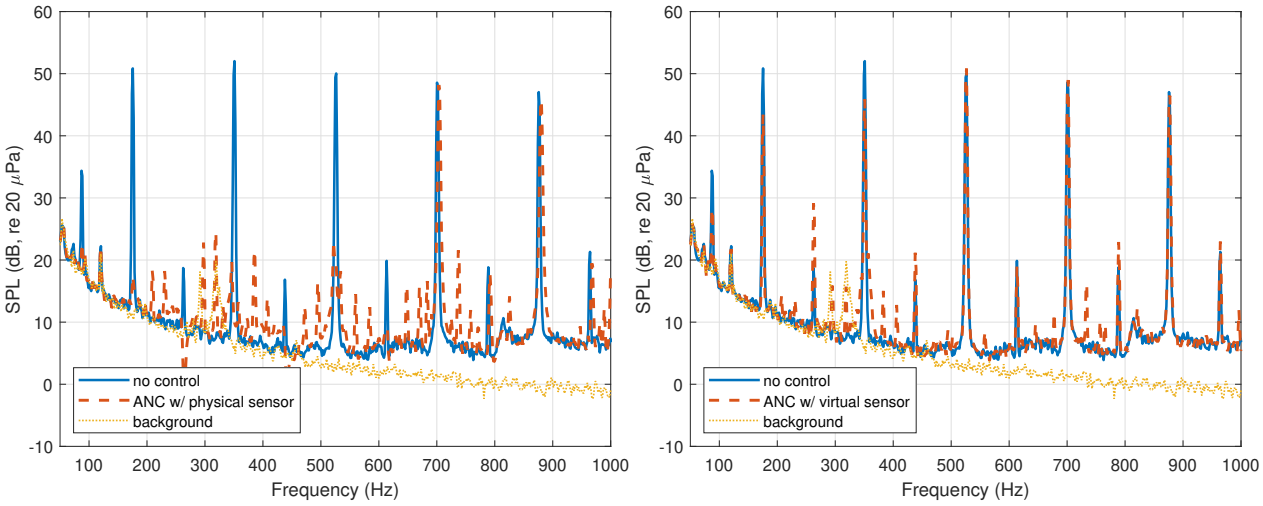


(a) (b)

Figure 7.14: Comparison of ANC at M3 using a (a) physical sensor and (b) a virtual error sensor developed through Electret 2 (RPM = 5250).

Similar results are observed in Figures 7.15, when the rotor is operating at 6000 RPM. Figure 7.15a shows that traditional ANC using a physical sensor at M3 attenuates the SPLs of the shaft harmonic (100 Hz) and BPF (200 Hz) by 15 and 40 dB, respectively. The SPLs of harmonics through 600 Hz are also significantly attenuated. Figure 7.15b shows that the SPL of the shaft harmonic is attenuated by 4 dB. Additionally, the BPF is attenuated by 9 dB. Similar to the 5250 RPM case, the third shaft harmonic, 300 Hz, is amplified by 5 dB, although the amplified tone is much smaller than dominant tones. Again, applying ANC using a virtual error sensor does not amplify the SPLs at higher harmonics. Although ANC with a physical sensor achieves greater levels of SPL reduction, ANC using a virtual sensor is capable of reducing the SPL of the BPF at M3 by at least 8 dB. Similar results are achieved at M1 and M5, which can be seen in results presented in Appendix A.3.

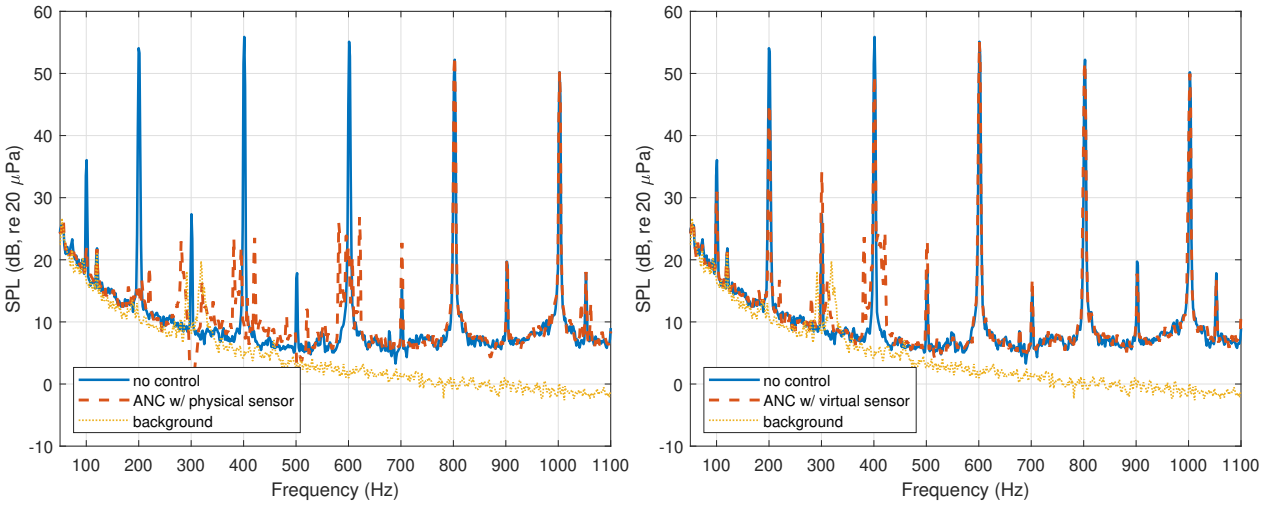


(a) (b)

Figure 7.15: Comparison of ANC at M3 using a (a) physical sensor and (b) a virtual error sensor developed through Electret 2 (RPM = 6000).

### 7.6.2 SPL Reduction at Surrounding Microphone Locations

The SPL reduction achieved at the designated virtual microphone location, M3, and surrounding microphone locations is shown in Figures 7.16 and 7.17. The SPL attenuation achieved while the rotor is operating at 5250 RPM is shown in Figure 7.16. The SPLs at each microphone are reduced at the shaft harmonic (87.5 Hz) and the BPF (175 Hz). Similar to Figure 7.7, the microphone locations closest to the virtual location are reduced most, and M5, the microphone furthest from M3, is reduced least. However, the SPL of the third shaft harmonic (262.5 Hz) is significantly amplified, which could be attributed to inaccuracies in the OF. The SPL of the fourth shaft harmonic (350 Hz) is also attenuated by 7 dB at M3 and surrounding microphone locations. Changes in the SPL at higher harmonics are small. Similar results are obtained while the rotor is operating at 6000 RPM, shown in Figure 7.17. The change in SPL at surrounding microphone locations is similar when the virtual location is defined at M1 and M5, which can be seen in results presented in Appendix A.4.

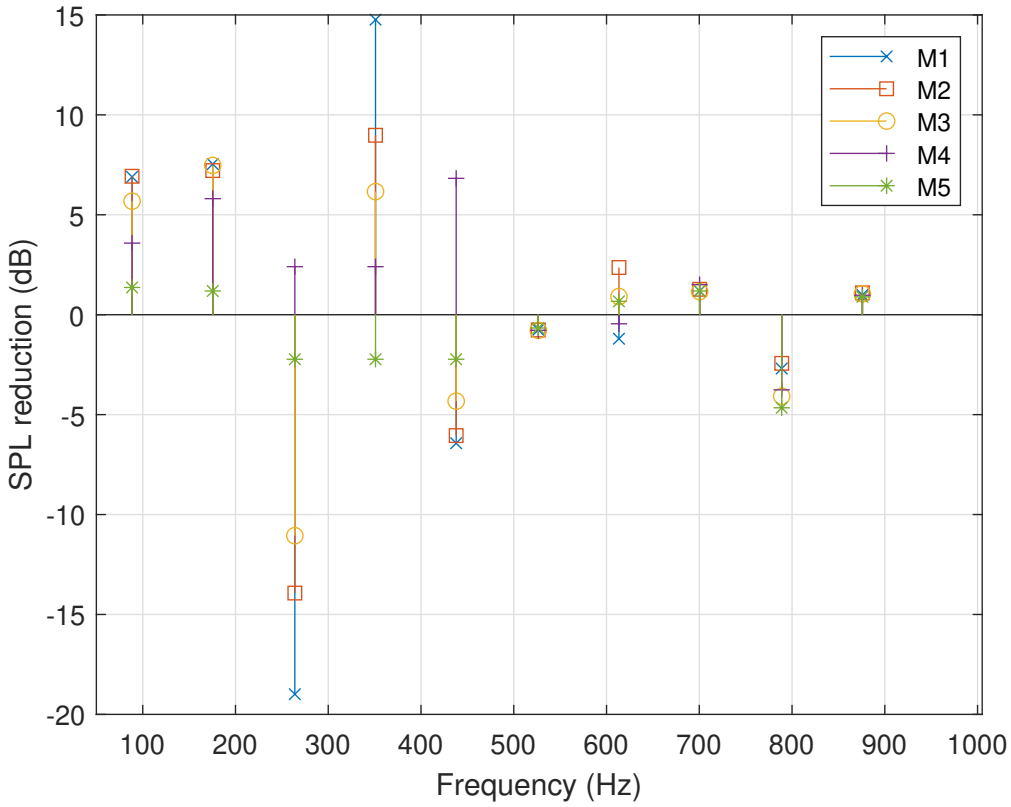


Figure 7.16: ANC response at M3 using the VES developed with Electret 2 when the rotor is operating at 5250 RPM.

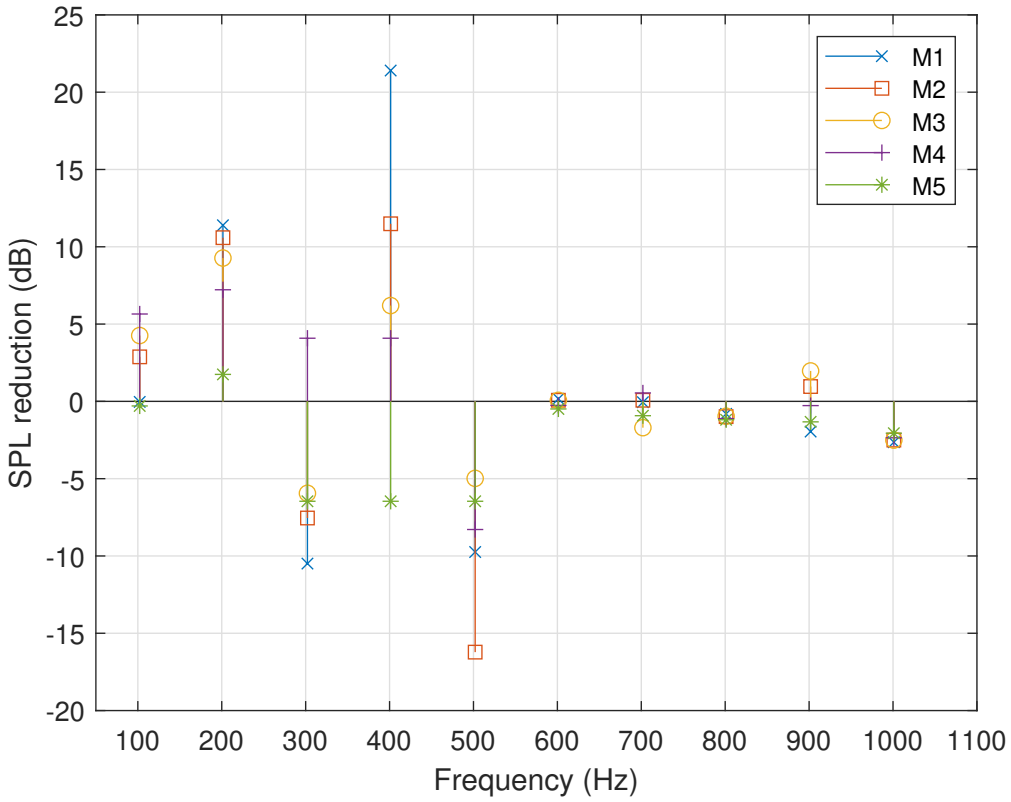


Figure 7.17: ANC response at M3 using the VES developed with Electret 2 when the rotor is operating at 6000 RPM.

### 7.6.3 Observation Filter Length

The length of the OF required to capture the magnitude and phase characteristics of a range of rotation rates was investigated. Similar to the in-line configuration, a system ID was performed to establish the paths between the speaker, electret 2, and the virtual location, M3, when the cone was arranged perpendicular relative to the microphone array. A single OF model was identified at 5250 RPM and compared to the measured magnitude and phase values over the range of rotation rates 5000-5500 RPM, which were collected in increments of 50 RPM. Figure 7.18 shows how the number of filter coefficients affects the OF model's ability to capture neighboring rotation rates' magnitude and phase values.

If the measured magnitude and phase values at the shaft harmonics of neighboring rotation rates coincide with the OF model line, it is assumed that the OF model can be used to establish the VES and subsequently be used with the ANC system to reduce the SPL at the corresponding frequencies. Figure 7.18a shows that an OF model created with 256 filter coefficients is only capable of estimating the magnitude at the BPF, 175 Hz. The measured phase values that are associated with the angular speed 5250 RPM coincide with the OF model, as well. The measured magnitude and phase values of the shaft harmonics that are associated with the rotation rates 5000 RPM and 5500 RPM are not captured by the OF model. Therefore, 256 filter coefficients does not create an OF model that may estimate neighboring rotation rates.

Figure 7.18b shows the OF model estimated using 512 filter coefficients. Magnitude values at the rotor BPF and harmonics corresponding the rotation rate 5250 and 5000 RPM are captured through around 500 Hz. Additionally, phase values at each rotation rate are largely captured through 900 Hz. Lastly, the OF model was identified using 1024 filter coefficients, shown in Figure 7.18c. The OF model captures more of the magnitude and phase values for the rotation rate 5500 RPM through around 350 Hz. So, the OF model with 1024 filter coefficients was used in-conjunction with the ANC system to observe the SPL reduction achieved at various rotor rotation rates.

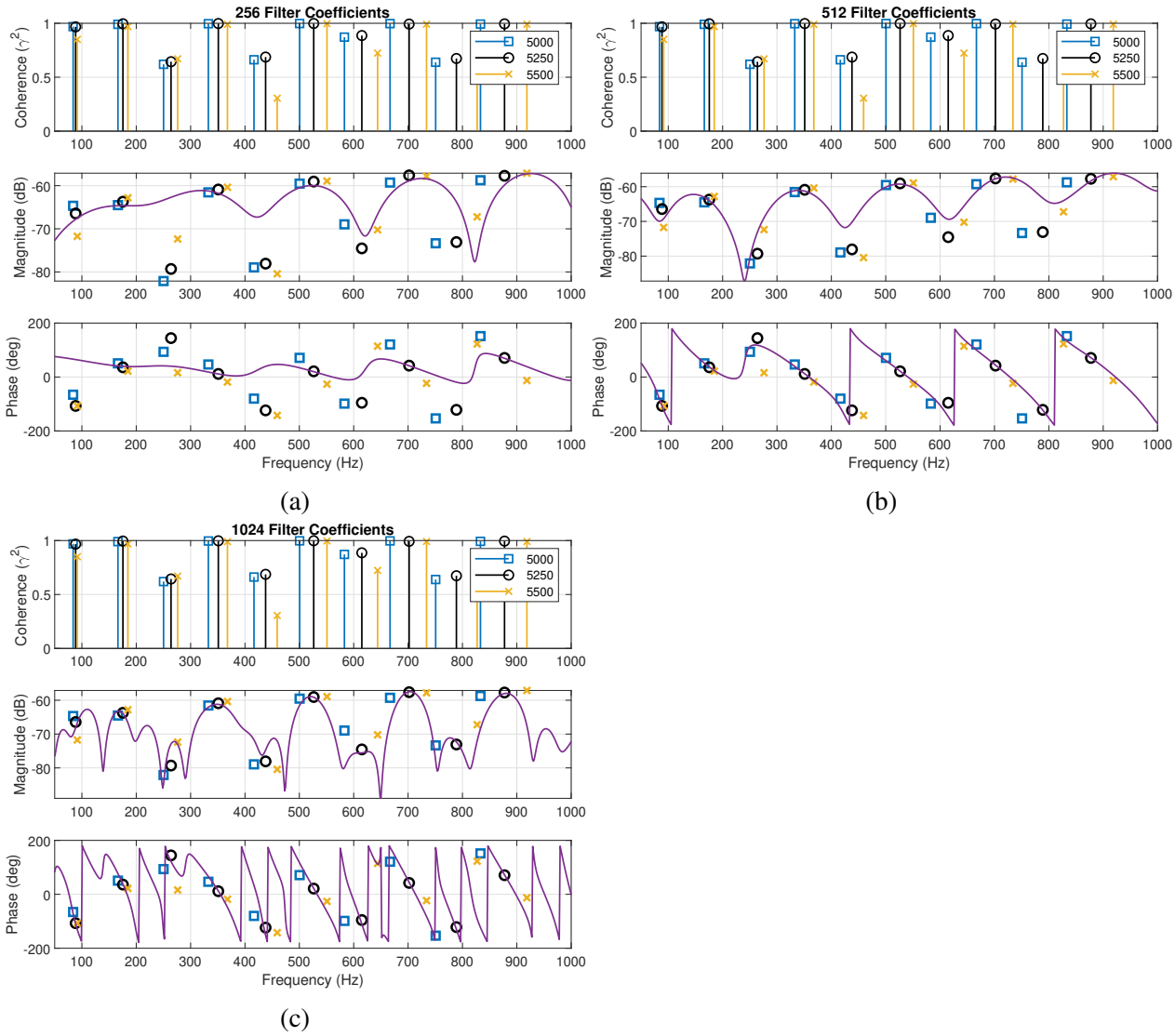


Figure 7.18: Comparison of number of filter coefficients used to create a model of the OF, M3.

The OF model, which was identified at 5250 RPM, was then used with the ANC system to attenuate the SPL at the virtual location, M3, while the rotor is operating at rotation rates ranging from 5000-5500 RPM. Figure 7.19 shows the SPL reduction at frequencies corresponding to their shaft harmonics and harmonics. The SPLs of each rotor BPF is reduced most, ranging from 5-8 dB. The SPL of the third shaft harmonic of each rotation rate is significantly amplified, however, which could be a result of an inaccurate OF, as previously mentioned. Additionally, coherence is low

between the reference signal, provided by the optical tachometer, and the response at the virtual location at this frequency. This is consistent for other locations of SPL amplification, as well. SPL changes at harmonics above 450 Hz are modest. Similar results are shown in Figure 7.20, which show the SPL reduction at rotation rates ranging from 5150-5350 RPM. Generally, an OF that is identified at a single rotation rate can be used to establish the VES and apply ANC to a virtual location over a narrow range of rotation rates. However, it is likely that maximum SPL attenuation will not be achieved at each neighboring rotation rate.

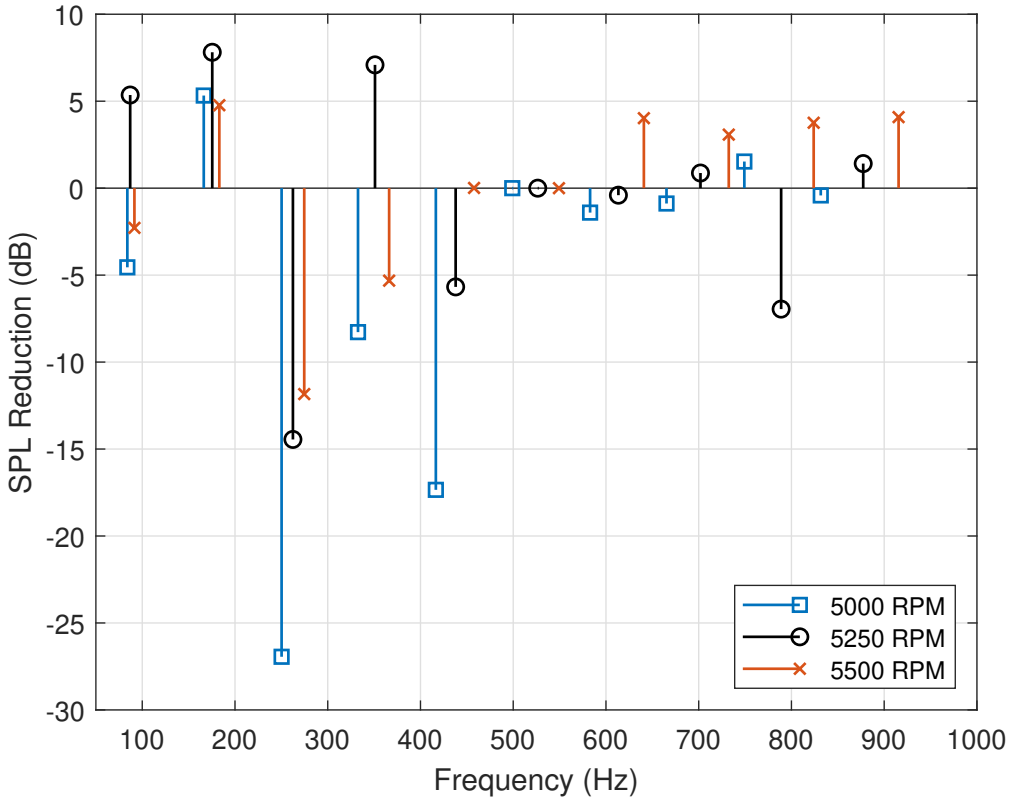


Figure 7.19: SPL attenuation achieved at M3 when the OF identified at 5250 RPM is used for various rotation rates.

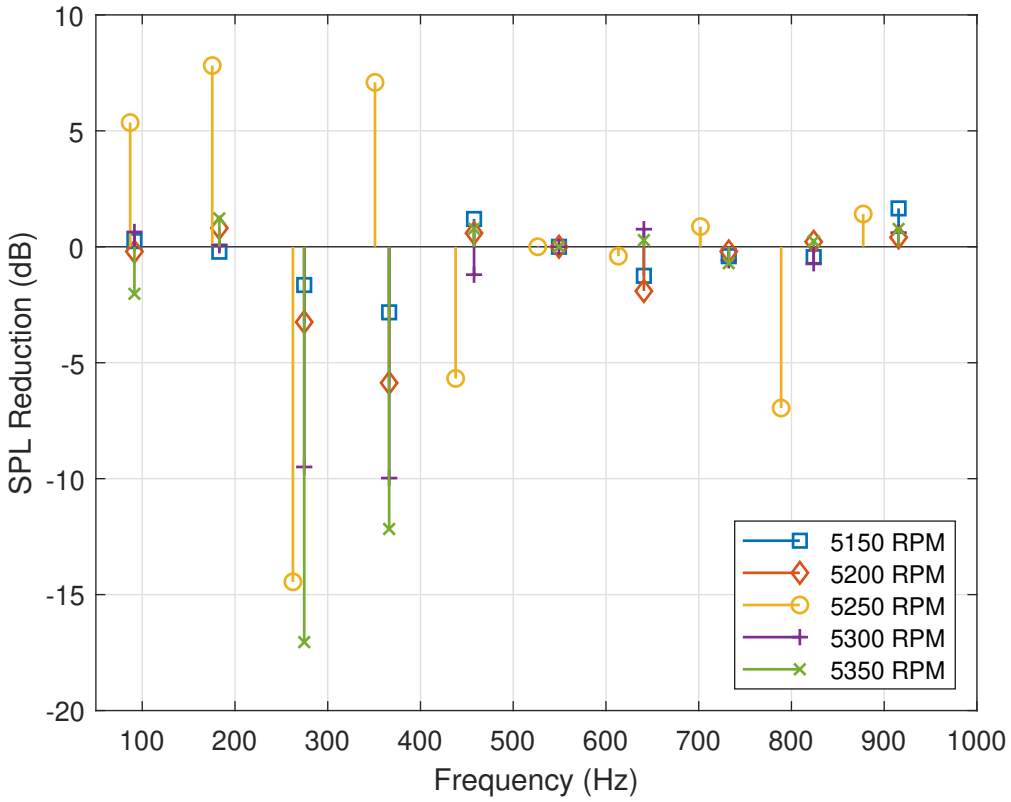


Figure 7.20: SPL attenuation achieved at M3 when the OF identified at 5250 RPM is used for various rotation rates.

## 7.7 Discussion

This chapter presented results showing the SPL attenuation achieved while implementing ANC at a designated far-field observer location using a virtual error sensor and compared it to the attenuation achieved using a physical sensor at the far-field location. Using a physical sensor to apply ANC at observer locations attenuated the SPL of the BPF and lower harmonics nearly 30 dB, however, this application is limited by the physical location of the error sensor, which is not provided in real applications. Although ANC using a physical sensor achieved greater levels of SPL attenuation at the observer location, ANC using a virtual error sensor can attenuate the SPL at the virtual location between 6-13 dB at the shaft harmonic and the BPF. This SPL attenuation demonstrated that the

virtual sensing technique that was used in conjunction with the ANC system in this study, the remote microphone technique (RMT), can be used to apply ANC at far-field observer locations. SPL changes due to active inputs at higher harmonics were minimal. Additionally, this chapter compared the SPL reductions at microphones surrounding the observer location. Surrounding microphones were located at different elevation angles, but shared the same azimuthal angle so, while the SPLs of each microphone at the shaft harmonic and BPF are reduced, it is important to note that this does not demonstrate global attenuation. Generally, the SPLs at microphones located closest to the designated virtual location were reduced most at the shaft harmonic and the BPF. The SPLs of microphones located furthest from the virtual location were reduced least. Additionally, SPL changes at surrounding microphones were modest at higher harmonics.

Observation filter models of different lengths were established at a single rotation rate to determine which filter length best captures the measured OF magnitude and phase characteristics over a narrow range of rotation rates spanning 500 RPM. Observation filters containing 1024 filter coefficients generally captured the magnitude and phase values from the shaft harmonic to around 600 Hz, indicating that the OF model could be used to establish an accurate virtual error sensor. Poor estimates at certain frequencies might be related to low coherence between the near-field microphone and the near-field electret. The virtual sensor was then used in conjunction with the ANC system and attenuated the SPLs of the range of shaft harmonics and BPFs between 4-14 dB, demonstrating that the observation filter might be used to attenuate the SPLs of a limited range of rotation rates.

# Chapter 8

# Conclusions

This work aimed to develop a virtual error sensor approach that can estimate the pressure response to a UAS rotor at a far-field location and subsequently eliminate the need to include a physical far-field microphone in an ANC system. The accuracy of the VES was first studied. A numerical model predicted the spatial extent of SPL attenuation using both a physical microphone and a virtual sensor to apply ANC to a far-field location. The VES was then used in conjunction with the ANC system to reduce the SPL at a designated virtual location. In addition to the virtual location, the response at the surrounding microphone locations were observed. ANC using a VES was applied when the airframe was in-line and perpendicular with the observer location. Finally, the observation filter was modeled using different FIR filters of different lengths to explore the filter length that would estimate an OF model that captured the magnitude and phase characteristics of surrounding rotation rates.

The system identification between the speaker and the far-field microphones and the speaker and the near-field electrets produced estimated plant models that correlate very well with the measured data. The system identification between the speaker and the far-field microphones was used to implement ANC using a far-field microphone as the physical error sensor, which reduces the SPLs

of the BPF and harmonics by about 30 dB, nearly background noise levels. The change in SPL at higher harmonics while using a physical microphone to apply ANC was large, which might be a result of recirculation effects, or be indiciatve of control spillover. ANC using the VES reduces the BPFs' SPLs between 6-13 dB, indicating that the reduction at observer locations is dependent on the quality of the observation filter. Using a VES, the change in SPLs of higher harmonics was small. Electret 2 was used to create the observation filter, as it identified an OF with significantly less error than those identified using electrets 1 and 3. However, the electrets each established virtual error sensors that attenuated the SPL at observer locations at similar levels.

After an OF was identified at a single rotation rate, 5250 RPM, ANC was applied to the virtual location, M3, while the rotor was operating at neighboring rotation rates. Results indicated that a single OF containing 1024 filter coefficients could be used in conjunction with an ANC system to reduce the SPL of the BPF at an observer location over a limited range of rotation rates. Using this OF to establish a virtual error sensor and apply ANC, the SPL of the frequency corresponding to the shaft rotation rate and BPF are reduced between 4 and 14 dB. The SPL fluctuations at higher harmonics are negligible. The OF was also identified using 256 and 512 coefficients, which do not accurately capture the magnitude and phase characteristics of the range of rotation rates, and the OFs were subsequently deemed insufficient to establish the VES.

The virtual error sensors that were established using the near-field electrets and far-field microphones successfully estimated the far-field SPL at the shaft rotation rate, the BPF and second harmonic. The far-field SPL at frequencies where the coherence between the reference tachometer and the estimated error signal was above 0.8 were accurately estimated. The far-field SPL at frequencies where coherence is low were not accurately estimated; subsequently, poor coherence might contribute to a poor error estimate. Frequencies where the far-field SPL are accurately estimated are successfully attenuated during ANC application. Additionally, a poor virtual sensor at certain frequencies might lead to amplification while applying ANC to the system.

In most cases, the ANC achieved at the far-field observer locations when the cone is positioned perpendicular relative to the microphone array is comparable to that achieved when the cone is in-line with the microphone array. However, the results differ when the OF is identified at one rotation rate and is used to apply ANC to an observer microphone at neighboring rotation rates. Each of the rotation rates is amplified at the third shaft harmonic, which might be attributed to poor coherence between the reference signal and the estimated error signal at that frequency. The SPLs of the surrounding microphones in both configurations are attenuated at the BPF, and the microphones closest to the observer location are also attenuated at the second harmonic, while the microphones furthest from the targeted microphone are amplified at the second harmonic, which can be attributed to the size of the zone of quiet, which changes with wavelength. This indicates that the VES that was established in this study can be used for practical ANC of rotor noise, and should be explored further.

The major findings in this work are:

- The VES is capable of estimating the far-field SPL when coherence between the estimated acoustic far-field response and the reference sensor is high.
- The ANC system using a VES is capable of attenuating the SPL of the rotor BPF between 6-13 dB.
- The SPLs of surrounding microphones closest to the targeted ANC location are reduced at the rotor BPF.
- Changes in SPL at higher harmonics are small when ANC using a VES is applied to the virtual location.
- An OF that is identified at a single rotation rate with 1024 filter coefficients is capable of capturing the magnitude and phase values of a small number of neighboring rotation rates.
- An OF that captures the magnitude and phase values at the shaft harmonics of neighboring rotation rates can be used to attenuate the SPL at the corresponding harmonics.

## 8.1 Future Work

In the future, a multiple-input control system should be studied to explore whether or not multiple near-field sensors produce an observation filter that captures more characteristics of the path from the near-field sensors to the virtual location. An array of virtual microphones could also be used to extend the control system to multiple-input-multiple-output (MIMO) or multiple-input-single-output (MISO) and explore the possibility of increasing the size of the zone of quiet so that locations immediately surrounding the designated observer location are not amplified at the BPF or the first two harmonics. Further, the observation filter should be studied further and interpolated from a wide range of measured rotation speeds. In order to increase practicality of implementing ANC on an in-flight UAS, the closed-loop ANC performance using the VES should be measured when the observation filter is identified at one rotation rate, and the rotation rate is changed during closed-loop data collection.

Additionally, it would be worthwhile to observe how the configuration of the cone relative to the rotor impacts the far-field responses with and without applying ANC. The cone should be positioned at different vertical clearances from the rotor to demonstrate how different UAS rotor-airframe configurations affect the estimate produced by virtual error sensor. Perhaps there is a clearance which allows the electrets to appropriately capture disturbance at the BPF and harmonics without simultaneously capturing downwash effects, leading to the estimation of a more accurate virtual error sensor. Flow recirculation effects on the results should also be investigated. The control system should be implemented on a very fast DSP, ADC/DAC to reduce latency and increase coherence. The sound field at different azimuthal angles should also be measured during ANC to understand how the ANC system affects the surrounding sound field. Finally, multiple rotors should be introduced to the test setup. Open-loop measurements should be collected, and the near-field changes should be observed.

# Bibliography


[1] Federal Aviation Administration. Community response to noise. https://www.faa.gov/regulations_policies/policy_guidance/noise/community/#annoyance, 2018. Accessed 2020.

[2] A. Christian and R. Cabell. Initial investigation into the psychoacoustic properties of small unmanned aerial system noise. In *AIAA/CEAS Aeroacoustics Conference*, 2017.

[3] N. S. Zawodny, D. D. Boyd Jr., and C. L. Burley. Acoustic characterization and prediction of representative, small-scale rotary-wing unmanned aircraft system components. *Proceedings of the AHS 72nd Annual Forum*, May 2016.

[4] N. S. Zawodny and D. D. Boyd Jr. Investigation of rotor-airframe interaction noise associated with small-scale rotary-wing unmanned aircraft systems. *Journal of the American Helicopter Society*, pages 1–17, January 2020.

[5] N. Intaratep, W. N. Alexander, W. J. Devenport, S. M. Grace, and A. Dropkin. Experimental study of quadcopter acoustics and performance at static thrust conditions. *Proceedings of the 22nd AIAA/CEAS Aeroacoustics Conference*, May 2016.

[6] J. Stephenson, D. Weitsman, and N. Zawodny. Effects of flow recirculation on unmanned aircraft system (uas) acoustic measurements in anechoic chambers. *The Journal of the Acoustical Society of America*, 145:11539, 2019.

[7] C. Hansen, S. Snyder, X. Qiu, L. Brooks, and D. Moreau. *Active Control of Noise and Vibration, Vol. 2*. CRC Press, 2012.

[8] G. Beckermann, I. Hosie, A. Clarke, M. Rowe, S. Rowe, S. Pentecost, and S. Edlin. Sound attenuating performance of nanofibre materials used in unmanned aerial vehicles. *TechConnect Briefs*, 1:212–215, 2018.

[9] N. Zawodny and N. Pettingill. Acoustic wind tunnel measurements of a quadcopter in hover and forward flight conditions. *Proceedings of InterNoise*, 2018.

[10] N.H. Schiller and N. S. Zawodny. Initial developments toward an active noise control system for small unmanned aerial systems. *Proceedings of InterNoise*, August 2018.

[11] S. Elliott and P. Nelson. *Active Control of Sound*. Academic Press, 1992.

[12] P. Lueg. Process of silencing sound oscillations, June 1936.

[13] P. A. Nelson, A. R. D. Curtis, S. J. Elliott, and A. J. Bullmore. The active minimization of harmonic enclosed sound fields, part i: Theory. *Journal of Sound and Vibration*, 117:1–13, 1987.

[14] A. R. D. Curtis A. J. Bullmore, P. A. Nelson and S. J. Elliott. The active minimization of harmonic enclosed sound fields, part ii: A computer simulation. *Journal of Sound and Vibration*, 117:15–33, 1987.

[15] S. J. Elliott, A. R. D. Curtis, A. J. Bullmore, and P. A. Nelson. The active minimization of harmonic enclosed sound fields, part iii: Experimental verification. *Journal of Sound and Vibration*, 117:35–38, 1987.

[16] S.J. Elliott, P. Joseph, A.J. Bullmore, and P.A. Nelson. Active cancellation at a point in a pure tone diffuse sound field. *Journal of Sound and Vibration*, 120:183–189, 1988.

[17] J. Garcia-Bonito, S. Elliott, and M. Bonilha. Active cancellation of pressure at a point in a pure tone diffracted diffuse sound field. *Journal of Sound and Vibration*, 201:43–65, 1997.

[18] R. Thomas, R. Burdisso, C. Fuller, and W. O'Brien. Active control of fan noise from a turbofan engine. *AIAA Journal*, pages 23–30, Jan 1994.

[19] R. H. Thomas, R. A. Burdisso, C. R. Fuller, and W. F. O'Brien. Preliminary experiment on active noise control of fan noise from a turbofan engine. *Journal of Sound and Vibration*, pages 532–537, March 1993.

[20] R. Burdisso and P. Smith. Active control of inlet noise from a turbofan engine using inlet wavenumber sensors. *AIAA Journal*, pages 99–1808, 1999.

[21] P. Smith, R. Burdisso, and C. Fuller. Experiments on active control of inlet noise from a turbofan engine using multiple circumferential control arrays. *2nd AIAA/CEAS-AeroacousticsConference*, pages 96–1792', 1996.

[22] R. A. Burdisso and C. R. Fuller. Active control of aircraft engine inlet noise using compact sound sources and distributed error sensors, May 1996.

[23] E. Envia. Fan noise reduction: an overview, February 2001.

[24] F. Pla, Z. Hu, and D. Sutliff. Active control of fan noise: Feasability study, September 1996.

[25] K. Gee and S. Sommerfeldt. A compact active control implementation for axial cooling fan noise. *Noise Control Engineering Journal*, 51:325–334, 2003.

[26] K. Gee and S. Sommerfeldt. Application of theoretical modeling to multichannel active control of cooling fan noise. *The Journal of the Acoustical Society of America*, 115:228–236, 2004.

[27] B. Shafer, K. Gee, and S. Sommerfeldt. Verification of a near-field error sensor placement method in active control of compact noise sources. *The Journal of the Acoustical Society of America*, 127:EL66, 2010.

[28] K. Homma, A. Charpentier, , and C. R. Fuller. Active-passive control of noise radiated from personal computers. *Inter-Noise 2002*, 08 2002.

[29] D. Moreau, B. Cazzolato, A. Zander, and C. Peterson. A review of virtual sensing algorithms for active noise control. *Algorithms*, 1:66–99, 2008.

[30] C. Petersena, R. Fraanjeb, B. Cazzolatoa, A. Zandera, and C. Hansen. A kalman filter approach to virtual sensing for active noise control. *Mechanical Systems and Signal Processing*, 22:490–508, 2008.

[31] J. Munn, B. Cazzolato, C. Kestell, and C. Hansen. Virtual error sensing for active noise control in a one-dimensional waveguide: Performance prediction versus measurement. *The Journal of the Acoustical Society of America*, 113:35, 2003.

[32] J. Garcia-Bonito, S. J. Elliott, and C. Boucher. Generation of zones of quiet using a virtual microphone arrangement. *The Journal of the Acoustical Society of America*, 101:3498, 1997.

[33] J. Bean, C. Fuller, and N. Schiller. Hybrid feedforward-feedback noise control using virtual sensors. *Noise-Con 2016*, 06 2016.

[34] J. Bean. Design and analysis of an active noise canceling headrest, March 2018.

[35] A. Roure and A. Albarrazin. The remote microphone technique for active noise control. In *Internoise and Noise-Con Congress and Conference Proceeding*, pages 1233–1244, 1999.

[36] C. Fuller, C. Papenfuss, and T. Saux. Active-passive control of portable generator set radiated noise. In *Proceedings of Acoustics 2012*, Freemantle, Australia, 2012.

[37] D. Moreau, J. Ghan, B. Cazzolato, and A. Zander. Active noise control in a pure tone diffuse sound field using virtual sensing. *The Journal of the Acoustical Society of America*, 125:3742–55, 07 2009.

[38] C. Kestell, B. Cazzolato, and C. Hansen. Active noise control in a free field with virtual sensors. *The Journal of the Acoustical Society of America*, 109:232, 2001.

[39] S. Elliott and A. David. A virtual microphone arrangement for local active sound control. In *Proceedings of the 1st International Conference on Motion and Vibration Control*, pages 1027–1031, Yokohama, Japan, 1992.

[40] S. Kuo and D. Morgan. *Active Noise Control Systems: Algorithms and DSP Implementations*. John Wiley & Sons, Inc., 1996.

[41] S. Elliott. *Signal Processing for Active Control*. Academic Press, 2001.

[42] H. Olson and E. May. Electronic sound absorber. *The Journal of the Acoustical Society of America*, 25:1130, 1953.

[43] C. Fuller, S. Elliott, and P. Nelson. *Active Control of Vibration*. Elsevier Science & Technology, 1996.

[44] J. Cheer and S. Daley. Active strcutural acoustic control using the remote sensor method. *Journal of Physics: Conference Series*, 744:012184, 2016.

[45] C. Radcliffe and S. Gogate. Model based feedforward noise control algorithm for vehicle interiors. 1993.

[46] J. Cheer, S. Elliott, O. Eunmi, and J. Jeong. Application of the remote microphone technique method to active noise control in a cell phone. *The Journal of the Acoustical Society of America*, 143:2412, 2018.

[47] W. Jung, S. Elliott, and J. Cheer. The effect of remote microphone technique and head-tracking on local active sound control. *23rd International Congress on Sound and Vibration*, 07 2016.

[48] COMSOL. Introduction to acoustics module. `https://doc.comsol.com/5.4/doc/com.comsol.help.aco/IntroductionToAcousticsModule.pdf.`, 1998-2018. Accessed 2020.

[49] C. J. Chapman. The structure of rotating sound fields. *Proceedings of the Royal Society of London, Series A: Mathematical and Physical Sciences*, 440, 1993.

[50] P.R. Prentice. The acoustic ring source and its application to propeller acoustics. *Proceedings of the Royal Society of London, Series A: Mathematical and Physical Sciences*, 437, 1992.

[51] S. Elliott and J. Cheer. Modeling local active sound control with remote sensors in spatially random pressure fields. *The Journal of the Acoustical Society of America*, 137:1936, 2015.

[52] P.D. Welch. The use of fast fourier transforms for the estimation of power spectra: A method based on time averaging over short modified periodograms. *IEEE Transactions on Audio and Electroacoustics*, 15:70–73, 1967.

[53] R. H. Cabell and C. R. Fuller. A principal component algorithm for feedforward active noise and vibration control. *Journal of Sound and Vibration*, pages 159–181, 1999.

# Appendix A

# ANC using a VES established at supplementary microphone locations

## A.1 ANC using a VES at far-field locations.

This section presents ANC results using a VES at designated far-field observer locations while the rotor is operating at 5250 RPM and 6000 RPM. For comparison, ANC using a physical sensor is also shown. Figure A.1 shows the SPL attenuation at M1 using a virtual sensor when the rotor is operating at 5250 RPM and 6000 RPM. Figure A.1a shows the SPL attenuation achieved using a VES to apply ANC at M1. The SPLs of the shaft harmonic (87.5 Hz) and BPF (175 Hz) are reduced nearly 13 dB and 9 dB, respectively. Additionally, the SPL of the fourth shaft harmonic (350 Hz) is reduced 7 dB. Figure A.1b show the SPL attenuation achieved using a VES while the rotor is operating at 6000 RPM. The SPL of the shaft harmonic (100 Hz) is attenuated by about 4 dB. The SPLs of the BPF (200 Hz) and fourth shaft harmonic (400 Hz) are reduced by 7 dB and 4 dB. Similar results are also achieved at M5, shown in Figure A.2. Both Figures show that the SPLs of the higher harmonics are not amplified.

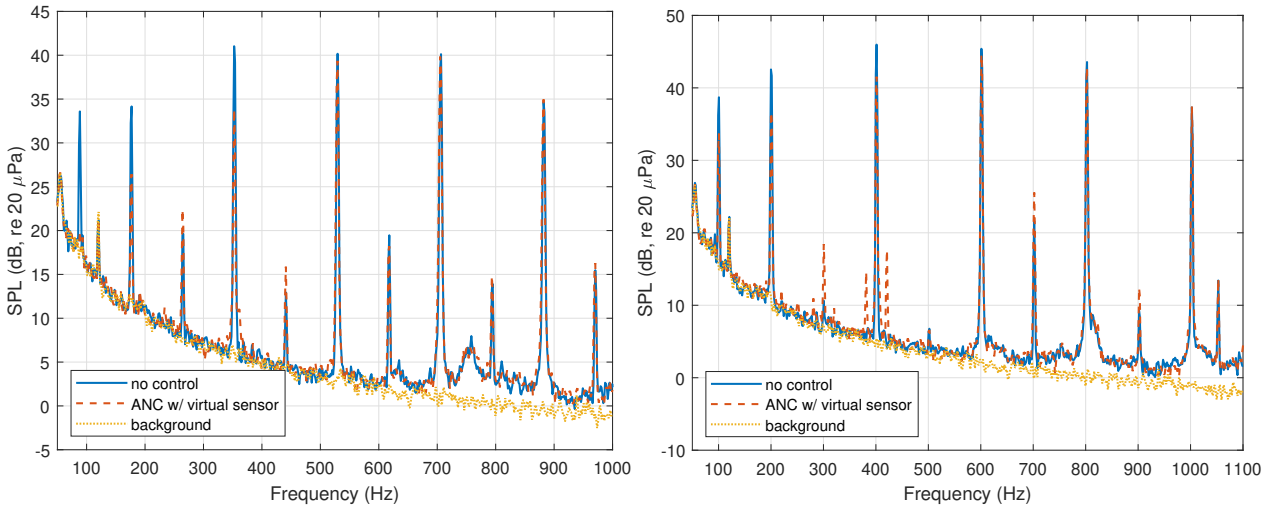


(a) (b)

Figure A.1: Comparison of ANC at M1 using a VES developed through Electret 2 while the rotor is operating at (a) 5250 RPM and (b) 6000 RPM.

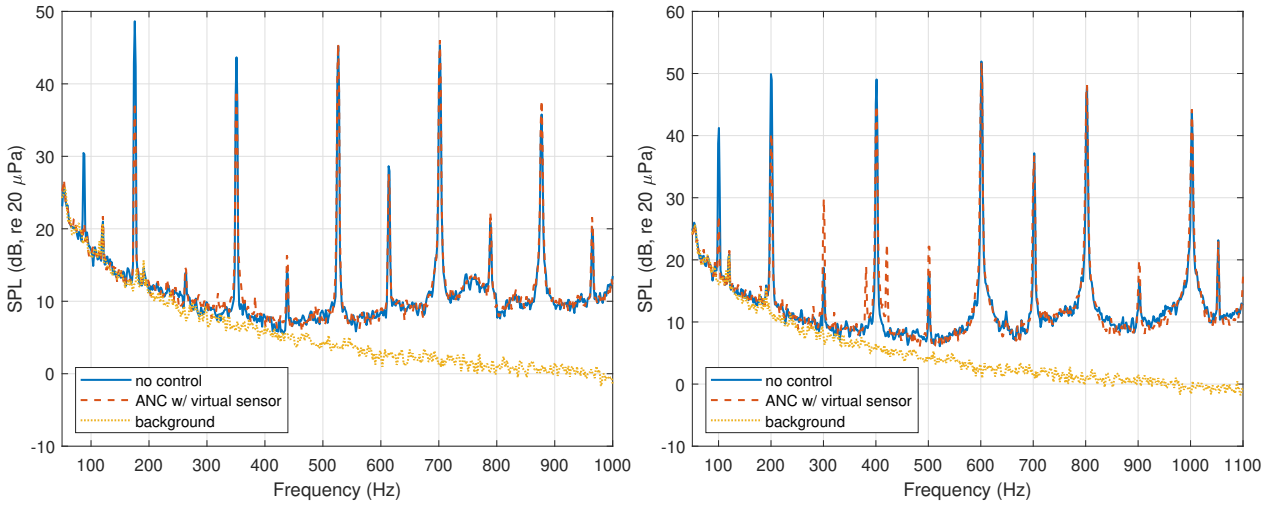


(a) (b)

Figure A.2: Comparison of ANC at M5 using a VES developed through Electret 2 while the rotor is operating at (a) 5250 RPM and (b) 6000 RPM.

## A.2 Change in SPL at surrounding microphone locations.

This section presents results showing the SPL reduction achieved at a designated virtual microphone location and surrounding microphone locations. Figure A.3a shows the SPL attenuation

achieved while the rotor is operating at 5250 RPM, and the designated virtual location is M1. The SPL of each microphone is attenuated at the shaft harmonic (87.5 Hz) and rotor BPF (175 Hz). The SPLs of closest to M1 are attenuated most, while the SPLs of microphones M4 and M5 are attenuated least. At the third shaft harmonic (262.5 Hz), the SPLs of microphones M1-M3 are amplified, which could indicate an inaccurate OF at this frequency. Figure A.3b shows the SPL attenuation achieved at the far-field microphones while the rotor is operating at 6000 RPM, and the virtual location is M1. Figure A.4 shows the ANC results at M5 while the rotor is operating at 5250 RPM and 6000 RPM.

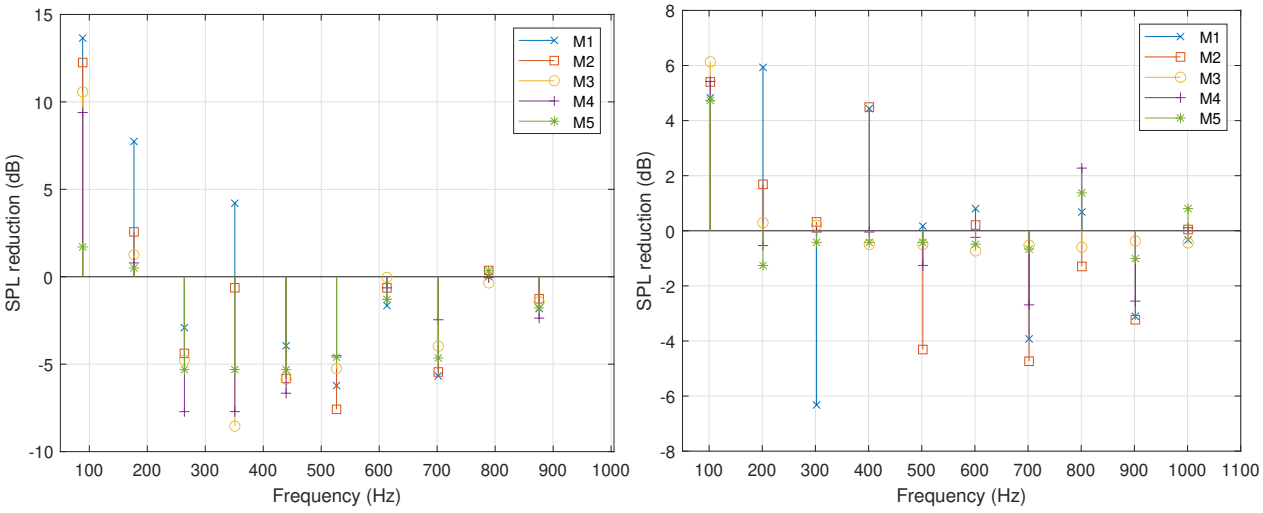


Figure A.3: Far-field microphone ANC response using the VES developed with Electret 2 when the rotor is operating at (a) 5250 RPM and (b) 6000 RPM.

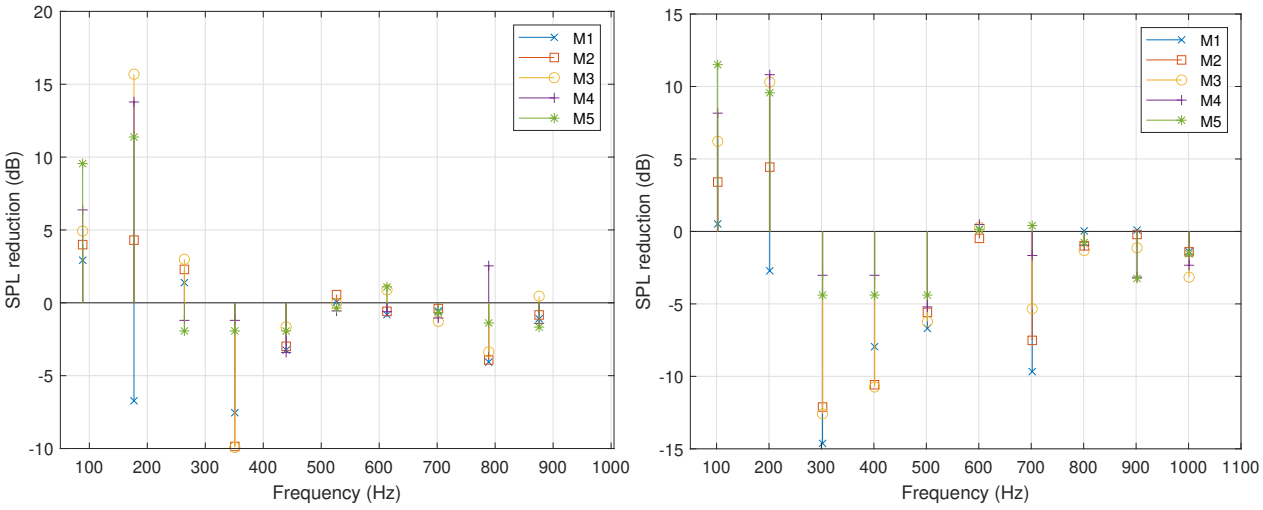


(a) (b)

Figure A.4: Far-field microphone ANC response using the VES developed with Electret 2 when the rotor is operating at (a) 5250 RPM and (b) 6000 RPM.

## A.3 ANC using a VES when the cone is perpendicular to the microphone array

This section presents ANC results using a VES at designated far-field observer locations while the rotor is operating at 5250 RPM and 6000 RPM. For comparison, ANC using a physical sensor is also shown. Figure A.5 shows the SPL attenuation at M1 using a physical sensor and a virtual sensor when the cone is perpendicular to the microphone array and the rotor is operating at 5250 RPM. ANC using a physical sensor is shown in Figure A.5a. The SPLs of the shaft harmonic (87.5 Hz) and the BPF (175 Hz) are attenuated nearly 40 dB. Additionally, the SPL of the second harmonic (350 Hz) is attenuated nearly 30 dB. Figure A.5b shows the SPL attenuation achieved using a VES to apply ANC at M1. The SPLs of the shaft harmonic and BPF are both reduced nearly 8 dB. Additionally, the SPL of the fourth shaft harmonic is reduced 6 dB. Similar results are also achieved at M5 while the rotor is operating at 5250 RPM, however Figure A.8b shows that the measured SPL at M5 during ANC using a virtual error sensor indicates that the speaker becomes saturated, most likely due to an issue with the controller. It is possible that this is the result of an inaccurate system ientification.

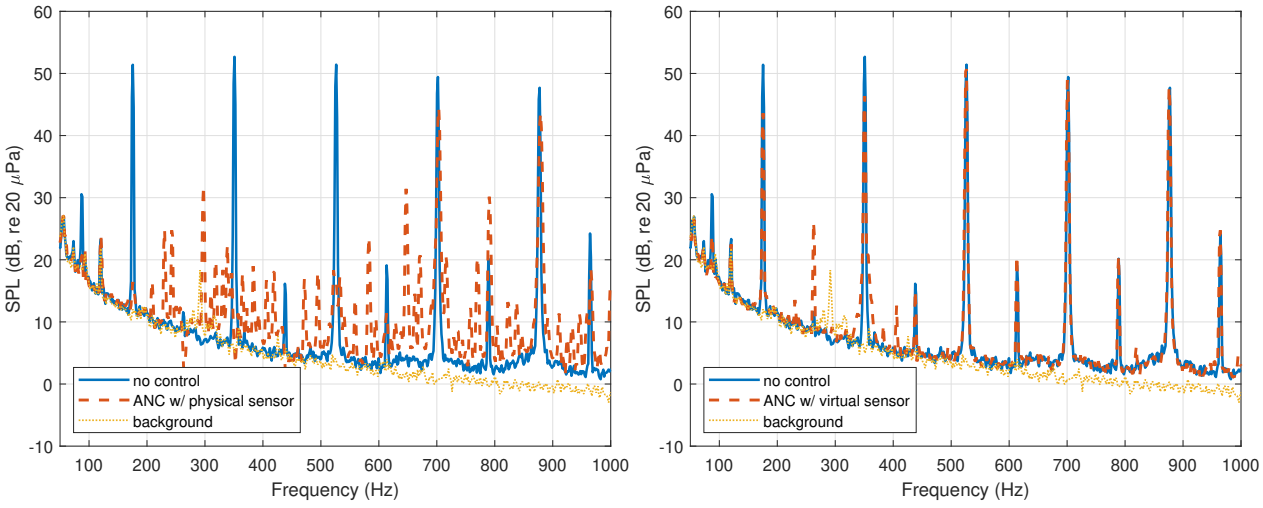


(a) (b)

Figure A.5: Comparison of ANC at M1 using a (a) physical sensor and (b) a virtual error sensor developed through Electret 2 (RPM = 5250).

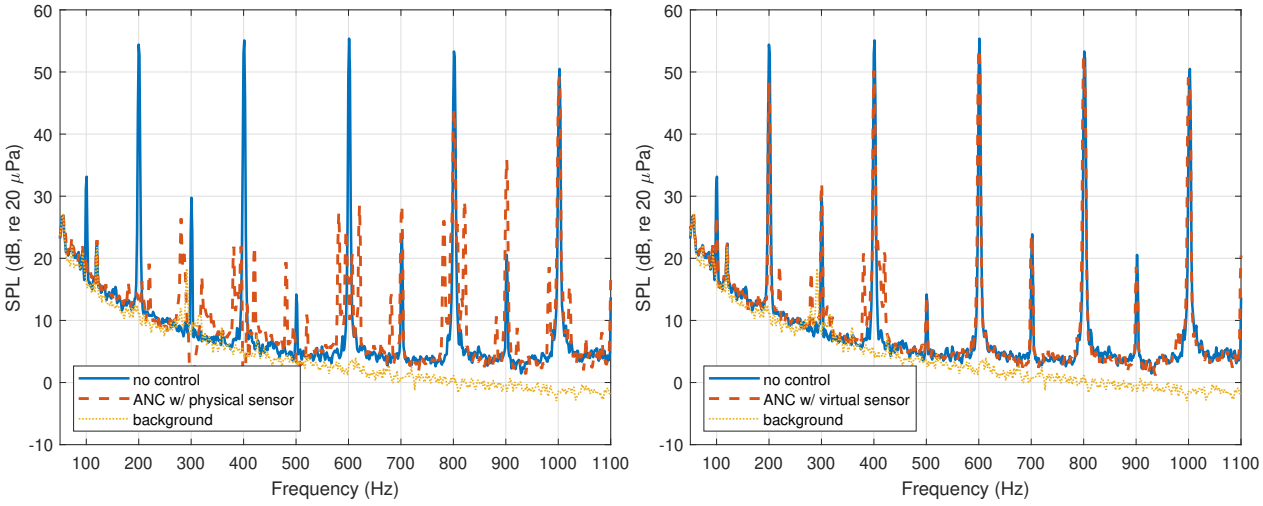


(a) (b)

Figure A.6: Comparison of ANC at M1 using a (a) physical sensor and (b) a virtual error sensor developed through Electret 2 (RPM = 6000).

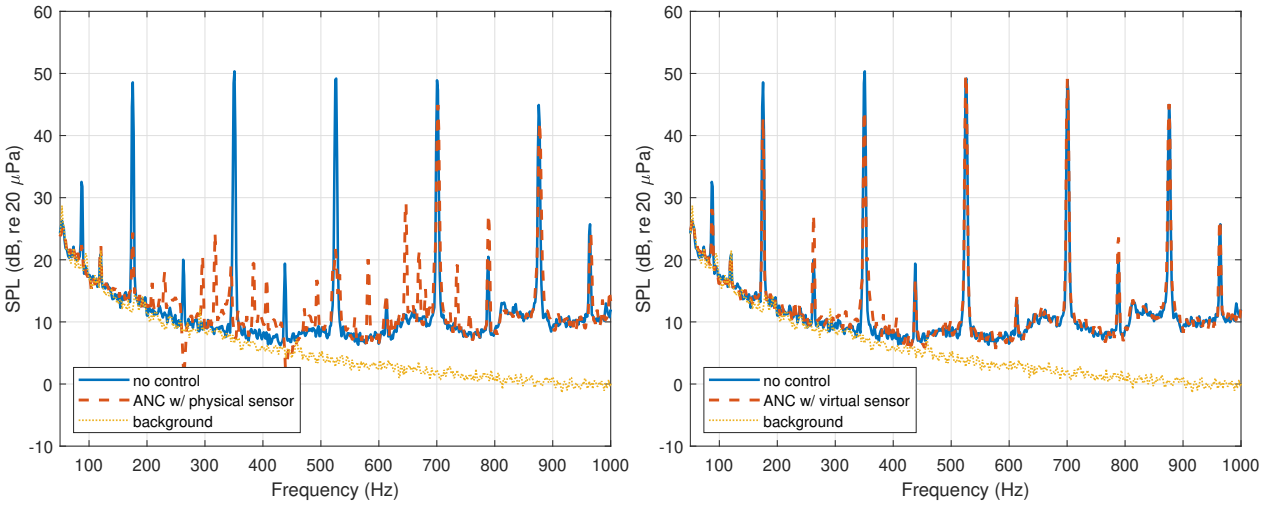


(a) (b)

Figure A.7: Comparison of ANC at M5 using a (a) physical sensor and (b) a virtual error sensor developed through Electret 2 (RPM = 5250).

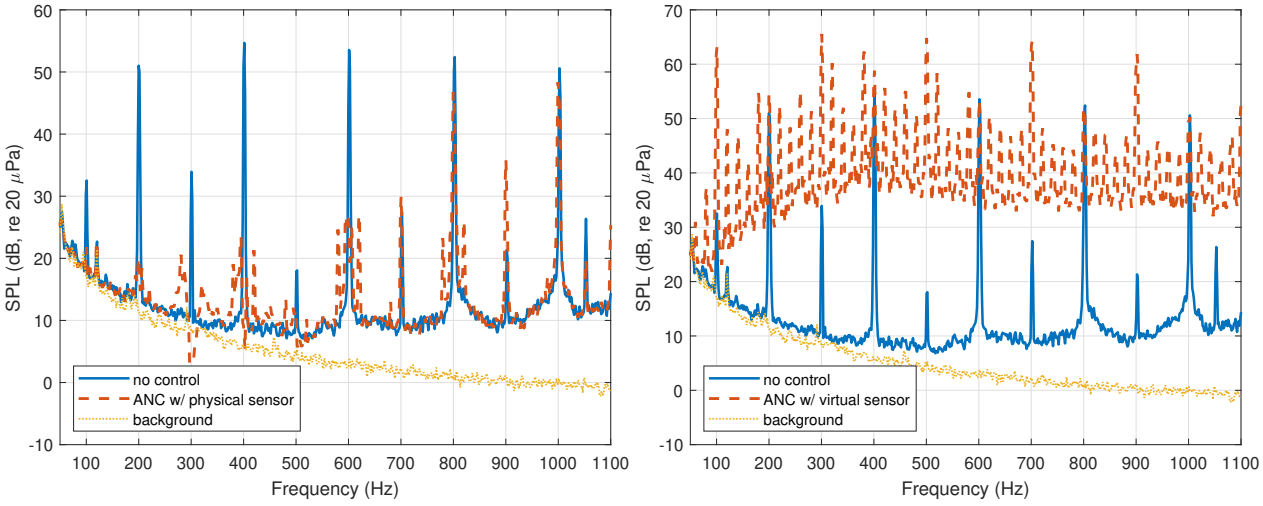


(a) (b)

Figure A.8: Comparison of ANC at M5 using a (a) physical sensor and (b) a virtual error sensor developed through Electret 2 (RPM = 6000).

## A.4 Change in SPL at surrounding microphone locations when the cone is perpendicular to the microphone array.

This section presents results showing the SPL reduction achieved at a designated virtual microphone location and surrounding microphone locations. Figure A.9a shows the SPL attenuation achieved while the rotor is operating at 5250 RPM, and the designated virtual location is M1. The SPL of each microphone is attenuated at the shaft harmonic (87.5 Hz) and rotor BPF (175 Hz). The SPLs of closest to M1 are attenuated most, while the SPLs of microphones M4 and M5 are attenuated least. At the third shaft harmonic (262.5 Hz), the SPLs of microphones M1-M3 are amplified, which could indicate an inaccurate OF at this frequency. Figure A.9b shows the SPL attenuation achieved at the far-field microphones while the rotor is operating at 6000 RPM, and the virtual location is M1. Figure A.10 shows the ANC results at M5 while the rotor is operating at 5250 RPM and 6000 RPM.

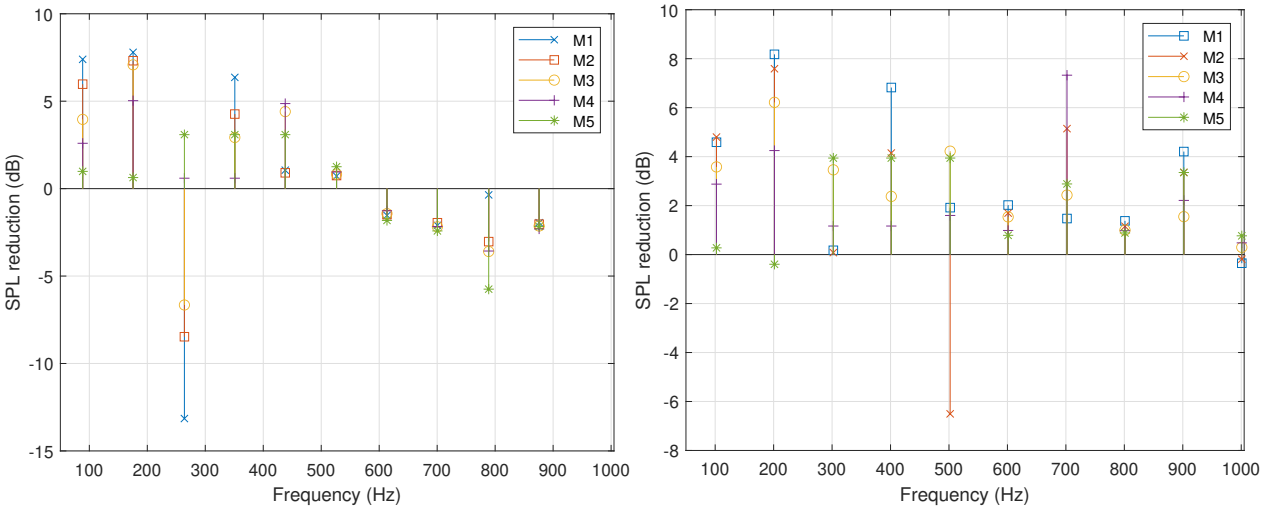


(a) (b)

Figure A.9: ANC response at M1 using the VES developed with Electret 2 when the rotor is operating at (a) 5250 RPM and (b) 6000 RPM.

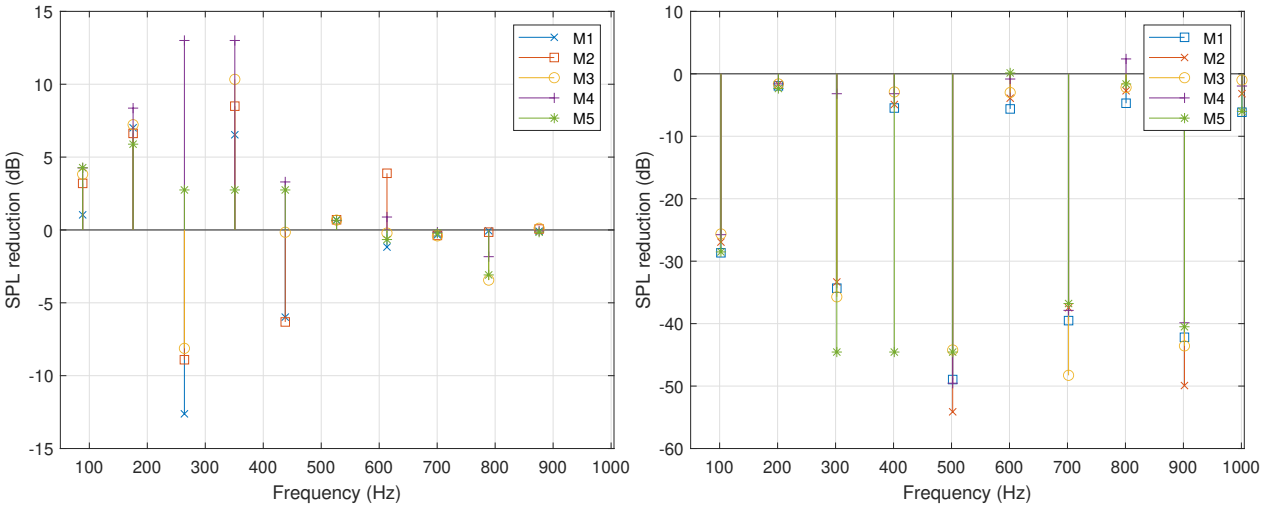


(a) (b)

Figure A.10: ANC response at M5 using the VES developed with Electret 2 when the rotor is operating at (a) 5250 RPM and (b) 6000 RPM.